Doctoral Dissertation (Censored)
博士論文 (要約)

Frequency-Dependent Squeezed Vacuum Source with Filter Cavity Control using Coherent Control Sidebands for Gravitational-Wave Detectors

(重力波望遠鏡のためのコヒーレントコントロール光によるフィルター共振器制御を用いた周波数依存スクイーズド真空場)

A Dissertation Submitted for the Degree of Doctor of Philosophy

December 2020
令和２年１２月博士 (理学) 申請

Department of Physics, Graduate School of Science,
The University of Tokyo
東京大学大学院理学系研究科物理学専攻

Naoki Aritomi
有冨尚紀

Abstract

The sensitivity of gravitational-wave (GW) detectors is designed to be limited by quantum noise. The quantum noise originates from the quantum vacuum field entering from an output port of the interferometer. The quantum noise is composed of shot noise and radiation pressure noise. The shot noise originates from the phase fluctuation of the vacuum field and dominates at high frequencies of the detector sensitivity, while the radiation pressure noise originates from the amplitude fluctuation of the vacuum field and dominates at low frequencies. The sensitivity of current GW detectors is dominated by shot noise at high frequencies. To reduce the shot noise, the frequency-independent squeezing, whose phase quadrature is squeezed, has been injected into the interferometer and the shot noise reduction by $\sim$3 dB has been achieved in Advanced LIGO and Advanced Virgo. However, the increase of the radiation pressure noise due to the frequency-independent squeezing has been observed in Advanced LIGO and Advanced Virgo.

To reduce the shot noise and radiation pressure noise simultaneously, the frequency-dependent squeezing, which is phase squeezed at high frequencies and amplitude squeezed at low frequencies, is required. The most promising way to realize the frequency-dependent squeezing is reflecting a frequency-independent squeezed vacuum field off an optical cavity called filter cavity. In the past, the squeezing angle rotation using rigid, meter-scale filter cavities has been realized in the MHz and kHz regions. However, frequency-dependent squeezing with a rotation frequency below 100 Hz, which is required in GW detectors, has not been demonstrated.

In this thesis, we developed the first frequency-dependent squeezed vacuum source with a rotation frequency below 100 Hz by using a 300 m filter cavity which can fit for Advanced LIGO and Advanced Virgo. It is shown that our frequency-dependent squeezed vacuum source can realize the broadband quantum noise reduction in GW detectors. However, in this measurement, the filter cavity length noise and the mode mismatch between the squeezer and the filter cavity were not satisfying the target value, and the detuning fluctuation of $\sim$30 Hz was observed. For further quantum noise reduction, it is necessary to stabilize the filter cavity length fluctuation, the alignment fluctuation, and the detuning fluctuation. In this measurement, the filter cavity was controlled with the auxiliary green field whose frequency is as twice as the squeezing frequency. As the optical path and the frequency of the green field and the squeezed field are different, the filter cavity control with the auxiliary green field does not ensure the filter cavity length and alignment for the squeezed field.

To solve this problem, I suggested a new control scheme of the filter cavity using coherent control sidebands, which are already used to control the squeezing angle. As the coherent control sidebands have the same optical path and almost the same frequency as the squeezed field, the control of the filter cavity with the coherent control sidebands ensures the filter cavity length and alignment for the squeezed field. I succeeded in controlling the length of the 300 m filter cavity with the new control scheme and demonstrated that the new control scheme reduced the filter cavity length fluctuation from 3.4 pm to 0.75 pm, which satisfies the target value of 1 pm. Using this new control scheme, the frequency-dependent squeezing with a rotation frequency approximately 100 Hz also has been realized.

The results presented in this thesis are significant for improving the sensitivity of the current GW detectors such as Advanced LIGO, Advanced Virgo, and KAGRA as well as the future third-generation GW detectors such as the Einstein Telescope and Cosmic Explorer, which require even longer filter cavities.

Thesis supervisor: Masaki Ando (Associate Professor)
Thesis title: Frequency-Dedenpent Squeezed Vacuum Source with Filter Cavity Control using Coherent Control Sidebands for Gravitational-Wave Detectors

Contents

Glossary

AMC	Alignment Mode Cleaner
AOM	Acousto-Optic Modulator
AR	Anti-Reflection
AS	Anti-Symmetric
BBH	Binary Black Hole
BNS	Binary Neutron Star
BS	Beam Splitter
CBC	Compact Binary Coalescence
CC	Coherent Control
CCSB	Coherent Control SideBands
DDS	Direct Digital Synthesizer
DECIGO	DECi-hertz Interferometer Gravitational-wave Observatory
DRFPMI	Dual Recycled Fabry-Perot Michelson Interferometer
EOM	Electro-Optic Modulator
ETM	End Test Mass
FC	Filter Cavity
FDS	Frequency-Dependent Squeezing
FIS	Frequency-Independent Squeezing
FSR	Free Spectral Range
FP	Fabry-Perot
GRMC	GReen Mode Cleaner
GW	Gravitational Wave
HR	High Reflection
IR	InfraRed
IRMC	InfraRed Mode Cleaner
ITM	Input Test Mass
LIGO	Laser Interferometer Gravitational-wave Observatory
LO	Local Oscillator
MI	Michelson Interferometer
MZ	Mach-Zehnder interferometer
NSBH	Neutron Star Black Hole
OPO	Optical Parametric Oscillator
PBS	Polarizing Beam Splitter
PD	Photo Detector
PDH	Pound-Drever-Hall
PLL	Phase-Locked Loop
PPKTP	Periodically Poled Potassium Titanyl Phosphate
PRM	Power Recycling Mirror

RSE	Resonant Sideband Extraction
SHG	Second Harmonic Generation
SQL	Standard Quantum Limit
SRM	Signal Recycling Mirror

Chapter 1

Introduction

In 2015, gravitational waves (GWs) from a binary black hole merger were observed by Advanced LIGO for the first time [1]. Thereafter, GW astronomy rapidly became a mature research field. After the observation of GWs from a binary neutron star merger [2] and the publication of the first GW sources catalog [3], the network of the GW detectors (composed of the two Advanced LIGO [4] and Advanced Virgo [5]) performed a third observing run (O3) and detected several candidates per month. The second GW sources catalog, which contains detections during the first half of O3, was recently published [6]. The Japanese detector KAGRA [7] is expected to join the network from the next observing run (O4) and a fifth detector, LIGO India, is expected to join in 2025 [8]. However, the sensitivity of the current GW detectors is not enough to determine the characteristics of the compact objects such as black holes and neutron stars, and to reveal the formation scenario of the compact binary systems, and to test the general relativity in the stronger gravity field. For the further GW detections and the precise measurement of the GW waveforms, it is necessary to improve the sensitivity of the current GW detectors.

The principle of the current GW detectors is a Michelson interferometer. As the motion of the test mass mirrors induced by GWs can be measured by the laser light in the interferometer, the fundamental sensitivity of the interferometric GW detectors is limited by the quantum fluctuation of the laser light in the classical picture. Therefore, it is important to reduce the quantum noise to improve the fundamental sensitivity of GW detectors. In the current GW detectors, the quantum noise limits the sensitivity at high frequencies, while other classical noises limit the sensitivity at low frequencies. In the future, the other classical noises are expected to be reduced and the quantum noise will limit the sensitivity at all frequencies.

The quantum noise originates from the quantum fluctuation of light and it is composed of quantum shot noise and radiation pressure noise. The shot noise dominates at high frequencies of the detector sensitivity, while the radiation pressure noise dominates at low frequencies. In 1981, Caves reported that quantum noise originates from quantum vacuum fluctuations entering from an output port of the interferometer [9]. He also suggested that quantum noise can be reduced by replacing the ordinary vacuum states with so-called squeezed vacuum states, whose fluctuations are reduced in one quadrature, while they

are increased in the orthogonal quadrature, following Heisenberg's uncertainty principle. When the noise reduced quadrature of the squeezed vacuum states is aligned with the GW signal, the signal to noise ratio of the GW signal is increased and therefore the sensitivity of GW detectors is improved.

In order to enhance the sensitivity of the current GW detectors at high frequencies where the shot noise mainly dominates, so-called frequency-independent squeezed vacuum sources have been implemented into the GW detectors such as Advanced LIGO and Advanced Virgo. The squeezed vacuum states of these frequency-independent squeezed vacuum sources are squeezed in the phase quadrature. Consequently, both Advanced LIGO and Advanced Virgo successfully reduced the shot noise and their detection rates were increased by ∼50 % in O3 [10, 11]. However, the frequency-independent squeezed vacuum currently used in GW detectors cannot reduce the shot noise and radiation pressure noise simultaneously. The reason is the optomechanical coupling between the laser light and the suspended test masses, which induces a rotation of the squeezing ellipse as a function of frequency. Therefore, the quadrature whose noise is reduced cannot be aligned with the GW signal at all frequencies. In fact, the increase in radiation pressure noise due to the frequency-independent squeezing has recently been observed in both Advanced LIGO and Advanced Virgo [12, 13]. This is one of the biggest obstacles for advanced GW detectors to reach their design sensitivity and go beyond.

One of the solutions to reduce the quantum noise at all frequencies is the injection of so-called frequency-dependent squeezed vacuum, whose squeezing angle rotates by 90° as a function of frequency, to counteract the squeezing angle rotation induced by the interferometer. Such a quantum noise reduction is optimal if the rotation occurs at the crossover frequency between the shot noise and the radiation pressure noise, which is approximately 70 Hz for advanced GW detectors. To realize the frequency-dependent squeezing, it was suggested to reflect a frequency-independent squeezed vacuum off an optical Fabry-Perot cavity called a filter cavity [14]. Previously, squeezing angle rotation using rigid, meter-scale filter cavities has been realized in the MHz [15] and kHz [16] regions.

In this thesis, we developed the first frequency-dependent squeezed vacuum source with the rotation frequency below 100 Hz by using a 300 m filter cavity which can fit for Advanced LIGO and Advanced Virgo [17]. It is shown that our frequency-dependent squeezed vacuum source can realize the broadband quantum noise reduction in GW detectors. However, in this measurement, the filter cavity length noise and the mode mismatch between the squeezer and the filter cavity were not satisfying the target value, and the detuning fluctuation of ∼30 Hz was observed. For further quantum noise reduction, it is necessary to stabilize the filter cavity length fluctuation, the alignment fluctuation, and the detuning fluctuation. In this measurement, the filter cavity was controlled with the auxiliary green field whose frequency is as twice as the squeezing frequency. As the optical path and the frequency of the green field and the squeezed field are different, the filter cavity control with the auxiliary green field does not ensure the filter cavity length and alignment for the squeezed field.

To solve this problem, I suggested a new control scheme of the filter cavity using coherent control sidebands which are already used to control the squeezing angle [18]. As the coherent control sidebands have the same optical path and almost the same frequency as the squeezed field, the control of the filter cavity with the coherent control sidebands ensures the filter cavity length and alignment for the squeezed field. I succeeded in controlling the length of the 300 m filter cavity with the new control scheme and demonstrated that the new control scheme reduced the filter cavity length fluctuation from 3.4 pm to 0.75 pm which satisfies the target value of 1 pm. Using this new control scheme, the frequency-dependent squeezing with the rotation frequency around 100 Hz also has been realized.

This thesis is organized as follows: in Chapter 2, the theory of gravitational waves and gravitational-wave observations are explained. In Chapter 3, the principle of gravitational-wave detectors is explained. In Chapter 4, the theory of the quantum states of light including squeezed states is described. In Chapter 5, the quantum noise in GW detectors and how to reduce it are presented. In Chapter 6, the experiment on frequency-independent squeezing is described. In Chapter 7, the experimental characterization of the 300 m filter cavity and the experiment on frequency-dependent squeezing are presented. In Chapter 8, the theoretical suggestion and experimental demonstration of a new control scheme of the filter cavity are presented. In Chapter 9, the conclusion is described.

Chapter 2

Gravitational Wave

Gravitational waves (GWs) are ripples of spacetime derived from general relativity. As GWs almost do not interfere with matters, GWs from astrophysical sources can reach Earth without losing their information. In this chapter, the theory of GWs and recent GW detections are presented.

2.1 Derivation of gravitational waves

2.1.1 Linearization of Einstein equation

Einstein equation derived from general relativity can be written as follows:

$$R_{\mu\nu} - \frac{1}{2} g_{\mu\nu} R = \frac{8\pi G}{c^4} T_{\mu\nu}, \tag{2.1}$$

where $R_{\mu\nu}$ is the Ricci tensor, $g_{\mu\nu}$ is the metric tensor, R is the scalar curvature or Ricci scalar, $T_{\mu\nu}$ is the energy momentum tensor, G is the gravitational constant, and c is the speed of light. The greek indices range from 0 to 3. $R_{\mu\nu}$ and R can be written as

$$R_{\mu\nu} = R^{\alpha}{}_{\mu\alpha\nu}, \tag{2.2}$$

$$R = g^{\mu\nu} R_{\mu\nu}, \tag{2.3}$$

where $R^{\mu}{}_{\nu\rho\sigma}$ is the Riemann curvature tensor:

$$R^{\mu}{}_{\nu\rho\sigma} = \frac{\partial \Gamma^{\mu}_{\nu\sigma}}{\partial x^{\rho}} - \frac{\partial \Gamma^{\mu}_{\nu\rho}}{\partial x^{\sigma}} + \Gamma^{\mu}_{\alpha\rho}\Gamma^{\alpha}_{\nu\sigma} - \Gamma^{\mu}_{\alpha\sigma}\Gamma^{\alpha}_{\nu\rho}, \tag{2.4}$$

and

$$\Gamma^{\rho}_{\mu\nu} = \frac{1}{2} g^{\rho\sigma} \left(\frac{\partial g_{\sigma\nu}}{\partial x^{\mu}} + \frac{\partial g_{\sigma\mu}}{\partial x^{\nu}} - \frac{\partial g_{\mu\nu}}{\partial x^{\sigma}} \right) \tag{2.5}$$

is the Christoffel symbol.

Considering the small perturbation of the metric as follows:

$$g_{\mu\nu} = \eta_{\mu\nu} + h_{\mu\nu}, \tag{2.6}$$

where $\eta_{\mu\nu} = \mathrm{diag}(-1, 1, 1, 1)$ is the metric in Minkowski spacetime (flat spacetime) and $h_{\mu\nu}$ is the small perturbation of the metric. Substituting this into the Einstein equation and considering the first order of $h_{\mu\nu}$, the Einstein equation results in the following wave equation:

$$\Box \overline{h}_{\mu\nu} = -\frac{16\pi G}{c^4} T_{\mu\nu}, \tag{2.7}$$

where $\overline{h}_{\mu\nu} \equiv h_{\mu\nu} - \frac{1}{2}\eta_{\mu\nu}\eta^{\alpha\beta}h_{\alpha\beta}$ and the Lorentz gauge

$$\frac{\partial \overline{h}^{\mu\nu}}{\partial x^{\mu}} = 0 \tag{2.8}$$

is assumed. This wave equation indicates that the small metric variation propagates the spacetime as waves and these are gravitational waves.

2.1.2 Plane wave solution of gravitational waves

Gravitational waves propagating in the vacuum ($T_{\mu\nu} = 0$) can be written as

$$\Box \overline{h}_{\mu\nu} = 0. \tag{2.9}$$

As a solution of this wave equation, $\overline{h}_{\mu\nu} = a_{\mu\nu}e^{ik_\alpha x^\alpha}$ is considered. Based on the symmetry of $\overline{h}_{\mu\nu}$, the Lorentz gauge, and wave equation,

$$a_{\mu\nu} = a_{\nu\mu}, \tag{2.10}$$
$$a_{\mu\alpha}k^{\alpha} = 0, \tag{2.11}$$
$$k_{\alpha}k^{\alpha} = 0. \tag{2.12}$$

Equation (2.11) indicates that the gravitational waves are transverse waves and Equation (2.12) shows that the gravitational waves propagate at the speed of light.

To remove the remaining degrees of freedom for coordinate transformation, Transverse Traceless gauge (TT gauge) is assumed as follows:

$$h_{\mu 0} = 0, \tag{2.13}$$
$$h_{ij}{}^{,j} = 0, \tag{2.14}$$
$$h^{j}{}_{j} = 0. \tag{2.15}$$

Here, the Latin indices range from 1 to 3. Under this gauge, the amplitude of the gravitational wave $a_{\mu\nu}$ is written as follows:

$$a_{\mu\nu} = \begin{pmatrix} 0 & 0 & 0 & 0 \\ 0 & h_+ & h_\times & 0 \\ 0 & h_\times & -h_+ & 0 \\ 0 & 0 & 0 & 0 \end{pmatrix}. \tag{2.16}$$

The gravitational waves have two degrees of freedom, which are h_+ and $h_\times$.

When the plane wave with frequency ω propagates toward the z-axis direction,

$$h_{\mu\nu}^{\mathrm{TT}} = a_{\mu\nu} \exp\left[-i\omega(t - z/c)\right]. \tag{2.17}$$

The space line element of the Minkowski spacetime is

$$\begin{aligned} dl^2 &= (\delta_{ij} + h_{ij}^{\mathrm{TT}}) dx^i dx^j \\ &= \{1 + h_+ \cos\left[\omega(t - z/c)\right]\} dx^2 + \{1 - h_+ \cos\left[\omega(t - z/c)\right]\} dy^2 + dz^2 \\ &\quad + 2h_\times \cos\left[\omega(t - z/c)\right] dx dy, \end{aligned} \tag{2.18}$$

where the real part of h_{ij} is considered.

When the amplitude of the gravitational waves is significantly small and the metric is the Minkowski spacetime, Equation (2.18) indicates that the distance between two points changes as follows:

$$dl^2 = \delta_{ij} dx'^i dx'^j, \tag{2.19}$$

$$dx' = \left(1 + \frac{h_+ \cos\left[\omega(t - z/c)\right]}{2}\right) dx + \frac{h_\times \cos\left[\omega(t - z/c)\right]}{2} dy, \tag{2.20}$$

$$dy' = \left(1 - \frac{h_+ \cos\left[\omega(t - z/c)\right]}{2}\right) dy + \frac{h_\times \cos\left[\omega(t - z/c)\right]}{2} dx. \tag{2.21}$$

This change is shown in Figure 2.1.

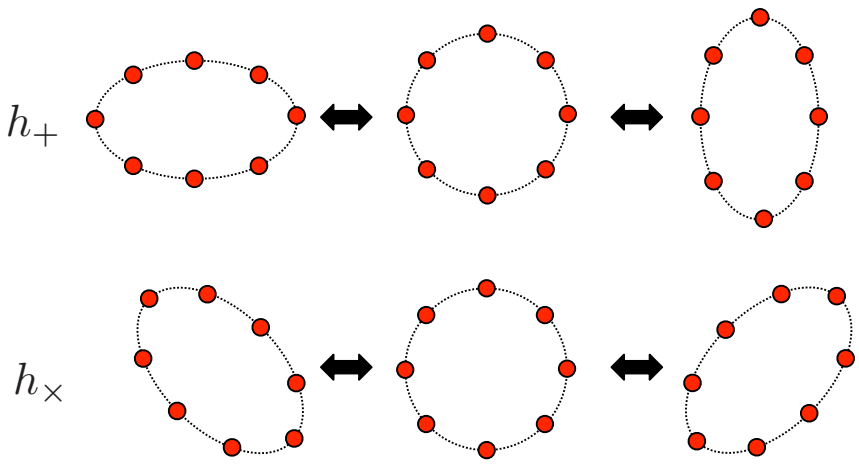

Figure 2.1: + mode and × mode of gravitational waves. Red points represent free masses and the gravitational waves are injected from the vertical direction to the sheet.

2.2 Generation of gravitational waves

The wave equation for GWs (2.7) indicates that GWs are generated from the energy momentum tensor $T_{\mu\nu}$. The solution of the wave equation can be written as

$$\overline{h}_{\mu\nu}(t, \boldsymbol{x}) = \frac{4G}{c} \int d^3\boldsymbol{x}' \frac{T_{\mu\nu}(t - |\boldsymbol{x} - \boldsymbol{x}'|/c, \boldsymbol{x}')}{|\boldsymbol{x} - \boldsymbol{x}'|}. \tag{2.22}$$

When the size of the GW source is much smaller than the GW wavelength, the equation above can be approximated as

$$h_{ij}(t, \boldsymbol{x}) = \frac{2G}{c^4 r} \ddot{Q}_{ij}(t - r/c), \tag{2.23}$$

where $r = |\boldsymbol{x}|$ and

$$Q_{ij}(t) = \int \rho(t, \boldsymbol{x}) \left(x_i x_j - \frac{1}{3} \delta_{ij} x^i x^j \right) d^3\boldsymbol{x} \tag{2.24}$$

is the quadrupole momentum of the GW source and ρ is the density of the GW source.

2.3 Astrophysical sources of gravitational waves

As the effect of GWs is extremely small, the main GW sources are astrophysical sources with significantly large quadrupole momentums. In this section, the main astrophysical sources of GWs are introduced.

Compact binary coalescence

The compact binary coalescence (CBC) is the merger the compact binary systems such as binary black hole (BBH), binary neutron star (BNS). All GW detections by LIGO and Virgo thus far are GWs from CBC. The CBC is composed of the following three phases: inspiral, merger, and ringdown. In the inspiral phase, the binary system is in circular orbit, and the orbit shrinks by losing its energy through the GWs. In the merger phase, the binary system merges emitting the largest GWs and forms a perturbed remnant compact object. In the ringdown phase, the perturbed remnant compact object relaxes to the stationary state by emitting the GWs. The ringdown of a remnant black hole is called the quasi normal mode.

When the component masses of CBC are m_1 and m_2, the strain of CBC in the inspiral phase is written as [19]

$$h(f) \simeq \frac{1}{\pi^{2/3}} \left(\frac{5}{24} \right)^{1/2} \frac{c}{r} \left(\frac{GM_c}{c^3} \right)^{5/6} f^{-7/6}, \tag{2.25}$$

where

$$M_c = \frac{(m_1 m_2)^{3/5}}{(m_1 + m_2)^{1/5}} \tag{2.26}$$

is called the chirp mass. Here, phase term of $h(f)$ is ignored.

The inspiral phase finishes at the innermost stable circular orbit (ISCO). The GW frequency at ISCO is as follows:

$$f_{\rm ISCO} = \frac{1}{12\sqrt{6}\pi}\frac{c^3}{GM} \tag{2.27}$$

$$= 2.2 \text{ kHz} \left(\frac{M_\odot}{M}\right), \tag{2.28}$$

where $M = m_1 + m_2$. The most sensitive frequency region of the current GW detectors is $\sim$ 10 Hz -1 kHz and thus the target mass of CBC is $\sim$ 1-100 $M_\odot$.

For $m_1 = m_2 = m$, the amplitude of GWs from CBC is

$$h(f) = 4.3 \times 10^{-24} \left(\frac{100 \text{ Mpc}}{r}\right) \left(\frac{m}{1.4\ M_\odot}\right)^{5/6} \left(\frac{100 \text{ Hz}}{f}\right)^{7/6}. \tag{2.29}$$

Pulsar

The pulsar is a rotating neutron star emitting periodic electromagnetic pulses. If the pulsar is not axisymmetric around the rotational axis, it generates GWs. The amplitude of the GWs from the pulsar is [19]

$$h(f) = \frac{4\pi^2 G}{c^4}\frac{I_{zz} f^2}{r}\epsilon, \tag{2.30}$$

where I_{zz} is the moment of inertia around the rotational axis (z axis) of the pulsar, $f_{\rm rot}$ is the rotational frequency of the pulsar, and $\epsilon = |I_{xx} - I_{yy}|/I_{zz}$ is the ellipticity of the pulsar (I_{xx} and I_{yy} are the moments of inertia around the x and y axes, which are orthogonal to the z axis). The GW frequency from the pulsar can be written as $f = 2f_{\rm rot}$.

The amplitude of the GWs from the pulsar with a typical galactic distance is

$$h = 1.1 \times 10^{-25} \left(\frac{\epsilon}{10^{-6}}\right) \left(\frac{I_{zz}}{10^{38} \text{ kg m}^2}\right) \left(\frac{10 \text{ kpc}}{r}\right) \left(\frac{f}{1 \text{ kHz}}\right)^2. \tag{2.31}$$

Supernova

The core collapse supernova (Type II supernova) can generate GWs if there is a non-axisymmetric mechanism in the supernova. The typical strain and frequency of the core collapse supernova is estimated to be $h \sim 10^{-22} - 10^{-21}$ and $\sim$ 1 kHz considering a distance of 10 kpc from the supernova [20].

Early universe

Another important GW source is the stochastic GW background from the early universe. Quantum fluctuation during inflation is one of the candidates that produces the stochastic

GW background. The strain of the stochastic GW background can be written as [19]

$$h(f) = \sqrt{\frac{3H_0^2}{4\pi^2}\frac{\Omega_{\rm gw}(f)}{f^3}}, \tag{2.32}$$

where $H_0 \sim 68$ km s^{-1}Mpc^{-1} is the Hubble constant and

$$\Omega_{\rm gw}(f) = \frac{1}{\rho_c}\frac{d\rho_{\rm gw}}{d(\log f)}, \tag{2.33}$$

where $\rho_{\rm gw}$ is the energy density of the stochastic GW background and ρ_c is the critical energy density for a flat universe,

$$\rho_c = \frac{3c^2H_0^2}{8\pi G}. \tag{2.34}$$

As $\Omega_{\rm gw}$ is estimated to be $\sim 10^{-15}$ [21], the strain of the stochastic GW background is

$$h(f) \sim 6 \times 10^{-25}\left(\frac{0.1\ {\rm Hz}}{f}\right)^{3/2}. \tag{2.35}$$

The equation above indicates that the amplitude of the stochastic GW background is larger at lower frequencies. However, this strain sensitivity is difficult to achieve in ground-based GW detectors because the sensitivity is limited by seismic noise at low frequencies. To avoid the seismic noise, a spaceborne GW detector called the DECIGO is planned [22]. The ultimate target of DECIGO is the stochastic GW background from the early universe.

2.4 Observations of gravitational waves

In 2015, Advanced LIGO observed gravitational waves from a BBH for the first time, as shown in Figure 2.2 [1].

LIGO and Virgo had observing runs three times thus far. The first observing run (O1) was from September 12, 2015 to January 19, 2016. The second observing run (O2) was from November 30, 2016 to August 25, 2017. The third observing run (O3) was from April 1, 2019 to March 27, 2020. There were 11 events, including a BNS merger, observed in O1 and O2 [3], and 39 events were observed in the first half of O3 (O3a) from April 1, 2019 to October 1, 2019 [6]. Cumulative GW events from O1 to O3a are shown in Figure 2.3. The significant increase of GW events from O2 to O3 was achieved by some upgrades, especially the injection of a squeezed vacuum field [10, 11].

Binary black hole merger

There are 46 binary black hole (BBH) mergers observed from O1 to O3a. The BBH merger rate estimated from the results from O1 to O3a is $\mathcal{R}_{\rm BBH} = 23.9^{+14.9}_{-8.6}$ Gpc^{-3} yr^{-1} [24].

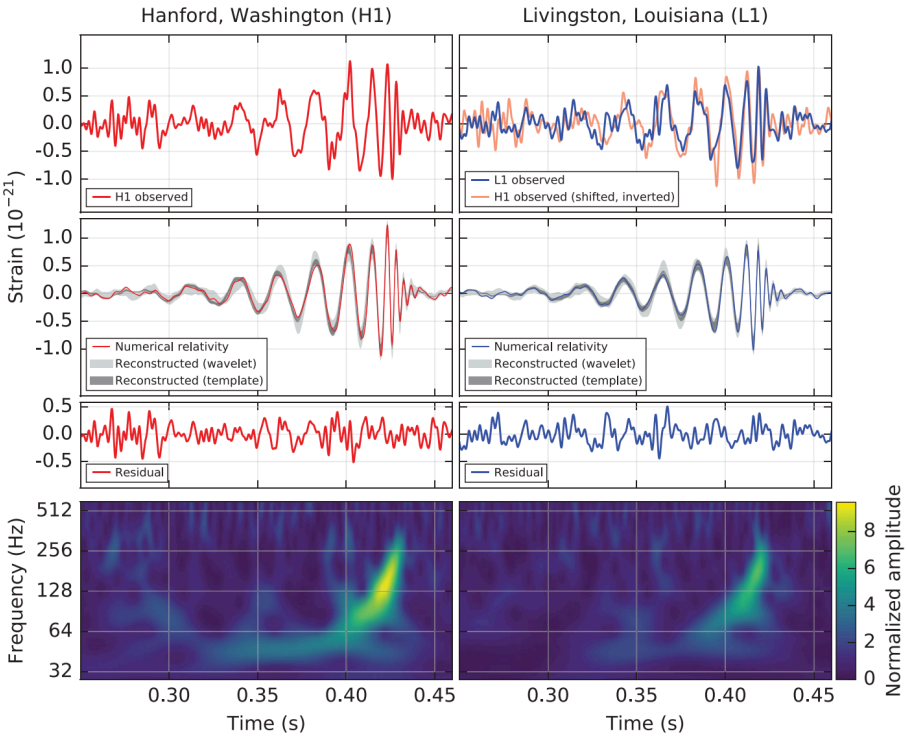

Figure 2.2: Observed chirp signals of GW150914 by Hanford and Livingston observatories of Advanced LIGO [1]. The left and right plots show the GW signals for Hanford and Livingston, respectively. The first and second plots from the top show the measured GW time series and calculated GW time series with numerical relativity, respectively. The second from the bottom plots show the residual GW signal after subtracting the calculated GW signal from the measured GW signal. The bottom plots show the GW frequency as a function of time. The GW frequency increases over time, which is why this GW signal is called the chirp signal.

Binary neutron star merger

There are two binary neutron star (BNS) mergers observed from O1 to O3a which are GW170817 [2] and GW190425 [29]. GW170817 was sufficiently localized by GW observation, which enabled the observations of the electromagnetic (EM) counterpart to the GW170817 with multiple wavelengths [30]. On the other hand, GW190425 was not sufficiently localized because one of the GW detectors were not working at the time of the event, and there was no observed EM counterpart to the GW190425 [29].

The BNS merger rate estimated from the results from O1 to O3a is $\mathcal{R}_{\rm BNS} = 320^{+490}_{-240}\ {\rm Gpc}^{-3}\ {\rm yr}^{-1}$ [24].

Neutron star black hole merger

There are two potential neutron star black hole (NSBH) mergers observed from O1 to O3a, which are GW190426_152155 [6] and GW190814 [25]. The component masses are 5.7 $M_\odot$ and 1.5 $M_\odot$ for GW190426_152155, and 23 $M_\odot$ and 2.6 $M_\odot$ for GW190814. The lower

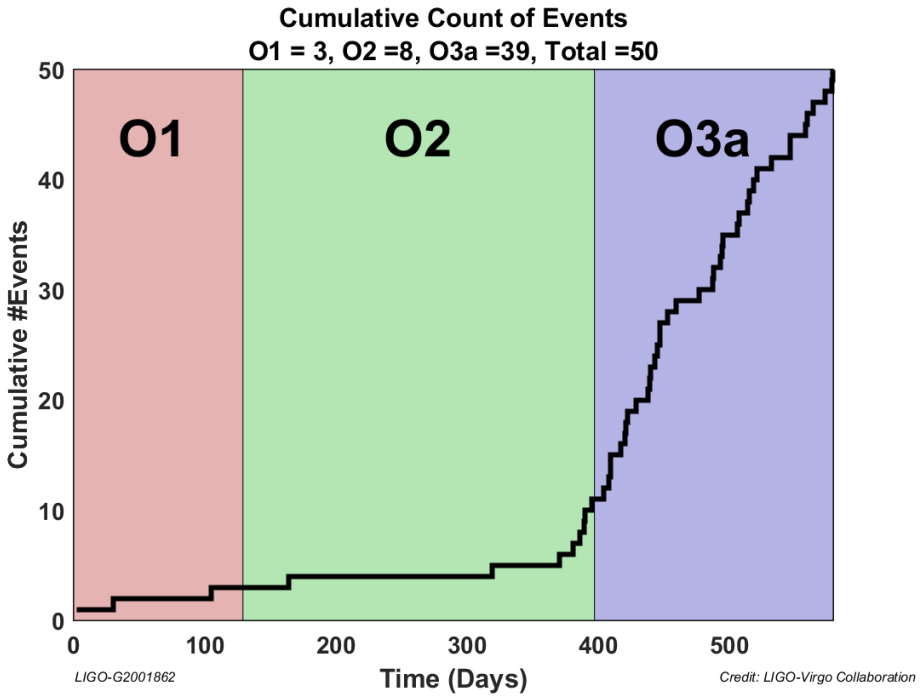

Figure 2.3: Cumulative GW events from O1 to O3a [23].

mass components of these events are either a neutron star or a black hole, and therefore, these events are either an NSBH or BBH merger.

2.5 Science from gravitational wave observations

Several scientific milestones were achieved from the GW observations, which will be presented in this section.

Population of compact objects

To understand the formation channel of compact objects and compact binary systems, the population of compact objects, such as mass and spin, provided crucial information. From GW observations, the compact objects were found in the wide mass range, which are not observed by EM. For example, the 2.6 $M_\odot$ compact object in GW190814 is in the mass gap region (called lower mass gap) between the neutron stars ($< 2.5M_\odot$) and the black holes ($> 5M_\odot$).

Tests of general relativity

GW observations of the compact binary coalescences enable the tests of general relativity in the strong gravity field. By using the binary black holes observed from O1 to O3a, tests of general relativity were conducted and several constraints on the general relativity were tighten [28]. However, there is still no evidence for violation of the general relativity.

Multi-messenger observation of a binary neutron star merger

As GW170817 was sufficiently localized, the EM counterparts to GW170817 were observed with multiple wavelengths [30]. Approximately 1.7 s after the BNS merger, a short gamma-ray burst (GRB 170817A) was observed [31]. This confirms that the BNS mergers are one of the progenitors of the short gamma-ray burst. Using the information on the time delay of GW170817 and GRB 170817A, the difference between the speed of gravity and the speed of light was constrained [31]. Another important EM observation related to GW170817 was an ultraviolet, optical, and infrared transient called kilonova [30]. The kilonova was caused by the radioactive decay of the r-process nuclei. This indicates that the BNS mergers are progenitors of heavy elements synthesized with the r-process.

Standard siren measurement

GW170817 enabled the first measurement of the Hubble constant with gravitational waves [32]. The distance to the source of GW170817 d was obtained from the GW observation, and the Hubble flow velocity of the corresponding GW source v_H was obtained from the EM observation. Using Hubble's law $v_H = H_0 d$, the Hubble constant H_0 was determined to be $70.0^{+12.0}_{-8.0}$ km s^{-1}Mpc^{-1}. This measurement is consistent with existing measurements, while it is independent of them. Future GW observations will improve the precision of the Hubble constant measurement.

2.6 Observation scenario

In the future, the fourth observing run (O4) will start around 2022, and the fifth observing run (O5) will start around 2025, as shown in Figure 2.4. KAGRA will join the observing run from O4, and LIGO-India will join from O5 [8]. One of the major upgrades towards O4 and O5 in LIGO, Virgo, and KAGRA is the implementation of the frequency-dependent squeezing, which is the main topic of this thesis. In particular, LIGO and Virgo plan to install a 300 m filter cavity from O4.

Third-generation GW detectors, such as the Einstein Telescope [33] and Cosmic Explorer [34], are planned to operate in the 2030s. The arm lengths of these detectors are 10-40 km, and the sensitivity is an order of magnitude better than the current GW detectors, which will lead to an increase of approximately 1000 times the GW events. In third-generation GW detectors, frequency-dependent squeezing with kilometer-scale filter cavities is planned to be installed for quantum noise reduction [35, 36].

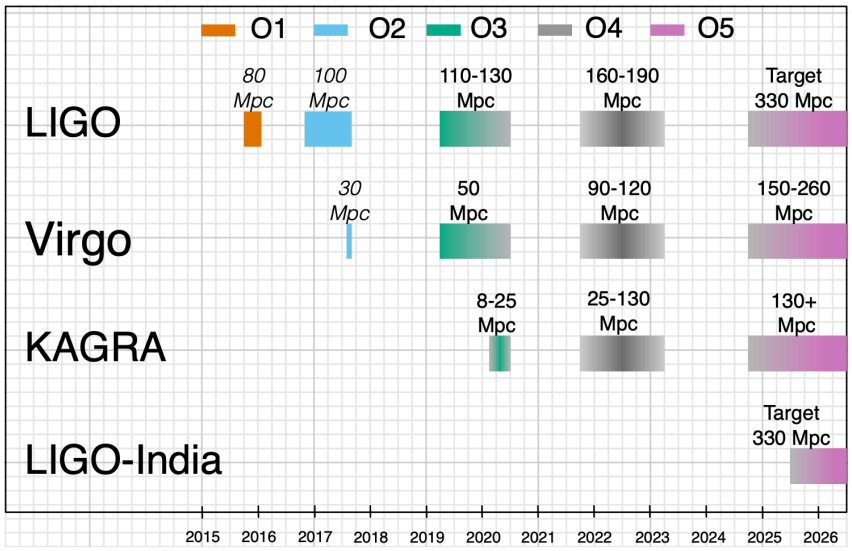

Figure 2.4: Observation scenario of GW detectors [8]. In this figure, KAGRA was expected to join O3, but actually KAGRA could not join O3 due to the early end of O3, although the BNS range of KAGRA reached around 1 Mpc.

Chapter 3

Gravitational-Wave Detector

The basic principle of ground-based GW detectors is the Michelson interferometer, which can measure the differential motion of test masses and is thus suitable to measure the motion induced by GWs. The configuration of the current GW detectors is called the dual recycled Fabry-Perot Michelson interferometer (DRFPMI). In this chapter, the principle of the interferometric GW detectors is presented.

3.1 Michelson interferometer

A configuration of the Michelson interferometer is shown in Figure 3.1.

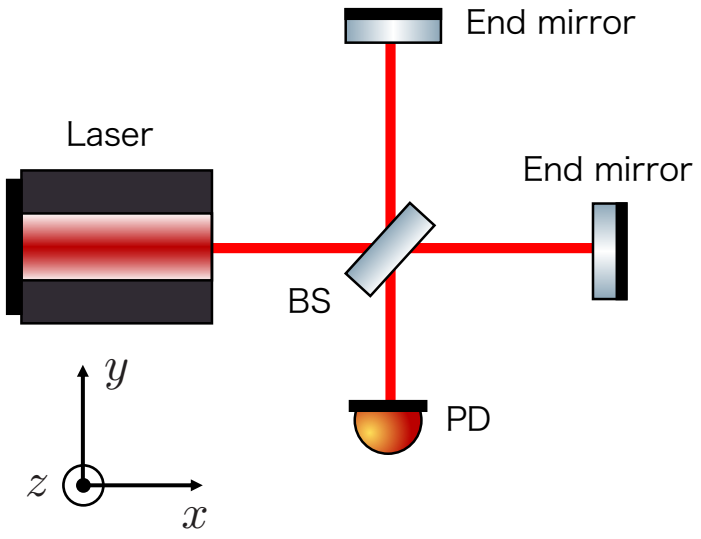

Figure 3.1: Configuration of the Michelson interferometer.

For simplicity, the splitting ratio of a beam splitter (BS) is assumed to be 50:50, and the reflectivity of the end mirror is 1. In Figure 3.1, when the arm length (distance between BS and end mirror) in the x-axis (horizontal) direction is L_x and the arm length in the

y-axis (vertical) direction is L_y, and the carrier laser frequency is ω_0, the round-trip phase between the BS and end mirror in x-arm and y-arm are $\phi_x = 2L_x\omega_0/c$ and $\phi_y = 2L_y\omega_0/c$, respectively. The electric field at an anti-symmetric port (AS port) is

$$\begin{aligned} E_{\rm AS} &= \frac{1}{2}E_0(e^{-i\phi_x} - e^{-i\phi_y}) \\ &= -iE_0 e^{-i\frac{\phi_+}{2}} \sin\frac{\phi_-}{2}, \end{aligned} \tag{3.1}$$

where E_0 is the input electric field and $\phi_+ \equiv \phi_x + \phi_y$, $\phi_- \equiv \phi_x - \phi_y$ are defined.

The carrier power at the AS port is

$$P_{\rm AS} = |E_{\rm AS}|^2 = P_0 \sin^2\frac{\phi_-}{2}, \tag{3.2}$$

where $P_0 = |E_0|^2$. The carrier power at the AS port only depends on the differential arm length in the x and y arms. The point where the carrier power at the AS port is 0 ($\phi_- = 2n\pi$, n: integer) is called the dark fringe, where all the injected carrier beam is reflected back to the injection port. This condition is necessary for the power recycling technique, which will be presented in Section 3.3.

3.1.1 Response to gravitational waves

In this section, we consider a response of a Michelson interferometer to GWs. We assume that GWs only have the plus mode and propagate in the z direction.

The spacetime interval in the TT gauge is

$$ds^2 = -c^2dt^2 + (1+h)dx^2 + (1-h)dy^2 + dz^2. \tag{3.3}$$

As light travels along the null geodesics: $ds^2 = 0$, the light in x arm obeys the following equation:

$$\frac{dx}{dt} = \pm\frac{c}{\sqrt{1+h}} \simeq \pm c\left(1 - \frac{1}{2}h\right), \tag{3.4}$$

where $\pm$ represents the light propagating in the $\pm x$ direction.

The round-trip phase for x arm is

$$\begin{aligned} \phi_x(t) &= \omega_0 \int_{\rm roundtrip} \left(\frac{dx}{dt}\right)^{-1} dx \\ &= \frac{2L_x\omega_0}{c} + \frac{\omega_0}{2}\int_{t-2L/c}^{t} h(t')dt', \end{aligned} \tag{3.5}$$

where $L_x \simeq L = (L_x + L_y)/2$ is assumed. Similarly, the round-trip phase for y arm is

$$\phi_y(t) = \frac{2L_y\omega_0}{c} - \frac{\omega_0}{2}\int_{t-2L/c}^{t} h(t')dt'. \tag{3.6}$$

Therefore, the electric field at the AS port is

$$\begin{aligned} E_{\rm AS} &= \frac{1}{2}E_0(e^{-i\phi_x} - e^{-i\phi_y}) \\ &= \frac{1}{2}E_0 e^{-i\phi_x}[1 - e^{i(\phi_- + \phi_{\rm GW})}], \end{aligned} \tag{3.7}$$

where

$$\phi_- = \frac{2\omega_0(L_x - L_y)}{c}, \tag{3.8}$$

$$\phi_{\rm GW}(t) = \omega_0 \int_{t-2L/c}^{t} h(t')dt'. \tag{3.9}$$

Here, $\phi_{\rm GW}$ is the phase induced by GWs. Using the Fourier transformation of $h(t')$ in Equation (3.9),

$$\begin{aligned} \phi_{\rm GW}(t) &= \omega_0 \int_{t-2L/c}^{t} \int_{-\infty}^{\infty} h(\omega) e^{i\omega t'} d\omega dt' \\ &= \int_{-\infty}^{\infty} H_{\rm MI}(\omega) h(\omega) e^{i\omega t} d\omega, \end{aligned} \tag{3.10}$$

where

$$H_{\rm MI}(\omega) = \frac{2\omega_0 L}{c} \frac{\sin(\omega L/c)}{\omega L/c} e^{-i\omega L/c} \tag{3.11}$$

is the frequency response of a Michelson interferometer to GWs. This response is maximum when $\omega L/c = \pi/2$. The optimal arm length for $f = 100$ Hz of GW frequency is $L = 750$ km. This arm length is not a realistic value to build it on Earth. To increase the effective arm length, Fabry-Perot cavities are used in current GW detectors, which will be presented in Section 3.2. Although the cavity length of the current GW detectors is only 3-4 km, the effective arm length is significantly enhanced by the cavity.

For $\omega \ll c/L$, which is the case for $f = 100$ Hz and $L = 3$-4 km, Equation (3.11) is

$$H_{\rm MI}(\omega) = \frac{2\omega_0 L}{c}. \tag{3.12}$$

3.1.2 DC readout

From Equation (3.7), the power at the AS port in the dark fringe is

$$P_{\rm AS} = P_0 \sin^2 \frac{\phi_{\rm GW}}{2}. \tag{3.13}$$

In the dark fringe, the GW signal $\phi_{\rm GW}$ is second order at the AS port. To obtain a linear GW signal at the AS port, a DC readout technique [37] is used in the current GW detectors. In the DC readout, the Michelson interferometer is operated close to the dark fringe to enable the small carrier light to leak into the AS port. The power at the AS port

in the DC readout is

$$P_{\rm AS} = P_0 \sin^2 \frac{\phi_- + \phi_{\rm GW}}{2} \simeq \frac{P_0}{4}(\phi_-^2 + 2\phi_-\phi_{\rm GW}). \tag{3.14}$$

Therefore, a linear GW signal can be obtained.

3.2 Fabry-Perot cavity

As mentioned in the previous section, Fabry-Perot cavities are used in the current GW detectors to increase the effective arm length. The Fabry-Perot cavity is composed of two mirrors that reflect the beam back and forth between them and enhance the power inside the cavity. A configuration of the Fabry-Perot cavity is shown in Figure 3.2.

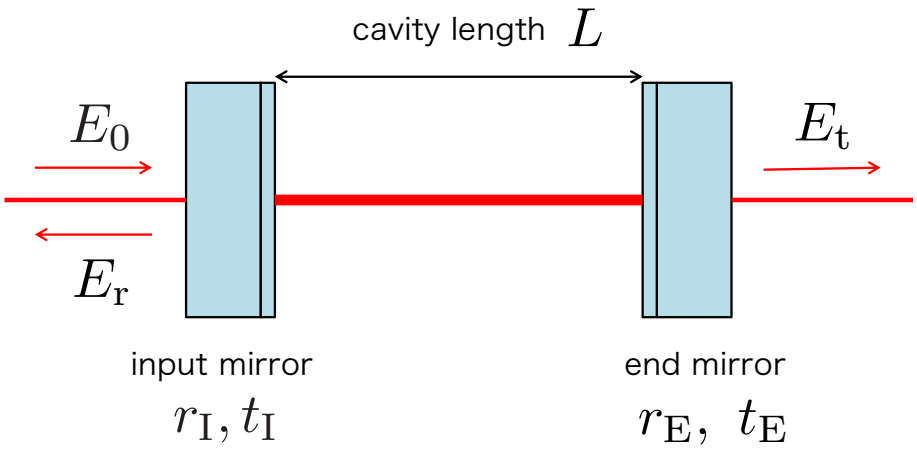

Figure 3.2: Configuration of the Fabry-Perot cavity. The Fabry-Perot cavity is composed of an input mirror and end mirror. We assume that the cavity length is L, the amplitude reflectivity and transmissivity of the input mirror are $r_{\rm I}$ and $t_{\rm I}$, respectively, and the amplitude reflectivity and transmissivity of the end mirror are $r_{\rm E}$ and $t_{\rm E}$, respevtively.

Firstly, we will not consider the effect of optical losses in the cavity. When the input electric field to the input mirror is E_0, the amplitude of the reflected field from the cavity is

$$\begin{aligned} E_{\rm r} &= E_0 r_{\rm I} - E_0 t_{\rm I}^2 r_{\rm E} e^{-i\phi} - E_0 t_{\rm I}^2 r_{\rm E}^2 r_{\rm I} e^{-2i\phi} - \cdots \\ &= E_0 r_{\rm I} - E_0 t_{\rm I}^2 r_{\rm E} e^{-i\phi} \sum_{n=0}^{\infty} (r_{\rm I} r_{\rm E} e^{-i\phi})^n \\ &= E_0 \left(r_{\rm I} - \frac{t_{\rm I}^2 r_{\rm E} e^{-i\phi}}{1 - r_{\rm I} r_{\rm E} e^{-i\phi}} \right), \end{aligned} \tag{3.15}$$

where ϕ is the round-trip phase in the cavity and can be written as follows:

$$\phi = \frac{2L\omega_0}{c}. \tag{3.16}$$

Similarly, the amplitude of the transmission field is

$$\begin{aligned} E_{\rm t} &= E_0 t_{\rm I} t_{\rm E} e^{-i\phi/2} \sum_{n=0}^{\infty} (r_{\rm I} r_{\rm E} e^{-i\phi})^n \\ &= E_0 \frac{t_{\rm I} t_{\rm E} e^{-i\phi/2}}{1 - r_{\rm I} r_{\rm E} e^{-i\phi}}. \end{aligned} \tag{3.17}$$

The amplitude reflectivity and transmissivity of a Fabry-Perot cavity $(r_{\rm FP}, t_{\rm FP})$ are

$$r_{\rm FP}(\phi) = r_{\rm I} - \frac{t_{\rm I}^2 r_{\rm E} e^{-i\phi}}{1 - r_{\rm I} r_{\rm E} e^{-i\phi}}, \tag{3.18}$$

$$t_{\rm FP}(\phi) = \frac{t_{\rm I} t_{\rm E} e^{-i\phi/2}}{1 - r_{\rm I} r_{\rm E} e^{-i\phi}}. \tag{3.19}$$

The transmission power is

$$\begin{aligned} P_{\rm t} &= |E_{\rm t}|^2 \\ &= \frac{(t_{\rm I} t_{\rm E})^2}{(1 - r_{\rm I} r_{\rm E})^2 + 4 r_{\rm I} r_{\rm E} \sin^2 \phi/2} P_0. \end{aligned} \tag{3.20}$$

The power transmissivity $|t_{\rm FP}(\phi)|^2$ as a function of the round-trip phase is shown in Figure 3.3.

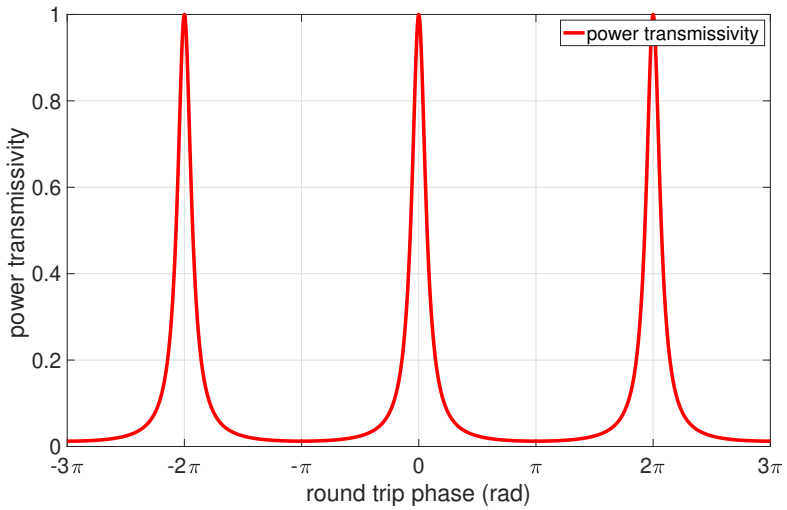

Figure 3.3: Power transmissivity of a Fabry-Perot cavity as a function of the round-trip phase. $r_{\rm I} = r_{\rm E} = 0.89$ is assumed.

When the Fabry-Perot cavity resonates, the transmission and the intracavity power are the maximum. The resonance condition is

$$\phi = 2\pi m \qquad (m = 1, 2, \cdots). \tag{3.21}$$

From Equation (3.16) and $\omega_0 = 2\pi c/\lambda_0$, this condition can be written as follows:

$$2L = m\lambda_0 \qquad (m = 1, 2, \cdots). \tag{3.22}$$

When the cavity length L is fixed, the transmission power changes periodically as a function of the laser frequency and this frequency period is called the free spectral range (FSR). From Equation (3.16) and (3.21), the FSR can be written as follows:

$$f_{\mathrm{FSR}} = \frac{\omega_{\mathrm{FSR}}}{2\pi} = \frac{c}{2L}. \tag{3.23}$$

From Equation (3.20), the full width at half maximum of the transmission power f_{FWHM} can be obtained by solving the following equation.

$$\frac{1}{1 + \dfrac{4r_{\mathrm{I}}r_{\mathrm{E}}}{(1 - r_{\mathrm{I}}r_{\mathrm{E}})^2} \sin^2\left(\dfrac{\pi L f_{\mathrm{FWHM}}}{c}\right)} = \frac{1}{2}. \tag{3.24}$$

Assuming $\dfrac{\pi L f_{\mathrm{FWHM}}}{c} = \dfrac{\pi f_{\mathrm{FWHM}}}{2 f_{\mathrm{FSR}}} \ll 1$ [1], we can expand the sine term as follows:

$$f_{\mathrm{FWHM}} = \frac{c(1 - r_{\mathrm{I}}r_{\mathrm{E}})}{2\pi L\sqrt{r_{\mathrm{I}}r_{\mathrm{E}}}}. \tag{3.25}$$

The ratio of f_{FSR} and f_{FWHM} represents the sharpness of the resonance and is called the finesse, which is

$$\mathcal{F} \equiv \frac{f_{\mathrm{FSR}}}{f_{\mathrm{FWHM}}} = \frac{\pi\sqrt{r_{\mathrm{I}}r_{\mathrm{E}}}}{1 - r_{\mathrm{I}}r_{\mathrm{E}}}. \tag{3.26}$$

When the intracavity loss T_{loss} is considered, the finesse (3.26) is

$$\mathcal{F} = \frac{\pi\sqrt{r}}{1 - r}, \tag{3.27}$$

where $r = r_{\mathrm{I}}r_{\mathrm{E}}r_{\mathrm{loss}}$ with $r_{\mathrm{loss}} = \sqrt{1 - T_{\mathrm{loss}}}$.

The cavity decay time is when the stored power inside the cavity is reduced by a factor of e^2 after turning off the input beam to the cavity [38]. The cavity transmission power after turning off the input beam can be written as follows:

$$P(t) = P_0 e^{-2t/\tau}, \tag{3.28}$$

where P_0 is the cavity transmission power before turning off the input beam and τ is the cavity decay time.

The decay time is written as follows:

$$\tau = \frac{\mathcal{F}}{\pi f_{\mathrm{FSR}}} = \frac{1}{\pi f_{\mathrm{FWHM}}}. \tag{3.29}$$

[1] This corresponds to $\mathcal{F} \gg 1$ in Equation (3.26)

This cavity decay time can be directly measured by turning off the input beam to the cavity and measuring the transmission or reflection beam from the cavity. This measurement is called a ringdown.

The finesse of a cavity is often measured by scanning the cavity length or the laser frequency, and measuring the time series of the transmission power from the cavity, as shown in Figure 3.3. This measurement is called cavity scan. From Equation (3.20), the time series of the transmission beam from the cavity can be written as follows:

$$T(t) = \frac{a}{1 + 4(\frac{\mathcal{F}}{\pi})^2 \sin^2(\frac{\pi(t-t_0)}{t_{\rm FSR}})}, \tag{3.30}$$

where a is the amplitude of the peak height, t_0 is the time offset depending on the starting time of the scan, and $t_{\rm FSR}$ is the time difference of the free spectral range. By fitting the measured data with this function, the finesse can be obtained.

3.2.1 Response to gravitational waves

In this section, we consider a response of a Fabry-Perot cavity to the GWs. For simplicity, we ignore the losses in the cavity. We assume that GWs only have the plus mode and propagate in the z direction and the Fabry-Perot cavity is placed along the x direction.

The phase for the beam with round trips in the cavity n times is

$$\phi_n(t) = \frac{2L\omega_0 n}{c} + \frac{\omega_0}{2}\int_{t-2Ln/c}^{t} h(t')dt'. \tag{3.31}$$

The amplitude reflectivity of the cavity around the resonance is

$$\begin{aligned}
r_{\rm FP} &= r_{\rm I} - t_{\rm I}^2 r_{\rm E}\sum_{n=1}^{\infty} r_{\rm I}^{n-1} r_{\rm E}^{n-1} e^{-i\phi_n} \\
&\simeq r_{\rm I} - t_{\rm I}^2 r_{\rm E}\sum_{n=1}^{\infty} r_{\rm I}^{n-1} r_{\rm E}^{n-1}\left(1 - i\frac{\omega_0}{2}\int_{t-2Ln/c}^{t} h(t')dt'\right) \\
&= \frac{r_{\rm I} - r_{\rm E}}{1 - r_{\rm I} r_{\rm E}} + i(t_{\rm I}^2 r_{\rm E})\frac{\omega_0}{2}\sum_{n=1}^{\infty} r_{\rm I}^{n-1} r_{\rm E}^{n-1}\int_{t-2Ln/c}^{t}\int_{-\infty}^{\infty} h(\omega)e^{i\omega t'}d\omega dt' \\
&= \frac{r_{\rm I} - r_{\rm E}}{1 - r_{\rm I} r_{\rm E}}\left(1 + i\int_{-\infty}^{\infty} H_{\rm FP}(\omega)h(\omega)e^{i\omega t}d\omega\right),
\end{aligned} \tag{3.32}$$

where

$$H_{\rm FP}(\omega) = \frac{\omega_0 L}{c}\frac{t_{\rm I}^2 r_{\rm E}}{(r_{\rm I} - r_{\rm E})(1 - r_{\rm I} r_{\rm E} e^{-2i\omega L/c})}\frac{\sin(\omega L/c)}{\omega L/c}e^{-i\omega L/c} \tag{3.33}$$

is the frequency response of a Fabry-Perot cavity to the GWs. In the case of $\omega L/c \ll 1$, $r_{\rm I} \simeq 1$, and $r_{\rm E} = 1$,

$$H_{\rm FP}(\omega) = -\frac{2\omega_0 L}{c}\frac{\mathcal{F}}{\pi}\frac{1}{1 + i\omega/\omega_p}, \tag{3.34}$$

where

$$f_p = \frac{\omega_p}{2\pi} = \frac{c}{4L\mathcal{F}} = \frac{f_{\mathrm{FWHM}}}{2} \tag{3.35}$$

is called the cavity pole. The frequency response of the Fabry-Perot cavity is the first-order low pass filter with a cutoff frequency f_p for GWs (also for cavity length noise and laser frequency noise). When we compare Equation (3.34) with Equation (3.12), the response of the Fabry-Perot cavity is enhanced by $\mathcal{F}/\pi$ with respect to the Michelson interferometer with the same arm length.

In current GW detectors, the Fabry-Perot cavities are used for arms of the Michelson interferometer, as shown in Figure 3.4. The response of the Fabry-Perot Michelson interferometer (FPMI) is enhanced by $2\mathcal{F}/\pi$ compared to the Michelson interferometer with the same arm length.

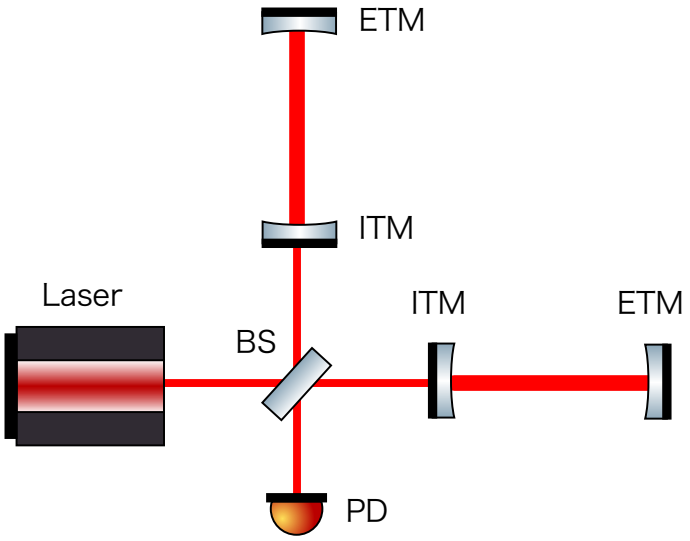

Figure 3.4: Configuration of a Fabry-Perot Michelson interferometer. There are two Fabry-Perot cavities used for the arms of the Michelson interferometer to enhance the effective arm length.

3.2.2 Pound-Drever-Hall technique

The Pound-Drever-Hall (PDH) technique is used to obtain the phase difference between a cavity resonance and injection beam and to keep the cavity resonate [39]. An example configuration of the PDH technique is shown in Figure 3.5.

The phase modulated injection beam is

$$\begin{aligned} E &= E_0 e^{i(\omega t + \beta \sin \Omega t)} \\ &\simeq E_0[J_0(\beta)e^{i\omega t} + J_1(\beta)e^{i(\omega+\Omega)t} - J_1(\beta)e^{i(\omega-\Omega)t}], \end{aligned} \tag{3.36}$$

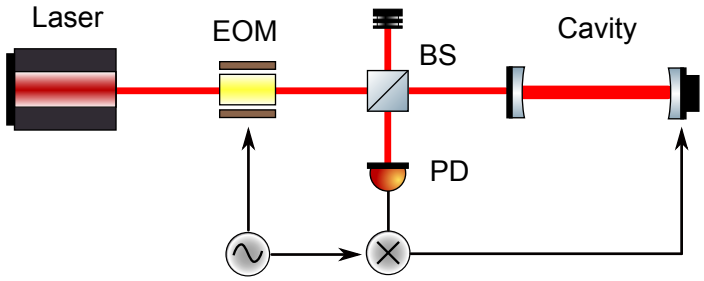

Figure 3.5: Example configuration of the PDH technique. The phase difference between the cavity resonance and the injection beam $\delta\phi$ can be obtained by modulating the phase of the injection beam using an electro-optic modulator (EOM) and demodulating the reflected beam from the cavity at the modulation frequency. The PDH signal is fed back to the cavity length to maintain the cavity resonance.

where β is the modulation depth, Ω is the modulation frequency, and J_n is the n-th order Bessel function of the first kind. From Equation (3.18), the reflected power from the cavity is

$$\begin{aligned} P_{\mathrm{r}} &= P_0 \left| J_0(\beta) r(\omega) e^{-i\omega t} + J_1(\beta) r(\omega+\Omega) e^{-i(\omega+\Omega)t} - J_1(\beta) r(\omega-\Omega) e^{-i(\omega-\Omega)t} \right|^2 \\ &= P_0 (|J_0(\beta) r(\omega)|^2 + |J_1(\beta) r(\omega+\Omega)|^2 + |J_1(\beta) r(\omega-\Omega)|^2) \\ &\quad + 2P_0 J_0(\beta) J_1(\beta) \{ \mathrm{Re}[r(\omega) r^*(\omega+\Omega) - r^*(\omega) r(\omega-\Omega)] \cos\Omega t \\ &\quad + \mathrm{Im}[r(\omega) r^*(\omega+\Omega) - r^*(\omega) r(\omega-\Omega)] \sin\Omega t \} + (2\Omega \quad \text{terms}). \end{aligned} \tag{3.37}$$

In Equation (3.37), the phase information of the carrier is included in the Ω terms, which are the beat notes of the carrier and sidebands. By demodulating the reflected signal with $\sin\Omega t$, the PDH signal in phase can be obtained as follows:

$$P^{\mathrm{I}}_{\mathrm{demod}} = P_0 J_0(\beta) J_1(\beta)\ \mathrm{Im}\{r(\omega) r^*(\omega+\Omega) - r^*(\omega) r(\omega-\Omega)\}. \tag{3.38}$$

By demodulating the reflected light with $\cos\Omega t$, the PDH signal in the quadrature phase is

$$P^{\mathrm{Q}}_{\mathrm{demod}} = P_0 J_0(\beta) J_1(\beta)\ \mathrm{Re}\{r(\omega) r^*(\omega+\Omega) - r^*(\omega) r(\omega-\Omega)\}. \tag{3.39}$$

When the modulation frequency is significantly larger than the cavity linewidth ($\Omega \gg \omega_{\mathrm{FWHM}}$) and the carrier is around the resonance, the sidebands are off resonance of the cavity and nearly completely reflected by the cavity ($r(\omega \pm \Omega) \simeq 1$). Therefore,

$$r(\omega) r^*(\omega+\Omega) - r^*(\omega) r(\omega-\Omega) \simeq i2\ \mathrm{Im}\{r(\omega)\}. \tag{3.40}$$

In this case, the Q phase PDH signal (3.39) disappears. The I phase PDH signal (3.38) is

$$\begin{aligned} P^{\mathrm{I}}_{\mathrm{demod}} &\simeq 2P_0 J_0(\beta)J_1(\beta)\ \mathrm{Im}\{r(\omega)\} \\ &= \frac{2P_0 J_0(\beta)J_1(\beta)\ t_{\mathrm{I}}^2 r_{\mathrm{E}} \sin\phi}{1 + r_{\mathrm{I}}^2 r_{\mathrm{E}}^2 - 2r_{\mathrm{I}} r_{\mathrm{E}} \cos\phi} \\ &\simeq \frac{4P_0 J_0(\beta)J_1(\beta) t_{\mathrm{I}}^2 r_{\mathrm{E}}}{(1 - r_{\mathrm{I}} r_{\mathrm{E}})^2}\delta\phi, \end{aligned} \tag{3.41}$$

where $\phi = \delta\phi \ll 1$ is assumed. The PDH signal is proportional to $\delta\phi$ around the resonance.

The intracavity power and the normalized PDH signals (In-phase, Quadrature) are shown in Figure 3.6.

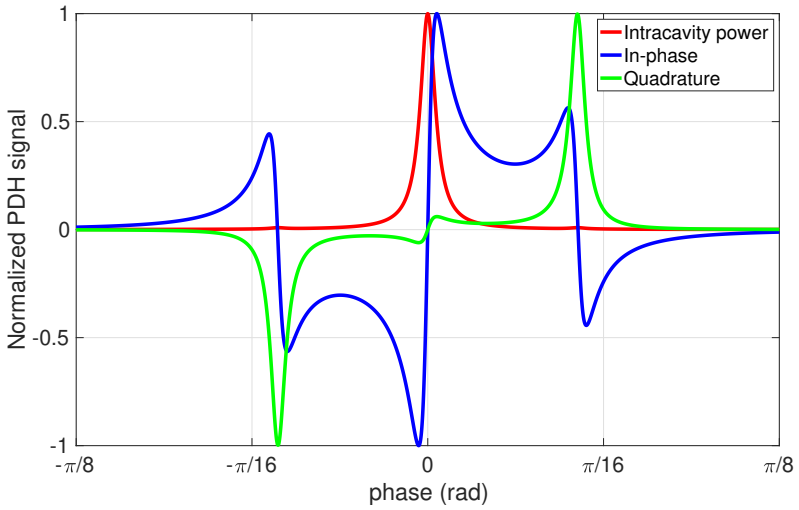

Figure 3.6: Normalized PDH signal of the Fabry-Perot cavity. The red line represents the intracavity power normalized with respect to its maximum intracavity power. The blue and green lines represent the PDH signals (in-phase and quadrature) normalized with respect to $P_0 J_0(\beta)J_1(\beta)$. It is assumed that the laser wavelength is $\lambda = 1064$ nm, the cavity length is $L = 4$ cm, the mirrors reflectivity is $r_{\mathrm{I}} = r_{\mathrm{E}} = \sqrt{0.9999}$, the cavity linewidth is $f_{\mathrm{FWHM}} = 8$ MHz, the modulation frequency is $\Omega/2\pi = 100$ MHz, and the modulation depth is $\beta = 0.15$ rad.

3.3 Configuration of GW detectors

The standard configuration of the current GW detectors is called the dual recycled Fabry-Perot Michelson interferometer (DRFPMI). The configuration of DRFPMI is shown in Figure 3.7. Two additional mirrors, called the power recycling and signal recycling mirrors, are placed in the FPMI.

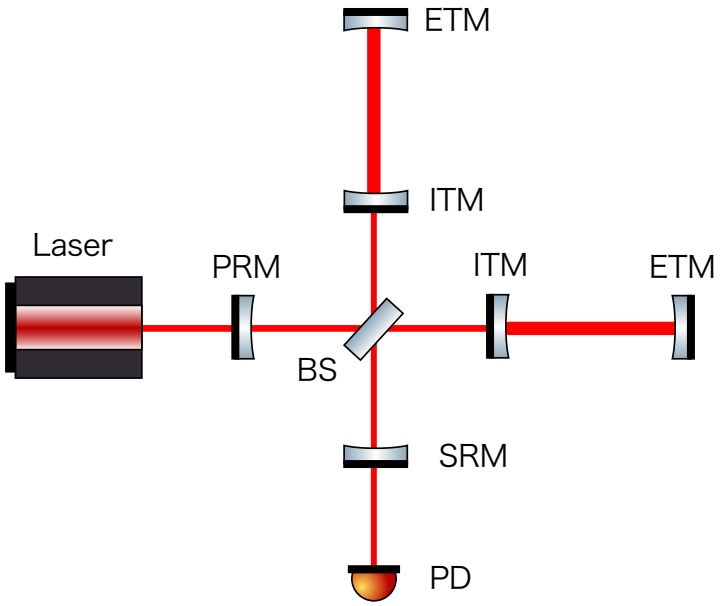

Figure 3.7: Configuration of DRFPMI. In addition to the FPMI, there are two additional mirrors called the power recycling mirror and signal recycling mirror.

Power recycling

The power recycling mirror (PRM) is placed at the injection port of the interferometer and reflects back the laser to the interferometer. The PRM and input test mass (ITMs) form a cavity called the power recycling cavity (PRC). When the carrier field is anti-resonant inside the PRC, the power recycling effectively increases the injection laser power.

Signal recycling

The signal recycling mirror (SRM) is placed at the anti-symmetric port of the interferometer and reflects the GW signal to the interferometer. The SRM and ITMs form a cavity called the signal recycling cavity (SRC). When GW sidebands are resonant inside the SRC, the effective bandwidth of the arm cavity is increased because the effective ITM reflectivity is reduced for the GW sidebands. This technique is called the resonant sideband extraction (RSE). The effective bandwidth of the arm cavity with RSE can be written as follows:

$$\gamma_{\mathrm{ifo}} = \frac{1 + r_{\mathrm{sr}}}{1 - r_{\mathrm{sr}}} \gamma_{\mathrm{arm}}, \tag{3.42}$$

where r_{sr} is the amplitude reflectivity of the SRM and γ_{arm} is the arm cavity half bandwidth. The interferometer bandwidth can be increased with RSE.

3.4 Noise sources in GW detectors

There are several noise sources in GW detectors. In this section, the following three main noise sources in GW detectors will be introduced: quantum noise, seismic noise, and thermal noise.

Quantum noise

The quantum noise is fundamental noise originated from the quantum fluctuation of light. It is composed of shot noise and radiation pressure noise. In a semi-classical picture, the shot noise is the photon counting noise in a photo detector, and the radiation pressure noise is the mirror fluctuation owing to the fluctuation of the photon number hitting on the mirror. In a quantum picture, the origin of the quantum noise is the vacuum field entering the output port of the interferometer [9]. Details of the quantum noise are presented in Chapter 5.

Seismic noise

The seismic noise originates from the mirror fluctuation owing to the seismic motion of the ground. Test masses in GW detectors are suspended by multiple pendulums to isolate the test masses from seismic noise. As the seismic noise below the resonant frequency of a suspension (which is usually an order of 1 Hz) cannot be isolated, it is a significant noise source at low frequencies.

Thermal noise

The thermal noise is composed of the Brownian motion of the mirror substrate, mirror coating, and suspension wires. The ways to reduce the thermal noise are using high Q factor coating and suspension wires, and cooling down the mirrors and suspension wires. LIGO and Virgo operate at room temperature, while test masses are cooled down to 20 K in KAGRA to reduce the thermal noise.

3.5 Sensitivity of GW detectors

The design sensitivities of Advanced LIGO, Advanced Virgo, and KAGRA are shown in Figure 3.8-3.10. For all cases, quantum noise broadly limits the sensitivity and it is crucial to reduce the quantum noise to improve the sensitivity of GW detectors.

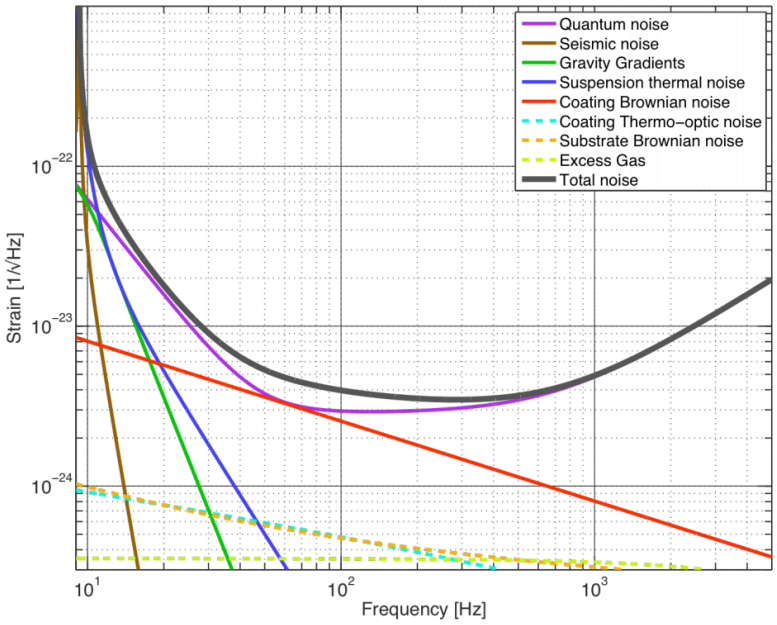

Figure 3.8: Design sensitivity of Advanced LIGO [4].

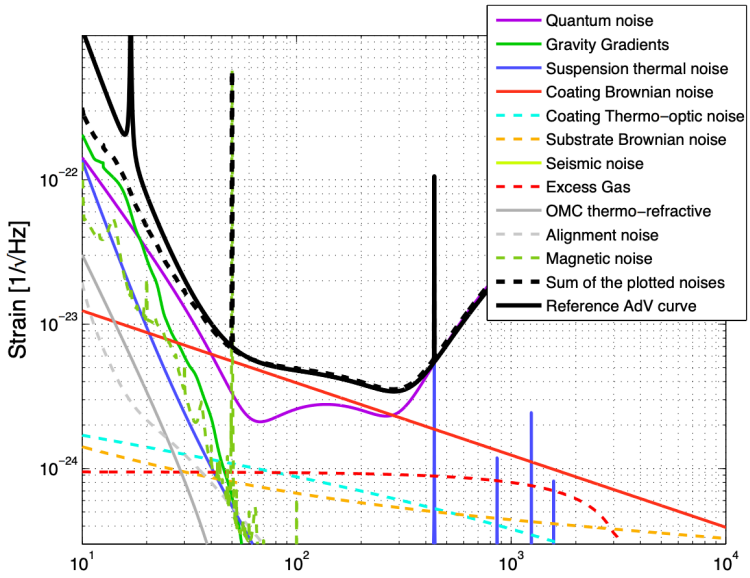

Figure 3.9: Design sensitivity of Advanced Virgo (AdV) [5].

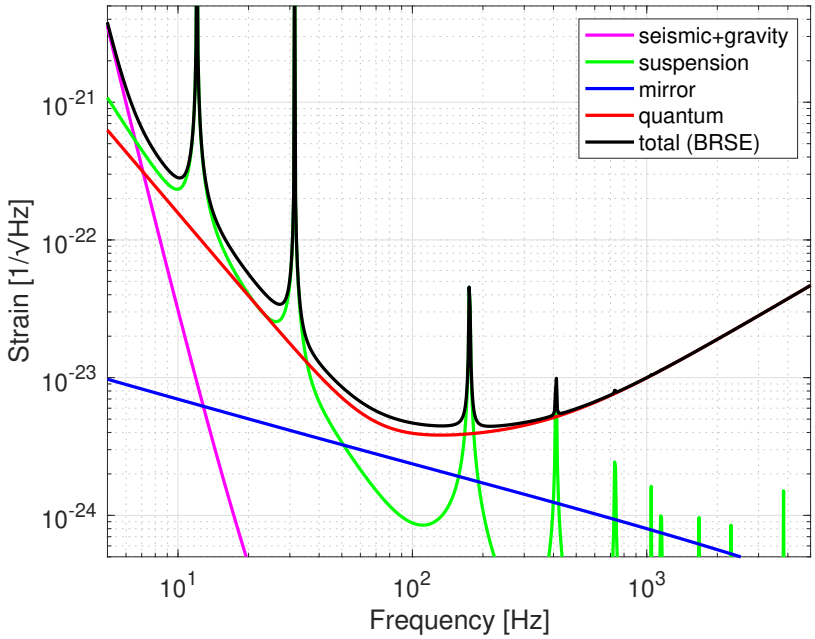

Figure 3.10: Design sensitivity of KAGRA (broadband RSE) [40].

Chapter 4

Theory of Quantum States of Light

Quantum noise in GW detectors originates from the vacuum field entering from the output port of the interferometer. To understand the quantum noise in GW detectors and how to reduce it, the basics of the quantum states of light are presented in this chapter.

4.1 Quantization of the electromagnetic field

In this section, we present the quantization of the electromagnetic field. The formalism used in this chapter (and throughout this thesis) is based on [14].

Quantized electric field can be written as follows:

$$E(t) = \int_0^\infty \sqrt{\frac{2\pi\hbar\omega}{Ac}} a(\omega) e^{-i\omega t} \frac{d\omega}{2\pi} + \text{h.c.}, \tag{4.1}$$

where A is the effective cross-sectional area of the electric field and $a(\omega)$ is the annihilation operator for a photon whose frequency is ω. h.c. indicates the Hermitian conjugate. The commutation relation of $a(\omega)$ is

$$[a(\omega), a(\omega')] = 0, \ [a(\omega), a^\dagger(\omega')] = 2\pi\delta(\omega - \omega'). \tag{4.2}$$

We consider a carrier field whose frequency is ω_0 and its sidebands whose frequencies are $\omega_0 \pm \Omega$. In GW detectors, the carrier frequency is $\omega_0/(2\pi) \sim 300$ THz, while the frequency of a GW signal is $\Omega \sim 10 - 10$ kHz, and thus, we can assume $\Omega \ll \omega_0$. In this sideband picture, Equation (4.1) can be written as follows:

$$E(t) = e^{-i\omega_0 t} \sqrt{\frac{2\pi\hbar\omega_0}{Ac}} \int_0^\infty [a_+ e^{-i\Omega t} + a_- e^{i\Omega t}] \frac{d\Omega}{2\pi} + \text{h.c.}, \tag{4.3}$$

where $a_+ = a(\Omega)$ and $a_- = a(-\Omega)$ are annihilation operators for the upper and lower sidebands. Here, we approximated $\omega_0 \pm \Omega \simeq \omega_0$ inside the square root. Formalism using operators a_+, a_- is called one-photon formalism as each operator acts on only one photon.

Using the annihilation and creation operators for the upper and lower sidebands, we can define

$$a_1(\Omega) = \frac{a_+ + a_-^\dagger}{\sqrt{2}},\ a_2(\Omega) = \frac{a_+ - a_-^\dagger}{\sqrt{2}i}. \tag{4.4}$$

In the time domain,

$$a_1(t) = \frac{a(t) + a^\dagger(t)}{\sqrt{2}},\ a_2(t) = \frac{a(t) - a^\dagger(t)}{\sqrt{2}i}. \tag{4.5}$$

A formalism using operators a_1, a_2 is called two-photon formalism because each operator acts on two photons, which are the upper and lower sidebands [41, 42]. The two-photon formalism is used throughout this thesis as it is useful for describing the squeezed vacuum states and calculating the quantum noise in GW detectors.

The commutation relation in the two-photon formalism is

$$[a_1, a_{2'}^\dagger] = -[a_2, a_{1'}^\dagger] = i2\pi\delta(\Omega - \Omega'), \tag{4.6}$$

$$[a_1, a_{1'}] = [a_1, a_{1'}^\dagger] = [a_{1'}^\dagger, a_{1'}^\dagger] = [a_{1'}^\dagger, a_{2'}^\dagger] = [a_1, a_{2'}] = 0, \tag{4.7}$$

and similarly, with $1 \leftrightarrow 2$.

The electric field (4.3) can be written in terms of the two-photon formalism as follows:

$$E(t) = \sqrt{\frac{4\pi\hbar\omega_0}{Ac}}\{a_1(t)\cos(\omega_0 t) + a_2(t)\sin(\omega_0 t)\}, \tag{4.8}$$

where

$$a_{1,2}(t) = \int_0^\infty \left[a_{1,2}(\Omega)e^{-i\Omega t} + a_{1,2}^\dagger(-\Omega)e^{i\Omega t}\right]\frac{d\Omega}{2\pi}. \tag{4.9}$$

When the carrier electric field is in the cosine quadrature, $a_1(t)$ is the amplitude modulation and $a_2(t)$ is the phase modulation for the carrier. Conventionally, a_1 is called the amplitude quadrature and a_2 is called the phase quadrature.

4.2 Heisenberg uncertainty principle

For an arbitrary Hermitian operator A and an arbitrary state $|\psi\rangle$, we define the uncertainty of the operator as

$$\Delta A = A - \langle A \rangle, \tag{4.10}$$

where $\langle A\rangle = \langle\psi| A |\psi\rangle$ is the expectation value of A for state $|\psi\rangle$. The variance of the operator is defined as follows:

$$\langle(\Delta A)^2\rangle = \langle A^2\rangle - \langle A\rangle^2 . \tag{4.11}$$

According to the Heisenberg uncertainty principle, for arbitrary Hermitian operators A and B, and an arbitrary state $|\psi\rangle$,

$$\langle(\Delta A)^2\rangle \langle(\Delta B)^2\rangle \geq \frac{1}{4}| \langle[A, B]\rangle |^2. \tag{4.12}$$

As the commutation relation for $a, a^\dagger$ in the time domain is $[a, a^\dagger] = 1$, the commutation relation for the quadrature operators is $[a_1, a_2] = i$. The uncertainty principle for the quadrature operators is

$$\langle(\Delta a_1)^2\rangle \langle(\Delta a_2)^2\rangle \geq \frac{1}{4}| \langle[a_1, a_2]\rangle |^2 = \frac{1}{4}. \tag{4.13}$$

This indicates that the product of variances of the amplitude and phase quadratures has an unavoidable lower limit for any states.

4.3 Quantum states of light

In this section, the basic quantum states of light, including Fock states, vacuum states, coherent states and squeezed states, are introduced.

4.3.1 Fock states and vacuum states

Fock states or number states $|n\rangle$ are defined as follows:

$$a |n\rangle = \sqrt{n} |n-1\rangle , \tag{4.14}$$

$$a^\dagger |n\rangle = \sqrt{n+1} |n+1\rangle , \tag{4.15}$$

$$N |n\rangle = n |n\rangle , \tag{4.16}$$

where $N = a^\dagger a$ is the number operator. The Fock states are orthogonal: $\langle n|m\rangle = \delta_{nm}$.

The vacuum states $|0\rangle$ are defined as follows:

$$a |0\rangle = 0. \tag{4.17}$$

The Fock states can be written in terms of the creation operator as follows:

$$|n\rangle = \frac{(a^\dagger)^n}{\sqrt{n!}} |0\rangle . \tag{4.18}$$

This indicates that there are n photons in the Fock states $|n\rangle$.

The expectation value and variance of a_1 and a_2 for the Fock states are

$$\langle n|\, a_1\, |n\rangle = \langle n|\, a_2\, |n\rangle = 0, \tag{4.19}$$

$$\langle n|\, (\Delta a_1)^2\, |n\rangle = \langle n|\, (\Delta a_2)^2\, |n\rangle = n + \frac{1}{2}. \tag{4.20}$$

The vacuum states $|0\rangle$ are the Fock states with no photon. Although the expectation value of the amplitude and phase quadratures for the vacuum states is 0, the vacuum states have an uncertainty in amplitude and phase quadratures owing to the Heisenberg uncertainty principle. This uncertainty of the vacuum states entering from the output port of the interferometer is the origin of the quantum noise in GW detectors.

4.3.2 Coherent states

Coherent states $|\alpha\rangle$ can be defined as the eigenstates of the annihilation operator as follows:

$$a\,|\alpha\rangle = \alpha\,|\alpha\rangle\,, \tag{4.21}$$

where α is an eigenvalue of a. Coherent states in the number state basis can be written as

$$|\alpha\rangle = e^{-|\alpha|^2/2} \sum_{n=0}^{\infty} \frac{\alpha^n}{\sqrt{n!}}\,|n\rangle\,. \tag{4.22}$$

The displacement operator from the vacuum states to the coherent states can be written as

$$D(\alpha)\,|0\rangle = |\alpha\rangle\,, \tag{4.23}$$

$$D(\alpha) = \exp\left(\alpha a^\dagger - \alpha^* a\right). \tag{4.24}$$

The expectation value and variance of a_1 and a_2 for the coherent states are

$$\langle \alpha|\, a_1\, |\alpha\rangle = \sqrt{2}\mathrm{Re}[\alpha], \tag{4.25}$$

$$\langle \alpha|\, a_2\, |\alpha\rangle = \sqrt{2}\mathrm{Im}[\alpha], \tag{4.26}$$

$$\langle \alpha|\, (\Delta a_1)^2\, |\alpha\rangle = \langle \alpha|\, (\Delta a_2)^2\, |\alpha\rangle = \frac{1}{2}. \tag{4.27}$$

The coherent states have an equal uncertainty for the amplitude and phase quadrature, and the product of the uncertainty for the amplitude and phase quadrature is the minimum value allowed by the uncertainty principle.

4.3.3 Squeezed states

The operator for the squeezed states can be written as

$$S(r,\phi) = \exp\left(\frac{1}{2} r e^{-2i\phi} a^2 - \frac{1}{2} r e^{2i\phi} a^{\dagger 2}\right), \tag{4.28}$$

where r is the squeezing factor and ϕ is the squeezing angle. Using the operator for the squeezed states, the amplitude and phase quadrature evolve as follows:

$$S(r,\phi)^\dagger a_1 S(r,\phi) = a_1(\cosh r - \sinh r \cos 2\phi) - a_2 \sinh r \sin 2\phi, \quad (4.29)$$
$$S(r,\phi)^\dagger a_2 S(r,\phi) = a_2(\cosh r + \sinh r \cos 2\phi) - a_1 \sinh r \sin 2\phi. \quad (4.30)$$

In the case of $\phi = 0$,

$$S(r)^\dagger a_1 S(r) = a_1 e^{-r}, \quad (4.31)$$
$$S(r)^\dagger a_2 S(r) = a_2 e^{r}. \quad (4.32)$$

The expectation value and variance of a_1 and a_2 in the squeezed states are as follows:

$$\langle 0| S(r)^\dagger a_1 S(r) |0\rangle = \langle 0| S(r)^\dagger a_2 S(r) |0\rangle = 0, \quad (4.33)$$
$$\langle 0| S(r)^\dagger (\Delta a_1)^2 S(r) |0\rangle = \frac{1}{2} e^{-2r}, \quad (4.34)$$
$$\langle 0| S(r)^\dagger (\Delta a_2)^2 S(r) |0\rangle = \frac{1}{2} e^{2r}. \quad (4.35)$$

Compared to the vacuum states, the variance of the amplitude quadrature in the squeezed states is decreased (or squeezed) by a factor of e^{2r}, while the variance of the phase quadrature is increased (or anti-squeezed) by the same factor. The squeezed states have a minimum uncertainty, however, the variance of the two quadratures are redistributed in the squeezed states.

The squeezed states for $\phi = 0$ can be written in terms of the number state as follows:

$$S(r)|0\rangle = \frac{1}{\sqrt{\cosh r}} \sum_{n=0}^{\infty} \frac{\sqrt{(2n)!}}{2^n n!} (\tanh r)^n |2n\rangle . \quad (4.36)$$

This indicates that only an even number of photons are present in the squeezed states. The squeezed states are generated from the pairs of correlated photons, which will be presented in Section 4.5.

4.4 Second order nonlinear process

The second order nonlinear process plays a key role in generating the squeezed vacuum states. In this section, the theory of the second order nonlinear process will be presented.

When an electric field E is applied to a nonlinear material, it induces a polarization P as follows:

$$P = \epsilon_0(\chi^{(1)} E + \chi^{(2)} E^2 + ...)$$
$$= P^{(1)} + P^{(2)} + ..., \quad (4.37)$$

where ϵ_0 is the free space permittivity and $\chi^{(n)}$ is the n-th order optical susceptibility of

the nonlinear material. In this thesis, only the second order nonlinear term is considered.

When the electric field can be written as $E = E_0 e^{-i\omega t} + \text{h.c.}$, the second order polarization in Equation (4.37) is

$$P^{(2)} = \epsilon_0 \chi^{(2)}(E_0^2 e^{-2i\omega t} + \text{h.c.}) + \epsilon_0 \chi^{(2)}(2E_0 E_0^*). \tag{4.38}$$

This equation indicates that the second harmonics of the input electric field and the DC field are generated. When the input electric field is composed of more than one frequency components, the second order nonlinear optical susceptibility leads to the sum and difference frequency generation of the input electric fields.

For the sum frequency generation, the field with a frequency $\omega_3 = \omega_1 + \omega_2$ is generated from the input fields with a frequency ω_1, ω_2, as shown in Figure 4.1.

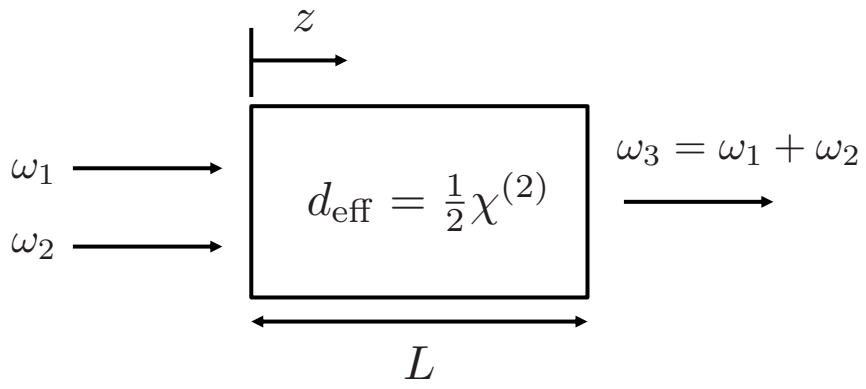

Figure 4.1: Schematic of sum frequency generation. A block in the center is a nonlinear material with effective nonlinear susceptibility $d_{\text{eff}} = \chi^{(2)}/2$. The optical axis is defined as the z axis and the length of the nonlinear material in the z axis is L. A field with a frequency $\omega_3 = \omega_1 + \omega_2$ is generated from the input fields with a frequency ω_1, ω_2.

The input and generated fields should satisfy the following wave equation [43]:

$$\nabla^2 \mathbf{E}_n - \frac{n^2(\omega_n)}{c^2} \frac{\partial^2 \mathbf{E}_n}{\partial t^2} = \frac{1}{\epsilon_0 c^2} \frac{\partial^2 \mathbf{P}_n^{\text{NL}}}{\partial t^2}, \tag{4.39}$$

where $\mathbf{E}_n$ is the n-th electric field, $n(\omega_n)$ is the refractive index of the nonlinear material for the n-th field, ω_n is the frequency of the n-th field, and $\mathbf{P}_n^{\text{NL}}$ is the nonlinear part of the polarization for the n-th field.

In the absence of a nonlinear source term, the solution of the wave equation (4.39) is

$$E_3(z,t) \quad = \quad A_3 e^{i(k_3 z - \omega_3 t)} + \text{h.c.}, \tag{4.40}$$

where A_3 is the constant amplitude of the generated field and

$$k_3 = \frac{n_3 \omega_3}{c}, \quad n_3 = n(\omega_3). \tag{4.41}$$

When the nonlinear source term is not large, we can assume that the solution to Equation (4.39) remains in the same form as Equation (4.40), except that A_3 becomes a slowly varying function of z. The nonlinear source term in Equation (4.39) can be written as follows:

$$P_3(z,t) \quad = \quad P_3 e^{-i\omega_3 t} + \text{h.c.}, \quad P_3 = 4\epsilon_0 d_{\text{eff}} E_1 E_2, \tag{4.42}$$

where $d_{\text{eff}} = \chi^{(2)}/2$.

Substituting Equation (4.40) and (4.42) into the wave equation (4.39),

$$\begin{aligned} &\left[\frac{d^2A_3}{dz^2} + 2ik_3\frac{dA_3}{dz} - k_3^2 A_3 + \frac{n_3^2\omega_3^2 A_3}{c^2}\right] e^{i(k_3 z - \omega_3 t)} + \text{h.c.} \\ &= -\frac{4d_{\text{eff}}\omega_3^2}{c^2} A_1 A_2 e^{i(k_1+k_2)z - \omega_3 t} + \text{h.c.}. \end{aligned} \tag{4.43}$$

As $k_3 = n_3\omega_3/c$, the third and fourth terms on the left hand side of Equation (4.43) are cancelled out. Assuming a slowly varying amplitude approximation,

$$\left|\frac{d^2A_3}{dz^2}\right| \ll \left|k_3\frac{dA_3}{dz}\right|. \tag{4.44}$$

Equation (4.43) is

$$\frac{dA_3}{dz} = \frac{2id_{\text{eff}}\omega_3^2}{k_3 c^2} A_1 A_2 e^{i\Delta k z}, \tag{4.45}$$

where $\Delta k = k_1 + k_2 - k_3$ is called the wavevector mismatch. In the simplified case where A_1, A_2 are constant,

$$A_3 = \frac{2id_{\text{eff}}\omega_3^2 A_1 A_2}{k_3 c^2}\int_0^L e^{i\Delta k z} dz = \frac{2id_{\text{eff}}\omega_3^2 A_1 A_2}{k_3 c^2}\frac{e^{i\Delta k L} - 1}{i\Delta k}. \tag{4.46}$$

The intensity of the generated field is calculated from the time averaged Poynting vector as follows:

$$I_3 = 2n_3\epsilon_0 c|A_3|^2. \tag{4.47}$$

Thus, we obtain

$$I_3 = \frac{8n_3\epsilon_0 d_{\text{eff}}^2\omega_3^4|A_1|^2|A_2|^2 L^2}{k_3^2 c^3}\text{sinc}^2\left(\frac{\Delta k L}{2}\right). \tag{4.48}$$

I_3 is characterized by the sinc function, which is shown in Figure 4.2. I_3 is maximum when the wavevector mismatch is $\Delta k = 0$.

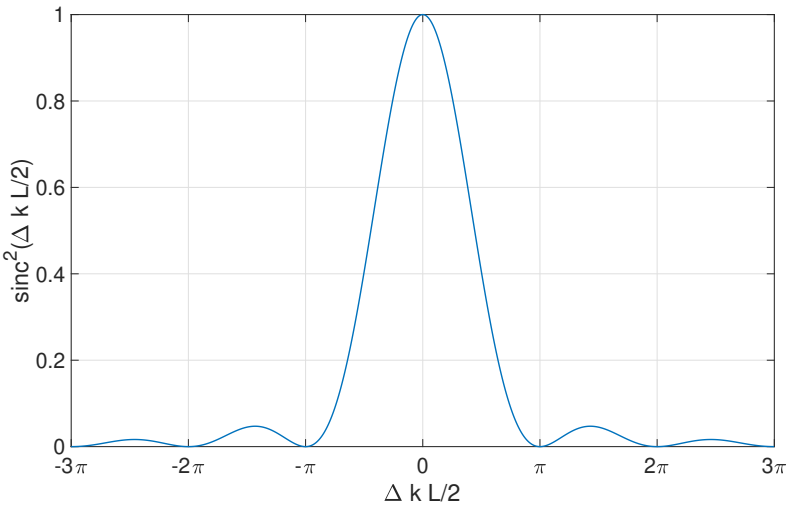

Figure 4.2: $\mathrm{sinc}^2(\Delta kL/2)$ as a function of the wavevector mismatch.

4.4.1 Phase matching

As we discussed in the previous section, the phase matching is important to maximize the nonlinear effect. The perfect phase matching condition $\Delta k = 0$ is

$$\frac{n_1\omega_1}{c} + \frac{n_2\omega_2}{c} = \frac{n_3\omega_3}{c}, \tag{4.49}$$

$$\omega_1 + \omega_2 = \omega_3. \tag{4.50}$$

This condition is typically difficult to achieve because the refractive index is an increasing function of the frequency in the normal dispersion. To achieve the phase matching condition, the following three different techniques are commonly used [43]. The first two techniques use the birefringence of the nonlinear material, while the third one can be used for the non-birefringence material.

Type I phase matching

In type I phase matching, the input fields have the same polarization, while the generated field has the orthogonal polarization with respect to the input fields. Phase matching can be done when the refractive indices of the nonlinear crystal for the two orthogonal polarizations have different values. Fine tuning of the refractive index of the crystal for the input and generated fields can be done by changing the incident angle of the input fields and the temperature of the crystal.

The second harmonic generator (SHG) in our experiment uses $MgO : LiNbO_3$ as a nonlinear crystal. As the refractive index of $MgO : LiNbO_3$ for the IR ordinary ray is approximately the same as that for the green extraordinary ray: $n_o(1064\text{ nm}) \simeq n_e(532\text{ nm}) \simeq 2.23$ [44], phase matching can be done via Type I phase matching.

Type II phase matching

In type II phase matching, the input fields have orthogonal polarizations, and the generated field has the same polarization as either of the injected fields.

Quasi phase matching

Instead of using the birefringence of the crystal, the quasi-phase matching flips the sign of the nonlinearity of the crystal before the phase mismatch between the input and generated fields becomes $\pi/2$. The quasi-phase matching can be done by inverting the crystal's domain periodically with a short length scale. A phase mismatch in the quasi-phase matching can be written as follows:

$$\Delta k_{\mathrm{QPM}} = k_1 + k_2 - k_3 - \frac{2\pi}{\Lambda}, \tag{4.51}$$

where Λ is the crystal inversion period. With quasi-phase matching, d_{eff} is replaced with $d_{\mathrm{QPM}} = \frac{2}{\pi} d_{\mathrm{eff}}$. Fine tuning of the phase matching condition can be done by tuning the refractive index of the crystal with the crystal temperature.

The optical parametric oscillator (OPO) in our experiment uses periodically oled potassium titanyl phosphate (PPKTP) as a nonlinear crystal, and phase matching is done via quasi-phase matching.

4.5 Generation of squeezed vacuum states

Squeezed vacuum states can be generated from OPO, which is an optical cavity and has a nonlinear crystal inside. OPO converts the pump photon, whose frequency is $2\omega_0$, to two correlated photons whose frequency is ω_0. In this section, the principle of the generation of squeezed vacuum states with OPO is presented.

4.5.1 Equation of motion of OPO with losses

In this section, the calculation of the equation of motion of OPO with losses is presented based on [45, 46, 47]. The OPO with losses can be modelled, as shown in Figure 4.3. It is a triangular cavity with the input, output, and loss couplers. We denote the coupler $j = i, o, l$ for the input, output, and loss couplers, respectively.

The Hamiltonian of the OPO with loss can be written as [48]

$$H = H_{\mathrm{cav}} + H_{\mathrm{int}} + H_{\mathrm{bath}}, \tag{4.52}$$

where H_{cav} is the Hamiltonian for the cavity modes, H_{int} is the Hamiltonian for the interaction between the cavity modes and the external modes that couple through coupler j, and H_{bath} is the Hamiltonian for the external modes,

$$H_{\mathrm{cav}} = \hbar\omega_0 a^\dagger a + \hbar(2\omega_0) b^\dagger b + \frac{i\hbar}{2}(\epsilon a^{\dagger 2} b - \epsilon^* a^2 b^\dagger), \tag{4.53}$$

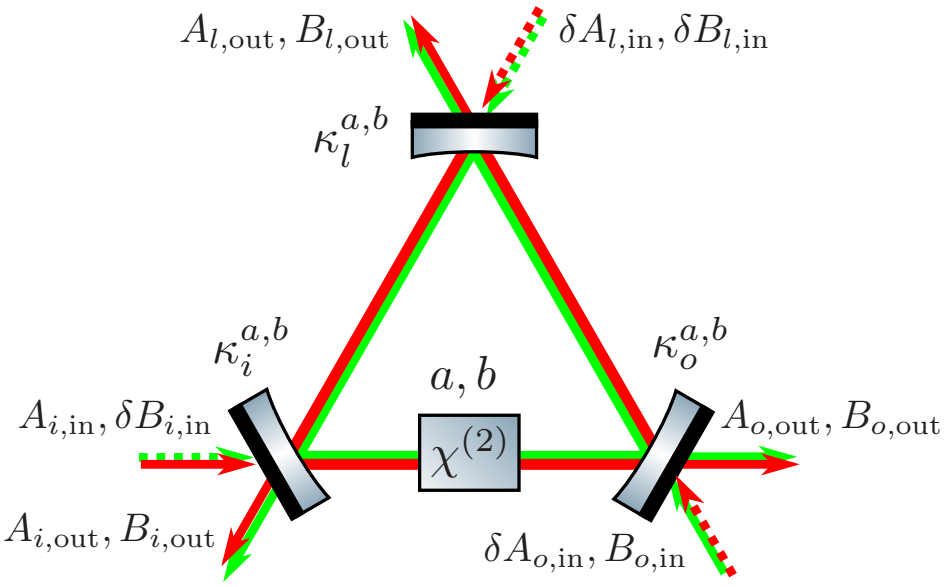

Figure 4.3: Model of OPO. a and b are the intracavity fields at the fundamental and second harmonic modes. $\kappa_i^{a,b}, \kappa_o^{a,b}$, and $\kappa_l^{a,b}$ are the decay rates for the input, output, and loss couplers for the fundamental and second harmonic modes. $A_{i,\mathrm{in}}$ and $\delta B_{i,\mathrm{in}}$, $\delta A_{o,\mathrm{in}}$ and $B_{o,\mathrm{in}}$, and $\delta A_{l,\mathrm{in}}$ and $\delta B_{l,\mathrm{in}}$ are the fundamental and second harmonic fields entering the cavity via the input, output, and loss couplers, respectively. $A_{i,\mathrm{out}}$ and $B_{i,\mathrm{out}}$, $A_{o,\mathrm{out}}$ and $B_{o,\mathrm{out}}$, and $A_{l,\mathrm{out}}$ and $B_{o,\mathrm{out}}$ are the fundamental and second harmonic fields exiting the cavity from the input, output, and loss couplers.

$$H_{\mathrm{int}} = i\hbar \sum_j \int_{-\infty}^{\infty} \left[\sqrt{2\kappa_j^a}(A_j^\dagger a - a^\dagger A_j) + \sqrt{2\kappa_j^b}(B_j^\dagger b - b^\dagger B_j) \right] d\omega, \tag{4.54}$$

$$H_{\mathrm{bath}} = \sum_j \int_{-\infty}^{\infty} \hbar\omega (A_j^\dagger A_j + B_j^\dagger B_j) d\omega, \tag{4.55}$$

where ϵ is the nonlinear coupling parameter and assumed to be a real number (optimal phase matching). a and b are the intracavity fields for the fundamental and second harmonic modes, respectively. A_j and B_j are the external fields coupling to the coupler j for the fundamental and second harmonic modes, respectively. $\kappa_j^{a,b} = (1 - \sqrt{R_j^{a,b}})/\tau_{\mathrm{rt}}$ is the decay rate of the coupler j for the fundamental and second harmonic modes, where $R_j^{a,b}$ is the power reflectivity of the coupler j for the fundamental and second harmonic mode and $\tau_{\mathrm{rt}} = L/c$ is the cavity round-trip time. The total cavity decay rate $\kappa^{a,b} = \sum_j \kappa_j^{a,b}$ corresponds to the cavity pole $2\pi f_p^{a,b}$ when the total cavity losses are low.

Assuming that the fundamental coherent field is injected from the input coupler, and second harmonic coherent field is injected from the output coupler which is the case for our experiment, the Langevin equation for the fundamental and second harmonic modes

will be [45]

$$\dot{a} = \frac{1}{i\hbar}[a, H_{\text{cav}}] - \kappa^a a + \sqrt{2\kappa_i^a} A_{i,\text{in}} e^{i\omega_0 t} + \sqrt{2\kappa_o^a}\delta A_{o,\text{in}} + \sqrt{2\kappa_l^a}\delta A_{l,\text{in}}, \quad (4.56)$$

$$\dot{b} = \frac{1}{i\hbar}[b, H_{\text{cav}}] - \kappa^b b + \sqrt{2\kappa_i^b}\delta B_{i,\text{in}} + \sqrt{2\kappa_o^b} B_{o,\text{in}} e^{i2\omega_0 t} + \sqrt{2\kappa_l^b}\delta B_{l,\text{in}}, \quad (4.57)$$

where $A_{j,\text{in}}$ and $B_{j,\text{in}}$ are the input external fields from the coupler j for the fundamental and second harmonic modes.

In a reference frame co-rotating with the injection coherent field,

$$\dot{a} = \epsilon a^\dagger b - (\kappa^a - i\Delta^a)a + \sqrt{2\kappa_i^a} A_{i,\text{in}} + \sqrt{2\kappa_o^a}\delta A_{o,\text{in}} + \sqrt{2\kappa_l^a}\delta A_{l,\text{in}}, \quad (4.58)$$

$$\dot{b} = -\frac{\epsilon}{2}a^2 - (\kappa^b - i\Delta^b)b + \sqrt{2\kappa_i^b}\delta B_{i,\text{in}} + \sqrt{2\kappa_o^b} B_{o,\text{in}} + \sqrt{2\kappa_l^b}\delta B_{l,\text{in}}, \quad (4.59)$$

where $\Delta^a = \omega_0 - \omega_{\text{cav}}^a, \Delta^b = 2\omega_0 - \omega_{\text{cav}}^b$ are the detuning of the injection frequency with respect to the cavity resonance.

We assume that the cavity operates on the resonance ($\Delta^{a,b} = 0$), constant pump ($\dot{b} = 0$), and photon number at the fundamental frequency is small ($a^2 = 0$). In this assumption,

$$\dot{a} = \epsilon b a^\dagger - \kappa^a a + \sqrt{2\kappa_i^a} A_{i,\text{in}} + \sqrt{2\kappa_o^a}\delta A_{o,\text{in}} + \sqrt{2\kappa_l^a}\delta A_{l,\text{in}}, \quad (4.60)$$

$$0 = -\kappa^b b + \sqrt{2\kappa_i^b}\delta B_{i,\text{in}} + \sqrt{2\kappa_o^b} B_{o,\text{in}} + \sqrt{2\kappa_l^b}\delta B_{l,\text{in}}. \quad (4.61)$$

Classical calculation

First, we calculate Equation (4.60) classically. Ignoring the quantum fluctuation terms and considering the steady state $\dot{a} = 0$, Equation (4.60) is

$$0 = |\epsilon||b| e^{i\phi_{\text{pump}}} a^\dagger - \kappa^a a + \sqrt{2\kappa_i^a} A_{i,\text{in}}, \quad (4.62)$$

$$0 = |\epsilon||b| e^{-i\phi_{\text{pump}}} a - \kappa^a a^\dagger + \sqrt{2\kappa_i^a} A_{i,\text{in}}^\dagger, \quad (4.63)$$

where ϕ_{pump} is the phase of the pump field. The $a^\dagger$ term in Equation (4.62) represents the sideband generated by the nonlinear effect. From Equation (4.62), (4.63) and setting the input field is real ($A_{i,\text{in}} = A_{i,\text{in}}^\dagger$),

$$a = \frac{\sqrt{2\kappa_i^a}}{\kappa^a} \frac{1 + x e^{i\phi_{\text{pump}}}}{1 - x^2} A_{i,\text{in}}, \quad (4.64)$$

where $x = |\epsilon||b|/\kappa^a$ is the OPO nonlinear factor. The OPO nonlinear factor is the ratio of the round-trip gain to the round-trip loss inside the OPO for the fundamental field. When it is above 1, the fundamental intracavity field becomes infinity, and the OPO can produce the fundamental coherent field. For the squeezing measurement, the OPO is

operated below the threshold. The OPO threshold power $P_{\rm th}$ can be written as follows:

$$x = \sqrt{\frac{P_{\rm pump}}{P_{\rm th}}}, \tag{4.65}$$

where $P_{\rm pump}$ is the injection pump power.

The parametric gain is the ratio of the transmission power (or intracavity power) of the fundamental field with/without the pump, which can be obtained from Equation (4.64):

$$G(\phi_{\rm pump}) = \frac{1 + x^2 + 2x\cos\phi_{\rm pump}}{(1-x^2)^2}. \tag{4.66}$$

The injected fundamental field is amplified or de-amplified, depending on the pump phase. In particular, the amplification factor

$$G(\phi_{\rm pump} = 0) = \frac{1}{(1-x)^2} = g \tag{4.67}$$

is called the nonlinear gain.

Quantum calculation

From Equation (4.60), when there is no coherent field at the fundamental frequency,

$$\delta\dot{a} = |\epsilon||b|e^{i\phi_{\rm pump}}\delta a^\dagger - \kappa^a\delta a + \sum_j \sqrt{2\kappa_j^a}\delta A_{j,\rm in}, \tag{4.68}$$

$$\delta\dot{a}^\dagger = |\epsilon||b|e^{-i\phi_{\rm pump}}\delta a - \kappa^a\delta a^\dagger + \sum_j \sqrt{2\kappa_j^a}\delta A_{j,\rm in}^\dagger. \tag{4.69}$$

From these equations, we can calculate the amplitude and phase quadrature $X_1^a = \frac{a+a^\dagger}{\sqrt{2}}$ and $X_2^a = \frac{a-a^\dagger}{\sqrt{2}i}$,

$$\delta\dot{X}_1^a = (-\kappa^a + |\epsilon||b|\cos\phi_{\rm pump})\delta X_1^a + |\epsilon||b|\sin\phi_{\rm pump}\delta X_2^a + \sum_j \sqrt{2\kappa_j^a}\delta X_1^{A_{j,\rm in}}, \tag{4.70}$$

$$\delta\dot{X}_2^a = (-\kappa^a - |\epsilon||b|\cos\phi_{\rm pump})\delta X_2^a + |\epsilon||b|\sin\phi_{\rm pump}\delta X_1^a + \sum_j \sqrt{2\kappa_j^a}\delta X_2^{A_{j,\rm in}}. \tag{4.71}$$

Obtaining the Fourier transform,

$$(1 - x\cos\phi_{\rm pump} + i\Omega/\kappa^a)\delta\tilde{X}_1^a - x\sin\phi_{\rm pump}\delta\tilde{X}_2^a = \sum_j \frac{\sqrt{2\kappa_j^a}}{\kappa^a}\delta\tilde{X}_1^{A_{j,\rm in}}, \tag{4.72}$$

$$(1 + x\cos\phi_{\rm pump} + i\Omega/\kappa^a)\delta\tilde{X}_2^a - x\sin\phi_{\rm pump}\delta\tilde{X}_1^a = \sum_j \frac{\sqrt{2\kappa_j^a}}{\kappa^a}\delta\tilde{X}_2^{A_{j,\rm in}}. \tag{4.73}$$

From Equation (4.72) and (4.73),

$$\begin{pmatrix} \delta\tilde{X}_1^a \\ \delta\tilde{X}_2^a \end{pmatrix} = \frac{1}{(1+x+i\Omega/\kappa^a)(1-x+i\Omega/\kappa^a)} \times \begin{pmatrix} 1+x\cos\phi_{\text{pump}}+i\Omega/\kappa^a & x\sin\phi_{\text{pump}} \\ x\sin\phi_{\text{pump}} & 1-x\cos\phi_{\text{pump}}+i\Omega/\kappa^a \end{pmatrix} \begin{pmatrix} \sum_j \frac{\sqrt{2\kappa_j^a}}{\kappa^a}\delta\tilde{X}_1^{A_{j,\text{in}}} \\ \sum_j \frac{\sqrt{2\kappa_j^a}}{\kappa^a}\delta\tilde{X}_2^{A_{j,\text{in}}} \end{pmatrix}. \tag{4.74}$$

The boundary condition for the output coupler is [45]

$$A_{o,\text{in}} + A_{o,\text{out}} = \sqrt{2\kappa_o^a}a. \tag{4.75}$$

Converting this to the two-photon formalism and obtaining the Fourier transform,

$$\delta\tilde{X}_{1,2}^{A_{o,\text{out}}} = \sqrt{2\kappa_o^a}\delta\tilde{X}_{1,2}^a - \delta\tilde{X}_{1,2}^{A_{o,\text{in}}}. \tag{4.76}$$

The variance of the amplitude and phase quadrature for the transmission field can be calculated as $V_{1,2}^{\text{trans}} = \langle 0|\,|\delta\tilde{X}_{1,2}^{A_{o,\text{out}}}|^2\,|0\rangle$. Using $\langle 0|\,\delta\tilde{X}_n^i\delta\tilde{X}_m^{\dagger j}\,|0\rangle = \delta_{ij}\delta_{nm}$, where $i,j = A_{i,\text{in}}, A_{o,\text{in}}, A_{l,\text{in}}$ and $n,m = 1,2$, the variance of the amplitude and phase quadrature for the OPO transmission are

$$\begin{pmatrix} V_1^{\text{trans}} \\ V_2^{\text{trans}} \end{pmatrix} = \begin{pmatrix} 1+4x\eta_{\text{esc}}\dfrac{2x+(1+x^2+(\Omega/\kappa^a)^2)\cos\phi_{\text{pump}}}{((1-x)^2+(\Omega/\kappa^a)^2)((1+x)^2+(\Omega/\kappa^a)^2)} \\ 1+4x\eta_{\text{esc}}\dfrac{2x-(1+x^2+(\Omega/\kappa^a)^2)\cos\phi_{\text{pump}}}{((1-x)^2+(\Omega/\kappa^a)^2)((1+x)^2+(\Omega/\kappa^a)^2)} \end{pmatrix}, \tag{4.77}$$

where $\eta_{\text{esc}} = \kappa_o^a/\kappa^a$ is called the OPO escape efficiency. $V_{1,2}^{\text{trans}}$ can be written in terms of $V_\pm$ as follows:

$$\begin{pmatrix} V_1^{\text{trans}} \\ V_2^{\text{trans}} \end{pmatrix} = \begin{pmatrix} \cos^2\frac{\phi_{\text{pump}}}{2} & \sin^2\frac{\phi_{\text{pump}}}{2} \\ \sin^2\frac{\phi_{\text{pump}}}{2} & \cos^2\frac{\phi_{\text{pump}}}{2} \end{pmatrix} \begin{pmatrix} V_+ \\ V_- \end{pmatrix}, \tag{4.78}$$

where

$$V_+ = 1+\eta_{\text{esc}}\frac{4x}{(1-x)^2+(\Omega/\kappa^a)^2}, \tag{4.79}$$

$$V_- = 1-\eta_{\text{esc}}\frac{4x}{(1+x)^2+(\Omega/\kappa^a)^2}. \tag{4.80}$$

V_+ corresponds to the anti-squeezing quadrature and V_- corresponds to the squeezing quadrature.

When $\Omega/\kappa^a \ll 1$, the variances of the squeezing and anti-squeezing quadrature $V_\pm$ are

$$V_\pm = 1 \pm 4\eta_{\text{esc}}\frac{x}{(1\mp x)^2}. \tag{4.81}$$

From Equation (4.81), the nonlinear gain g is related to the generated squeezing level σ_{dB} without losses ($\eta_{\mathrm{esc}} = 1$) as follows:

$$\sigma_{\mathrm{dB}} = -10 \log_{10} V_{-} = -20 \log_{10} \frac{1-x}{1+x} = 20 \log_{10} (2\sqrt{g} - 1). \tag{4.82}$$

4.6 Balanced homodyne detection

To measure the squeezed vacuum states, balanced homodyne detection is widely used, as shown in Figure 4.4. The local oscillator and the squeezed vacuum states are combined with the beam splitter, and the two outputs from the beam splitter are detected with photo detectors, and the difference of the two outputs is extracted.

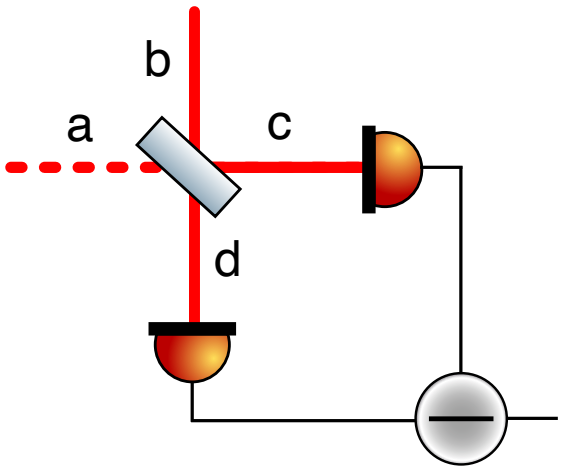

Figure 4.4: Configuration of balanced homodyne detection. a, b are input fields for BS and c, d are output fields for BS. The output fields from BS are detected with photo detectors and then subtracted.

The input-output relation of the beam splitter is

$$\begin{pmatrix} c \\ d \end{pmatrix} = \frac{1}{\sqrt{2}} \begin{pmatrix} 1 & 1 \\ 1 & -1 \end{pmatrix} \begin{pmatrix} a \\ b \end{pmatrix}. \tag{4.83}$$

The photocurrent at each PD is

$$I_c \propto c^\dagger c = \frac{1}{2}(a^\dagger a + a^\dagger b + b^\dagger a + b^\dagger b), \tag{4.84}$$

$$I_d \propto d^\dagger d = \frac{1}{2}(a^\dagger a - a^\dagger b - b^\dagger a + b^\dagger b). \tag{4.85}$$

When the two signals are balanced, the difference of these signals is

$$I_{\mathrm{diff}} = I_c - I_d \propto a^\dagger b + b^\dagger a. \tag{4.86}$$

When a is the squeezed vacuum filed and b is the local oscillator (LO),

$$a = \delta a e^{i\phi_{\mathrm{CC}}},\ b = (\bar{b} + \delta b)e^{i\phi_{\mathrm{LO}}}, \tag{4.87}$$

where $\bar{b}$ is the DC amplitude of the LO and δa and δb are fluctuation terms. ϕ_{CC} and ϕ_{LO} are the phase of the squeezed vacuum field and LO, respectively. ϕ_{CC} can be tracked by the coherent control (CC) field, which is presented in the next section.

Ignoring the second order of the fluctuation terms, Equation (4.86) is

$$\begin{aligned} I_{\mathrm{diff}} &\propto \bar{b}(\delta a^{\dagger} e^{i(\phi_{\mathrm{LO}}-\phi_{\mathrm{CC}})} + \delta a e^{-i(\phi_{\mathrm{LO}}-\phi_{\mathrm{CC}})}) \\ &= \sqrt{2}\bar{b}(\delta X_1 \cos(\phi_{\mathrm{LO}} - \phi_{\mathrm{CC}}) + \delta X_2 \sin(\phi_{\mathrm{LO}} - \phi_{\mathrm{CC}})). \end{aligned} \tag{4.88}$$

Normalizing the equation above by the LO power, the variance of the squeezed vacuum field measured by the homodyne detector is

$$V_{\mathrm{meas}} = \cos^2(\phi_{\mathrm{LO}} - \phi_{\mathrm{CC}})V_1 + \sin^2(\phi_{\mathrm{LO}} - \phi_{\mathrm{CC}})V_2. \tag{4.89}$$

From Equation (4.78), the amplitude quadrature δX_1 is rotated from the anti-squeezing quadrature δX_+ by $\phi_{\mathrm{pump}}/2$. Therefore, we can express the measured quadrature as follows:

$$\delta X_{\mathrm{meas}} = \begin{pmatrix} \cos(\phi_{\mathrm{LO}} - \phi_{\mathrm{CC}}) & \sin(\phi_{\mathrm{LO}} - \phi_{\mathrm{CC}}) \end{pmatrix} \begin{pmatrix} \cos\frac{\phi_{\mathrm{pump}}}{2} & -\sin\frac{\phi_{\mathrm{pump}}}{2} \\ \sin\frac{\phi_{\mathrm{pump}}}{2} & \cos\frac{\phi_{\mathrm{pump}}}{2} \end{pmatrix} \begin{pmatrix} \delta X_+ \\ \delta X_- \end{pmatrix}. \tag{4.90}$$

The variance of the measured quadrature is

$$V_{\mathrm{meas}} = \cos^2(\phi_{\mathrm{sqz}})V_+ + \sin^2(\phi_{\mathrm{sqz}})V_-, \tag{4.91}$$

where

$$\phi_{\mathrm{sqz}} = \phi_{\mathrm{LO}} - \phi_{\mathrm{CC}} - \frac{\phi_{\mathrm{pump}}}{2} \tag{4.92}$$

is called the squeezing angle. $\phi_{\mathrm{sqz}} = 0$ corresponds to the anti-squeezing quadrature and $\phi_{\mathrm{sqz}} = \pi/2$ corresponds to the squeezing quadrature. In this thesis, we define the homodyne angle as $\phi_{\mathrm{hom}} = \pi/2 - \phi_{\mathrm{sqz}}$. By changing the squeezing angle ϕ_{sqz}, any quadrature of the squeezed vacuum filed can be measured. When we want to maintain the same quadrature, ϕ_{sqz} has to be controlled.

4.7 Coherent control

Coherent control is a technique used to control the squeezing angle [49]. The coherent control field, whose frequency is $\omega_0 + \Omega_{\mathrm{cc}}$, is injected to the OPO and copropagates with

the squeezed vacuum field. The coherent control field can track the phase of the squeezed vacuum field. The coherent control is composed of two coherent control loops (referred to as CC1 and CC2 in this thesis). ϕ_{pump} is maintained constant by CC1, and the relative phase between LO and CC ($\phi_{\mathrm{LO}} - \phi_{\mathrm{CC}}$) is maintained constant by CC2 to make the squeezing angle ϕ_{sqz} constant.

For simplicity, we assume that detuning of the CC field inside the OPO is significantly smaller than the OPO bandwidth $\Omega_{\mathrm{cc}} \ll \kappa^a$. When the CC field is injected from the input port of the OPO, as shown in Figure 4.3, the CC field inside the OPO is from Equation (4.62) and (4.63),

$$a_{\mathrm{cav,cc}} = \frac{\sqrt{2\kappa_i^a} A_{\mathrm{cc}}}{(1-x^2)\kappa^a} \left(e^{i(\omega_0+\Omega_{\mathrm{cc}})t} + x e^{i(\omega_0-\Omega_{\mathrm{cc}})t+i\phi_{\mathrm{pump}}} \right), \tag{4.93}$$

where A_{cc} is the amplitude of the CC field before the OPO. In this formula, the reference frame is not co-rotating with $e^{i\omega_0 t}$. Owing to the nonlinear effect of the OPO, an additional sideband with a frequency of $\omega_0 - \Omega_{\mathrm{cc}}$ and phase of ϕ_{pump} is generated.

CC1 error signal

The CC1 error signal is obtained by detecting the beat note of the two CC sidebands (CCSB) at the OPO reflection. The reflected CCSB fields from the OPO can be calculated from the boundary condition of the input port as follows:

$$\begin{aligned} A_{\mathrm{refl,cc}} &= \sqrt{2\kappa_i^a} a_{\mathrm{cav,cc}} - A_{\mathrm{in,cc}} \\ &= \left\{ \frac{2\kappa_i^a}{(1-x^2)\kappa^a} - 1 \right\} A_{\mathrm{cc}} e^{i(\omega_0+\Omega_{\mathrm{cc}})t} + \frac{2\kappa_i^a A_{\mathrm{cc}} x}{(1-x^2)\kappa^a} e^{i(\omega_0-\Omega_{\mathrm{cc}})t+i\phi_{\mathrm{pump}}}. \end{aligned} \tag{4.94}$$

The beat note of the CCSB at the OPO reflection is

$$P_{\mathrm{CC1}} = \frac{4A_{\mathrm{cc}}^2 \kappa_i^a x}{(1-x^2)\kappa^a} \left\{ \frac{2\kappa_i^a}{(1-x^2)\kappa^a} - 1 \right\} \cos\left(2\Omega_{\mathrm{cc}} t - \phi_{\mathrm{pump}}\right). \tag{4.95}$$

Demodulating this signal with $\cos\left(2\Omega_{\mathrm{cc}} + \phi_{\mathrm{dm,CC1}}\right)$ and low-passing it, the CC1 error signal is

$$P_{\mathrm{CC1}} = \frac{2A_{\mathrm{cc}}^2 \kappa_i^a x}{(1-x^2)\kappa^a} \left\{ \frac{2\kappa_i^a}{(1-x^2)\kappa^a} - 1 \right\} \cos\left(\phi_{\mathrm{pump}} + \phi_{\mathrm{dm,CC1}}\right). \tag{4.96}$$

As the CC1 error signal is locked at the point where the CC1 error signal (4.96) is 0,

$$\phi_{\mathrm{pump}} = -\phi_{\mathrm{dm,CC1}} + \frac{\pi}{2}. \tag{4.97}$$

ϕ_{pump} can be fixed to any value by changing the CC1 demodulation phase $\phi_{\mathrm{dm,CC1}}$.

CC2 error signal

The CC2 error signal is obtained from the beat note of CCSB and LO at the homodyne detector. The CCSB transmit the OPO and reach the homodyne detector with squeezed vacuum states. When the phase of the CCSB between the OPO and homodyne detector is ϕ_{CC}, the CCSB at the homodyne detector are

$$e^{i\phi_{\mathrm{CC}}}\sqrt{2\kappa_o^a}a_{\mathrm{cav,cc}} = \frac{2\sqrt{\kappa_i^a\kappa_o^a}A_{\mathrm{cc}}}{(1-x^2)\kappa^a}\left(e^{i(\omega_0+\Omega_{\mathrm{cc}})t+i\phi_{\mathrm{CC}}} + xe^{i(\omega_0-\Omega_{\mathrm{cc}})t+i(\phi_{\mathrm{CC}}+\phi_{\mathrm{pump}})}\right). \quad (4.98)$$

From Equation (4.86), the beat signal of CCSB and LO ($A_{\mathrm{LO}}e^{i\omega_0 t+i\phi_{\mathrm{LO}}}$) at the homodyne detector is

$$\begin{aligned} P_{\mathrm{CC2}} &= \frac{4\sqrt{\kappa_i^a\kappa_o^a}A_{\mathrm{cc}}A_{\mathrm{LO}}}{(1-x^2)\kappa^a}\{\cos(\Omega_{\mathrm{cc}}t-\phi_{\mathrm{LO}}+\phi_{\mathrm{CC}})+x\cos(\Omega_{\mathrm{cc}}t+\phi_{\mathrm{LO}}-\phi_{\mathrm{CC}}-\phi_{\mathrm{pump}})\} \\ &= \frac{4\sqrt{\kappa_i^a\kappa_o^a}A_{\mathrm{cc}}A_{\mathrm{LO}}}{(1-x^2)\kappa^a}\{\cos(\Omega_{\mathrm{cc}}t-\phi_{\mathrm{sqz}}-\phi_{\mathrm{pump}}/2)+x\cos(\Omega_{\mathrm{cc}}t+\phi_{\mathrm{sqz}}-\phi_{\mathrm{pump}}/2)\}. \end{aligned} \quad (4.99)$$

Considering the cosine terms in Equation (4.99),

$$\begin{aligned} P_{\mathrm{CC2}} &\propto \cos(\Omega_{\mathrm{cc}}t-\phi_{\mathrm{sqz}}-\phi_{\mathrm{pump}}/2)+x\cos(\Omega_{\mathrm{cc}}t+\phi_{\mathrm{sqz}}-\phi_{\mathrm{pump}}/2) \\ &= \{\cos(\phi_{\mathrm{sqz}}+\phi_{\mathrm{pump}}/2)+x\cos(\phi_{\mathrm{sqz}}-\phi_{\mathrm{pump}}/2)\}\cos\Omega_{\mathrm{cc}}t \\ &+ \{\sin(\phi_{\mathrm{sqz}}+\phi_{\mathrm{pump}}/2)-x\sin(\phi_{\mathrm{sqz}}-\phi_{\mathrm{pump}}/2)\}\sin\Omega_{\mathrm{cc}}t \\ &= \sqrt{1+x^2+2x\cos(2\phi_{\mathrm{sqz}})}\cos(\Omega_{\mathrm{cc}}t+\phi_{\mathrm{CC2}}), \end{aligned} \quad (4.100)$$

where

$$\phi_{\mathrm{CC2}} = \arctan\left\{\frac{-\sin(\phi_{\mathrm{sqz}}+\phi_{\mathrm{pump}}/2)+x\sin(\phi_{\mathrm{sqz}}-\phi_{\mathrm{pump}}/2)}{\cos(\phi_{\mathrm{sqz}}+\phi_{\mathrm{pump}}/2)+x\cos(\phi_{\mathrm{sqz}}-\phi_{\mathrm{pump}}/2)}\right\}. \quad (4.101)$$

Demodulating Equation (4.100) by $\cos(\Omega_{\mathrm{cc}}t+\phi_{\mathrm{dm,CC2}})$ and low-passing it, the CC2 error signal is

$$P_{\mathrm{CC2}} = \frac{2\sqrt{\kappa_i^a\kappa_o^a}A_{\mathrm{cc}}A_{\mathrm{LO}}}{\kappa^a}\frac{\sqrt{1+x^2+2x\cos(2\phi_{\mathrm{sqz}})}}{1-x^2}\cos(\phi_{\mathrm{CC2}}-\phi_{\mathrm{dm,CC2}}). \quad (4.102)$$

As the CC2 error signal is locked at the point where the CC2 error signal (4.102) is 0,

$$\phi_{\mathrm{dm,CC2}} = \phi_{\mathrm{CC2}}+\frac{\pi}{2}. \quad (4.103)$$

The squeezing angle ϕ_{sqz}, which is included in ϕ_{CC2}, can be fixed to any value by changing the CC2 demodulation phase $\phi_{\mathrm{dm,CC2}}$.

CC2 demodulation phase and squeezing angle

The relationship between the squeezing angle and the CC2 demodulation phase is linear without a nonlinear effect ($x = 0$), however, it becomes nonlinear with a nonlinear effect of CCSB. The relationship between the CC2 demodulation phase and the squeezing angle (4.103) with $\phi_{\mathrm{pump}} = 0$ is shown in Figure 4.5. The squeezing angle becomes sensitive to the CC2 demodulation phase around the anti-squeezing quadrature ($\phi_{\mathrm{sqz}} = 0, \pi$) owing to the nonlinear effect of CCSB.

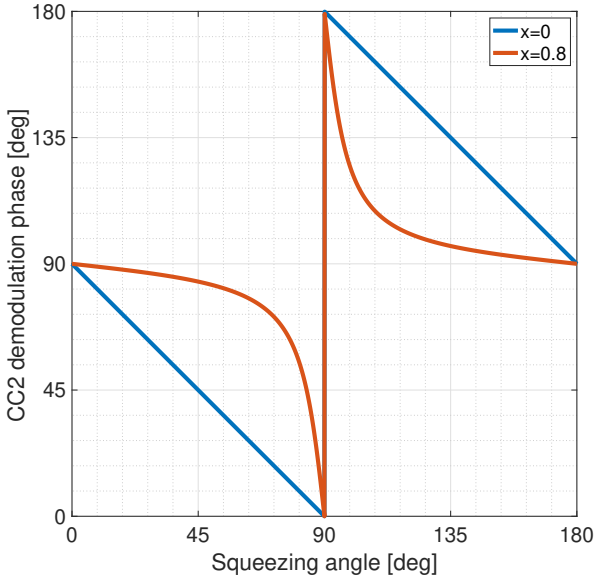

Figure 4.5: Relation between the CC2 demodulation phase and squeezing angle with $\phi_{\mathrm{pump}} = 0$ for $x = 0$ and 0.8.

4.8 Squeezing degradation sources

In the experiment, there are several sources which degrade the achievable squeezing level. In this section, the main squeezing degradation sources, including losses, classical noise, and phase noise, are presented.

4.8.1 Losses

When there are losses in the squeezing path, the squeezed vacuum field is lost, and the external vacuum field comes in from the loss port, and the squeezing level is degraded. The squeezing and anti-squeezing levels with losses l are

$$V_{\pm}^{l} = (1 - l)V_{\pm} + l, \tag{4.104}$$

where $V_\pm$ are the squeezing and anti-squeezing levels without any losses,

$$V_\pm = 1 \pm 4\frac{x}{(1 \mp x)^2}. \tag{4.105}$$

From Equation (4.104) and (4.105), the squeezing and anti-squeezing noise levels with losses can be written as follows:

$$V_-^l = 1 - 4\eta\frac{x}{(1+x)^2}, \tag{4.106}$$

$$V_+^l = 1 + 4\eta\frac{x}{(1-x)^2}, \tag{4.107}$$

where $\eta = 1 - l$ is the total efficiency, which can be divided into $\eta = \eta_{\rm esc}\eta_{\rm loss}\eta_{\rm vis}\eta_{\rm PD}$ where $\eta_{\rm esc}$ is the escape efficiency of OPO, $\eta_{\rm loss}$ is the propagation efficiency, $\eta_{\rm vis}$ is the efficiency of the visibility of the LO and squeezed field, and $\eta_{\rm PD}$ is the efficiency of the photo detectors.

The squeezing and anti-squeezing levels as a function of losses are shown in Figure 4.6.

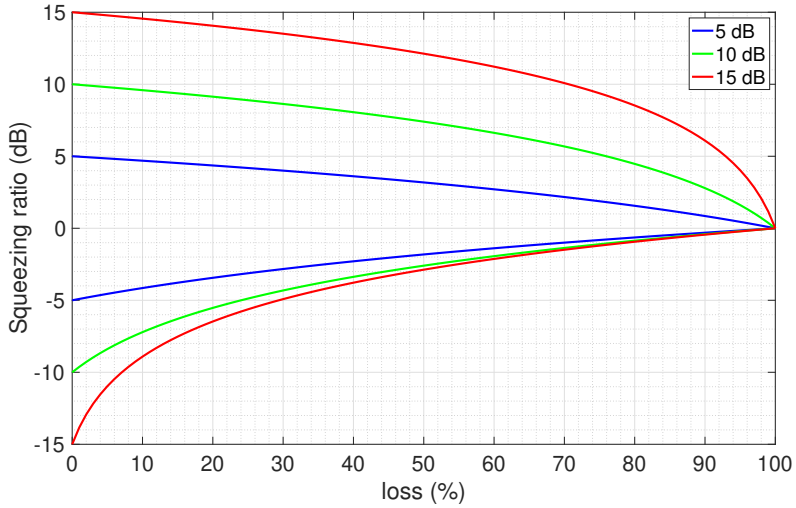

Figure 4.6: Squeezing and anti-squeezing levels as a function of losses for 5, 10, and 15 dB generated squeezing. The squeezing level is degraded more than the anti-squeezing level by losses.

4.8.2 Classical noise

As the classical noise in the detected signal, such as dark noise of the electronics, increases both vacuum noise (quantum noise without squeezing) and squeezing noise levels, the classical noise can be considered as an optical loss [50, 51]. The squeezing level with the

classical noise is

$$\begin{aligned} V_-^{\rm obs} &= \frac{V_{\rm sqz}^{\rm obs}}{V_{\rm vac}^{\rm obs}} \\ &= \frac{V_{\rm sqz}+V_{\rm class}}{V_{\rm vac}+V_{\rm class}} \\ &= \left(1-\frac{V_{\rm class}}{V_{\rm vac}+V_{\rm class}}\right)\frac{V_{\rm sqz}}{V_{\rm vac}}+\frac{V_{\rm class}}{V_{\rm vac}+V_{\rm class}} \\ &= \left(1-\frac{V_{\rm class}}{V_{\rm vac}^{\rm obs}}\right)V_- + \frac{V_{\rm class}}{V_{\rm vac}^{\rm obs}}, \end{aligned} \tag{4.108}$$

where $V_-^{\rm obs}, V_{\rm sqz}^{\rm obs}$ and $V_{\rm vac}^{\rm obs}$ are the observed squeezing ratio, observed squeezing noise level, and observed vacuum noise level, respectively. $V_{\rm class}$ is the classical noise level. This formula has the same form as Equation (4.104) and the effect of the classical noise is the same as the effect of the losses $l = V_{\rm class}/V_{\rm vac}^{\rm obs}$ (ratio of the classical noise and observed vacuum noise in the power spectral density).

4.8.3 Phase noise

The squeezing angle fluctuation (phase noise) couples the anti-squeezing quadrature to the squeezing quadrature and degrades the squeezing level. The squeezing and anti-squeezing levels with the phase noise are

$$V_\pm^\theta(t) = V_\pm \cos^2\theta(t) + V_\mp \sin^2\theta(t). \tag{4.109}$$

Although the squeezing angle can be controlled by the coherent control, there are residual fluctuations of the squeezing angle. If we model the fluctuations as normally distributed around $\theta = 0$ with a small rms fluctuation $\theta_{\rm rms}$ (< 100 mrad), we can write the averaged variance of the squeezing and anti-squeezing quadrature as follows:

$$\begin{aligned} V_\pm^{\theta_{\rm rms}} &= \int_{-\infty}^{\infty} d\theta \frac{e^{-\theta^2/2\theta_{\rm rms}^2}}{\sqrt{2\pi}\theta_{\rm rms}}(V_\pm\cos^2\theta + V_\mp\sin^2\theta) \\ &\simeq V_\pm\cos^2\theta_{\rm rms} + V_\mp\sin^2\theta_{\rm rms}. \end{aligned} \tag{4.110}$$

The squeezing and anti-squeezing levels as a function of the phase noise are shown in Figure 4.7.

4.8.4 Combination of squeezing degradation sources

From Equation (4.104) and (4.110), the squeezing and anti-squeezing levels with the loss and phase noise are

$$V_\pm^{l,\theta_{\rm rms}} = (1-l)(V_\pm\cos^2\theta_{\rm rms} + V_\mp\sin^2\theta_{\rm rms}) + l \tag{4.111}$$

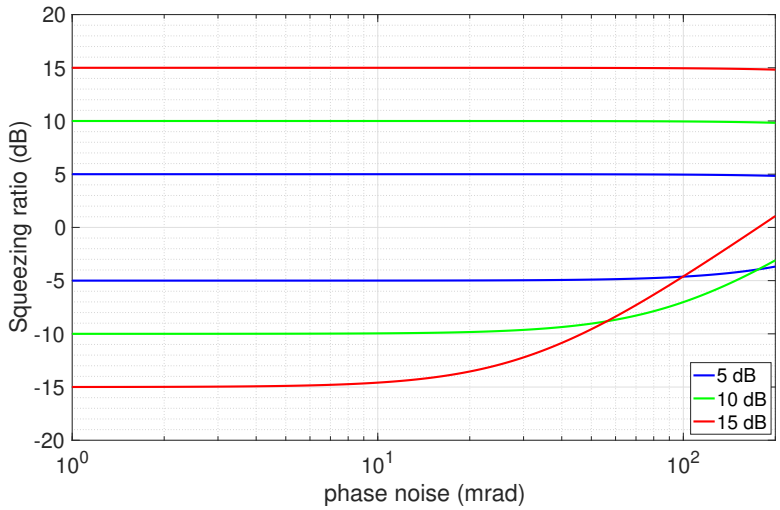

Figure 4.7: Squeezing and anti-squeezing level as a function of phase noise for 5, 10, and 15 dB generated squeezing. The squeezing level is degraded by the phase noise, while the anti-squeezing level nearly does not degrade.

From Equation (4.105) and (4.111), the squeezing level with the loss and phase noise can be written as a function of x as follows:

$$V_{-}^{l,\theta_{\rm rms}} = 1 + 4\eta x \left\{ \frac{\sin^2\theta_{\rm rms}}{(1-x)^2} - \frac{\cos^2\theta_{\rm rms}}{(1+x)^2} \right\}. \tag{4.112}$$

When the generated squeezing level is increased, the squeezing level is increased, but the anti-squeezing level is also increased, which decreases the squeezing level due to phase noise. Therefore, there is an optimal generated squeezing level for the maximum achievable squeezing level with loss and phase noise, which can be obtained by solving $dV_{-}^{l,\theta_{\rm rms}}/dx = 0$ where

$$\frac{dV_{-}^{l,\theta_{\rm rms}}}{dx} = -4\eta \frac{(1+6x^2+x^4)\cos 2\theta_{\rm rms} - 4x(1+x^2)}{(1-x^2)^3}. \tag{4.113}$$

The optimal value for x is obtained as follows [46]:

$$x = 1 - 2\sqrt{\theta_{\rm rms}} + 2\theta_{\rm rms} - 2\theta_{\rm rms}^{3/2} + 2\theta_{\rm rms}^2. \tag{4.114}$$

The optimal generated squeezing for a maximum achievable squeezing level depends on only phase noise.

Although the maximum achievable squeezing level with loss and phase can be obtained by substituting Equation (4.114) into Equation (4.112), it is easier to obtain it from Equation (4.111) without using x. From Equation (4.111) and $V_{+}V_{-} = 1$, the squeezing level with loss and phase noise can be written as a function of the anti-squeezing level as

follows:

$$V_{-}^{l,\theta_{\mathrm{rms}}} = \frac{1-l}{2}\left\{\left(\tan^2\theta_{\mathrm{rms}}+\frac{1}{\tan^2\theta_{\mathrm{rms}}}\right)\frac{V_{+}^{l,\theta_{\mathrm{rms}}}-l}{1-l} + \left(\tan\theta_{\mathrm{rms}}-\frac{1}{\tan\theta_{\mathrm{rms}}}\right)\sqrt{\left(\tan\theta_{\mathrm{rms}}+\frac{1}{\tan\theta_{\mathrm{rms}}}\right)^2\left(\frac{V_{+}^{l,\theta_{\mathrm{rms}}}-l}{1-l}\right)^2-4}\right\}+l, \tag{4.115}$$

where $\theta_{\mathrm{rms}} \ll 1$ is assumed. It is a general formula between the squeezing level and anti-squeezing levels with the loss and phase noise and is independent of the generated squeezing level. From Equation (4.115), the maximum achievable squeezing level for a given loss and phase noise can be obtained. By solving $dV_{-}^{l,\theta_{\mathrm{rms}}}/dV_{+}^{l,\theta_{\mathrm{rms}}} = 0$, the maximum achievable squeezing level and the corresponding anti-squeezing level are derived as follows:

$$V_{-}^{l,\theta_{\mathrm{rms}}} = \frac{2(1-l)}{\tan\theta_{\mathrm{rms}}+\frac{1}{\tan\theta_{\mathrm{rms}}}}+l, \tag{4.116}$$

$$V_{+}^{l,\theta_{\mathrm{rms}}} = (1-l)\frac{\tan^2\theta_{\mathrm{rms}}+\frac{1}{\tan^2\theta_{\mathrm{rms}}}}{\tan\theta_{\mathrm{rms}}+\frac{1}{\tan\theta_{\mathrm{rms}}}}+l. \tag{4.117}$$

The maximum achievable squeezing level (4.116) as a function of loss and phase noise is shown in Figure 4.8.

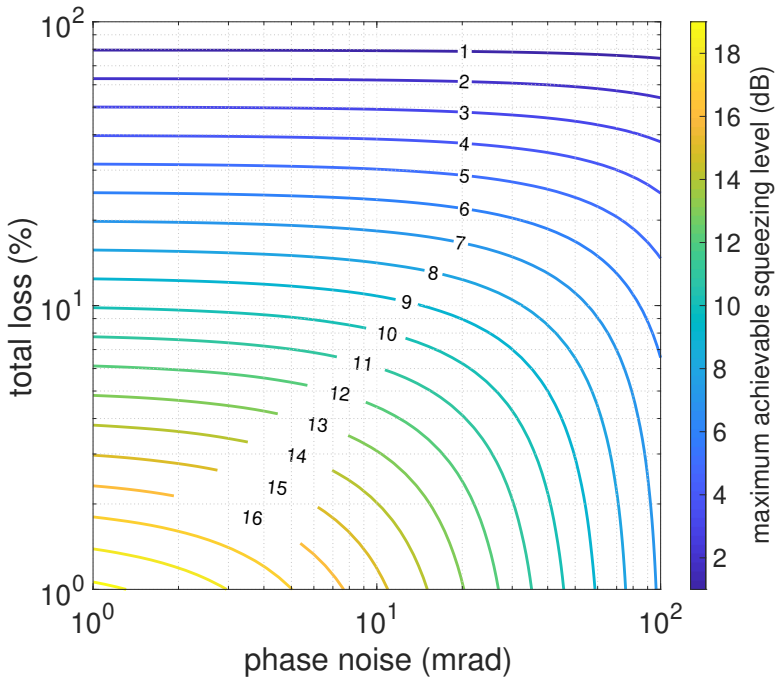

Figure 4.8: Maximum achievable squeezing level with losses and phase noise.

Chapter 5

Quantum Noise in Gravitational-Wave Detector

Quantum noise in GW detectors originates from the vacuum field entering the output port of the interferometer, as shown in Figure 5.1. Injecting the squeezed vacuum field instead of the vacuum field is a key for reducing the quantum noise. In this chapter, a basic summary of the quantum noise and how the squeezed vacuum field can improve the quantum noise are presented.

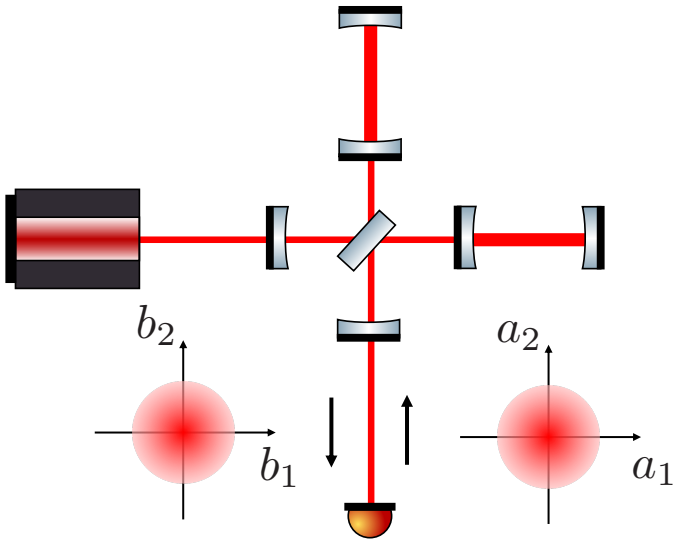

Figure 5.1: Injection of vacuum field in GW detectors.

5.1 Quantum noise

The relationship between the injected vacuum field a and the vacuum field reflected from the interferometer b is [14]

$$\begin{pmatrix} b_1 \\ b_2 \end{pmatrix} = e^{i2\beta} \begin{pmatrix} 1 & 0 \\ -\mathcal{K} & 1 \end{pmatrix} \begin{pmatrix} a_1 \\ a_2 \end{pmatrix} + e^{i\beta} \begin{pmatrix} 0 \\ \sqrt{2\mathcal{K}} \end{pmatrix} \frac{h}{2h_{\mathrm{SQL}}}, \tag{5.1}$$

where $\mathcal{K}$ is the optomechanical coupling factor of the interferometer, h is GW strain signal, h_{SQL} is the standard quantum limit, and β is the phase shift from the interferometer,

$$\mathcal{K} = \left(\frac{\Omega_{\mathrm{SQL}}}{\Omega}\right)^2 \frac{\gamma_{\mathrm{ifo}}^2}{\Omega^2 + \gamma_{\mathrm{ifo}}^2}, \tag{5.2}$$

$$h_{\mathrm{SQL}} = \sqrt{\frac{8\hbar}{m\Omega^2 L_{\mathrm{arm}}^2}}, \tag{5.3}$$

$$\beta = \arctan\left(\frac{\Omega}{\gamma_{\mathrm{ifo}}}\right), \tag{5.4}$$

where Ω_{SQL} is the approximate frequency at which the quantum noise reaches the standard quantum limit and γ_{ifo} is the interferometer bandwidth,

$$\Omega_{\mathrm{SQL}} = \frac{t_{\mathrm{sr}}}{1 + r_{\mathrm{sr}}} \frac{8}{c} \sqrt{\frac{P_{\mathrm{arm}}\omega_0}{mT_{\mathrm{arm}}}}, \tag{5.5}$$

$$\gamma_{\mathrm{ifo}} = \frac{1 + r_{\mathrm{sr}}}{1 - r_{\mathrm{sr}}} \frac{T_{\mathrm{arm}} c}{4L_{\mathrm{arm}}} = \frac{1 + r_{\mathrm{sr}}}{1 - r_{\mathrm{sr}}} \gamma_{\mathrm{arm}}. \tag{5.6}$$

Here, t_{sr} and r_{sr} are the amplitude transmissivity and reflectivity of the signal recycling mirror, respectively. P_{arm} is the arm intracavity power, m is the test mirror mass, L_{arm} is the arm cavity length, and ω_0 is the carrier frequency. These parameters in KAGRA are summarized in Table 5.1.

Table 5.1: KAGRA parameter

Parameter	Symbol	Value
Carrier field frequency	ω_0	$2\pi \times 283$ THz
Standard quantum limit frequency	Ω_{SQL}	$2\pi \times 76.4$ Hz
Interferometer bandwidth	γ_{ifo}	$2\pi \times 382$ Hz
Arm input mirror transmissivity	T_{arm}	0.004
Signal recycling input transmissivity	t_{sr}^2	0.1536
Arm intracavity power	P_{arm}	400 kW
Mirror mass	m	22.8 kg
Arm cavity length	L_{arm}	3 km

The GW signal is included in b_2 in Equation (5.1):

$$b_2 = e^{i2\beta}(a_2 - \mathcal{K}a_1) + e^{i\beta}\sqrt{2\mathcal{K}}\frac{h}{2h_{\mathrm{SQL}}}. \tag{5.7}$$

The first term is the quantum noise, and the second term is the GW signal. From this formula, the quantum noise in terms of the GW strain will be

$$h = \frac{h_{\mathrm{SQL}}}{\sqrt{2\mathcal{K}}} e^{i\beta}(a_2 - \mathcal{K}a_1). \tag{5.8}$$

The power spectral density of quantum noise in GW detectors can be written as follows:

$$S_h = \frac{h_{\mathrm{SQL}}^2}{2}\left(\frac{1}{\mathcal{K}} + \mathcal{K}\right) \geqq h_{\mathrm{SQL}}^2. \tag{5.9}$$

The first term is shot noise, and the second term is the radiation pressure noise. Quantum noise in terms of strain $\sqrt{S_h}$ is shown in Figure 5.2. Quantum noise is dominated by shot noise at high frequencies and dominated by radiation pressure noise at low frequencies.

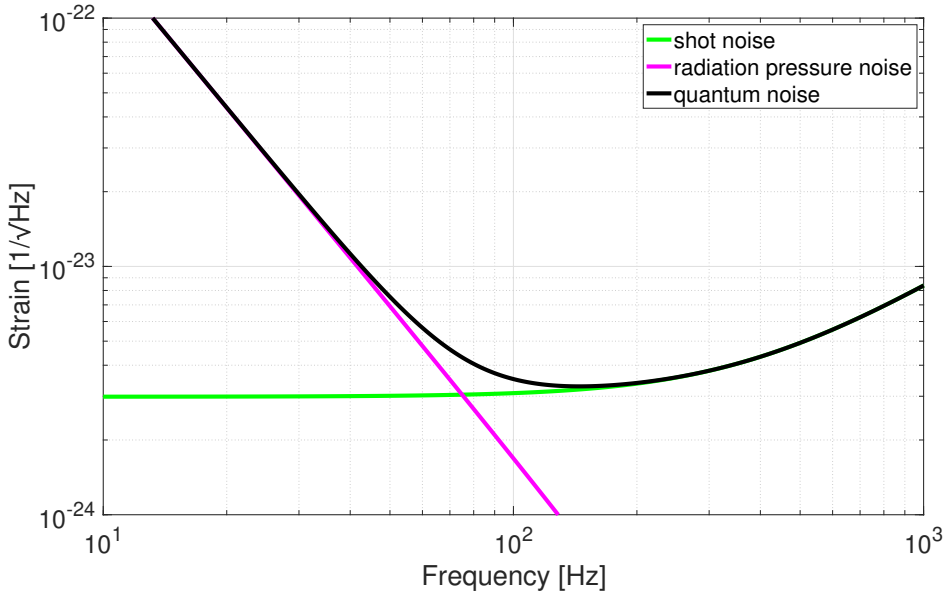

Figure 5.2: Quantum noise in GW detectors. In this figure, the KAGRA parameters shown in Table 5.1 are assumed.

There is a tradeoff between shot noise and radiation pressure noise in terms of laser power, and the quantum noise cannot surpass the standard quantum limit (SQL) h_{SQL}, as shown in Figure 5.3. When $\mathcal{K} = 1$, which corresponds to $\Omega \simeq \Omega_{\mathrm{SQL}}$ with $\Omega \ll \gamma_{\mathrm{ifo}}$, the quantum noise reaches the SQL.

Ponderomotive squeezing

Quantum noise in GW detectors can be better understood by considering the amplitude and phase picture, as shown in Figure 5.4. The vacuum field injected into the interferometer is reflected by the SRM without entering the interferometer at high frequencies, while at low frequencies, the vacuum field enters the interferometer, and the amplitude fluctuation of the vacuum induces test mass fluctuations through optomechanical coupling, leading to

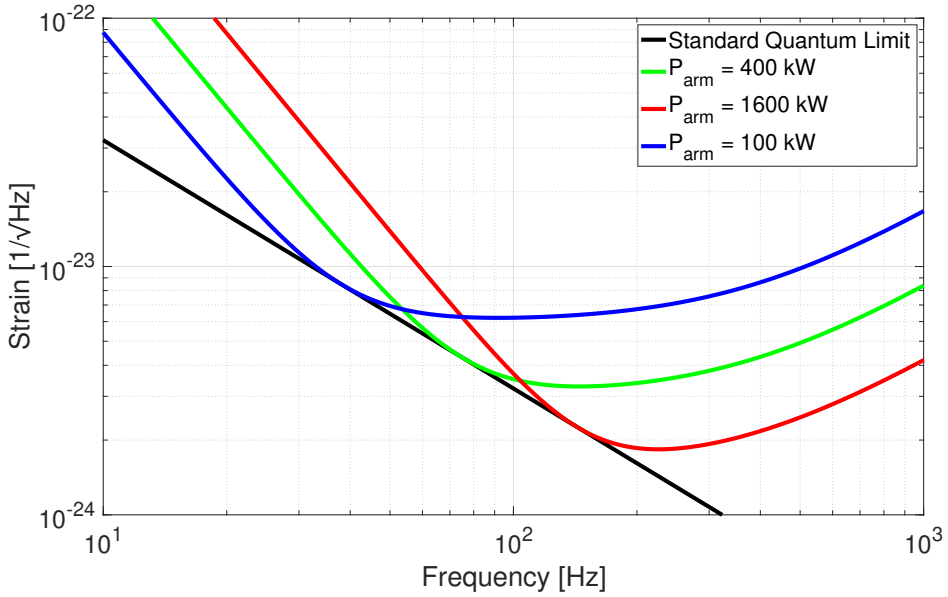

Figure 5.3: Quantum noise in GW detectors with various arm intracavity powers and the standard quantum limit.

the phase fluctuation. This is the origin of the radiation pressure noise. The output from the interferometer is squeezed at low frequencies, which is called ponderomotive squeezing.

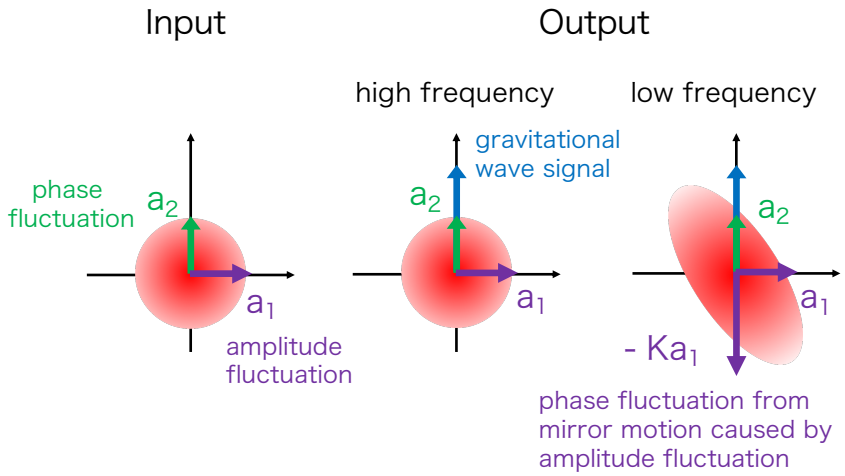

Figure 5.4: Ponderomotive squeezing.

5.2 Frequency-independent squeezing

To reduce the quantum noise, it was suggested to inject the squeezed vacuum states to the interferometer instead of the vacuum states as shown in Figure 5.5 [9].

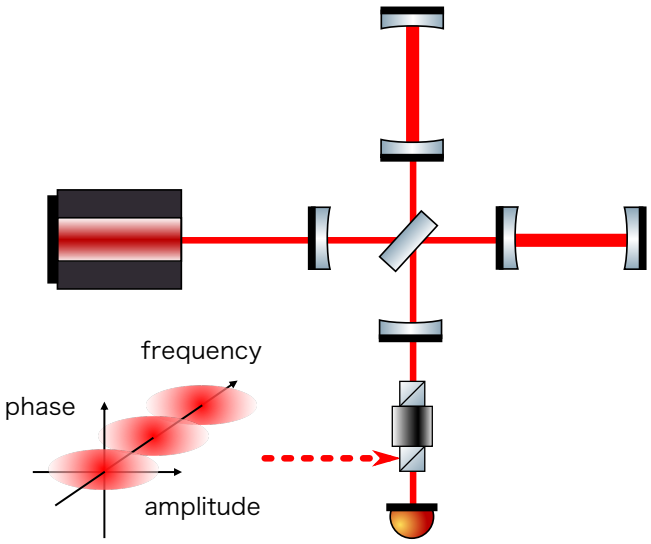

Figure 5.5: Injection of frequency-independent squeezing in GW detectors.

Quantum noise with frequency-independent squeezing can be expressed as [14]

$$S_{\rm sqz} = \frac{h_{\rm SQL}^2}{2}\left(\frac{1}{\mathcal{K}} + \mathcal{K}\right)(\cosh 2r - \sinh 2r \cos\left[2(\Phi - \phi_{\rm sqz})\right]), \tag{5.10}$$

where r is the injection squeezing factor, $\phi_{\rm sqz}$ is the injection squeezing angle, and $\Phi = {\rm arccot}\mathcal{K}$.

When the injection squeezing angle $\phi_{\rm sqz} = \pi/2$ (phase squeezing), Equation (5.10) is[1]

$$S_{\rm sqz}(\phi_{\rm sqz} = \pi/2) = \frac{h_{\rm SQL}^2}{2}\left(\frac{1}{\mathcal{K}e^{2r}} + \mathcal{K}e^{2r}\right). \tag{5.11}$$

The formula above indicates that the shot noise is reduced by a factor of e^{2r}, while the radiation pressure noise is increased by the same factor. The tradeoff between shot noise and radiation pressure noise remains, and the SQL cannot be surpassed with the phase squeezing. Shot noise reduction with phase squeezing was achieved in Advanced LIGO and Advanced Virgo in O3 [10, 11]. Furthermore, the increase in radiation pressure noise with frequency-independent squeezing was observed in Advanced LIGO and Advanced Virgo [12, 13].

[1] Here we used, $\cos 2\Phi = \cos^2\Phi - \sin^2\Phi = \dfrac{\mathcal{K}^2}{1+\mathcal{K}^2} - \dfrac{1}{1+\mathcal{K}^2} = -\dfrac{1-\mathcal{K}^2}{1+\mathcal{K}^2}$.

5.3 Frequency-dependent squeezing

To reduce the shot noise and radiation pressure noise simultaneously, frequency-dependent squeezed vacuum states, which are phase squeezed at high frequencies and amplitude squeezed at low frequencies, are required. When the injection squeezing angle has a frequency dependence, such as $\phi_{\rm sqz}(\Omega) = \Phi(\Omega) = {\rm arccot}\mathcal{K}(\Omega)$, the quantum noise with frequency-dependent squeezing (5.10) can be written as

$$S_{\rm sqz} = \frac{h_{\rm SQL}^2}{2}\left(\frac{1}{\mathcal{K}} + \mathcal{K}\right)e^{-2r}. \tag{5.12}$$

The formula above indicates that both of the shot noise and the radiation pressure noise can be reduced by a factor of e^{-2r}.

A comparison of the quantum noise with the vacuum, frequency-independent squeezing, and frequency-dependent squeezing are shown in Figure 5.6.

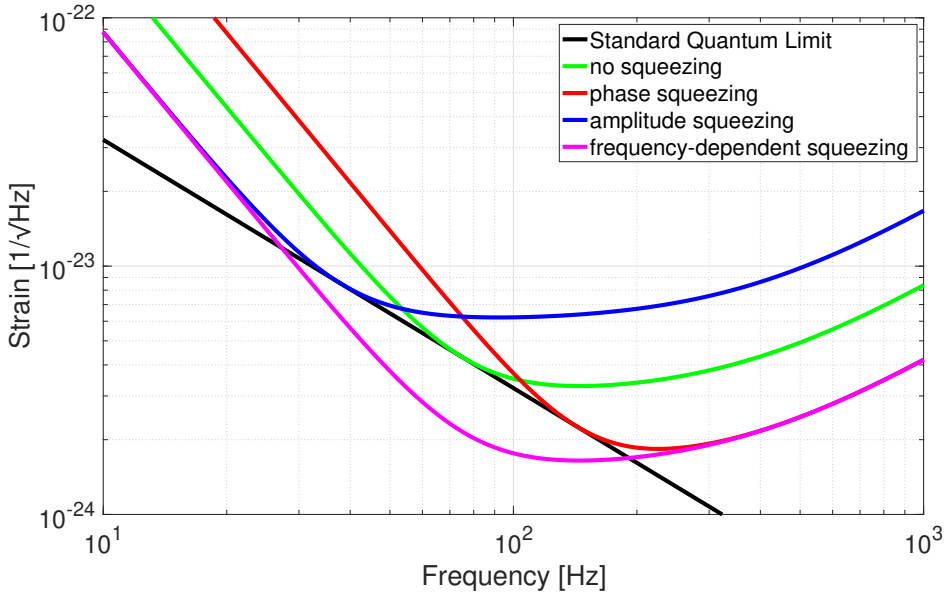

Figure 5.6: Quantum noise with vacuum, frequency-independent squeezing, and frequency-dependent squeezing.

5.4 Filter cavity

The most promising method to realize the frequency-dependent squeezing is by reflecting the frequency-independent squeezed vacuum field off a Fabry-Perot cavity, called the filter cavity [14]. The optical configuration of the frequency-dependent squeezing with the filter cavity is shown in Figure 5.7.

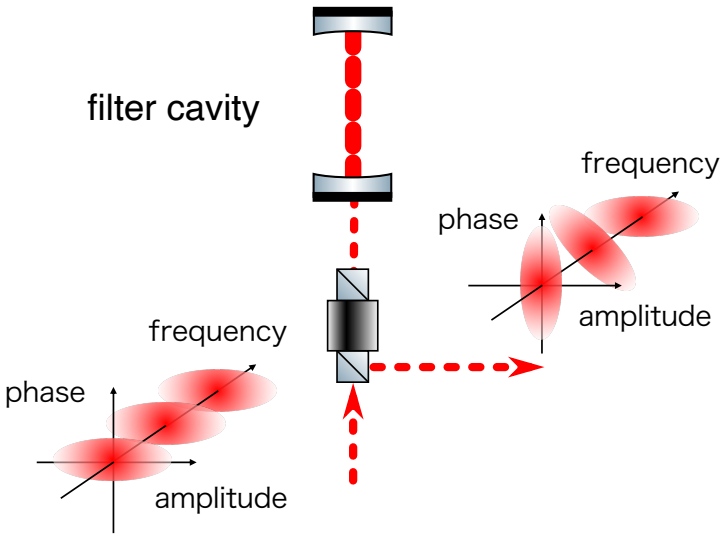

Figure 5.7: Optical configuration of frequency-dependent squeezing with the filter cavity. The squeezing angle rotates by 90° at low frequencies with the filter cavity, while the squeezing angle does not change at high frequencies.

The frequency-independent squeezed field is reflected by the filter cavity, acquiring a frequency dependence. This mechanism can be better understood in a sideband picture, where the squeezing angle at each frequency is determined by the average phase between the upper and lower sidebands, as shown in Figure 5.8. If the cavity is operating at a detuned configuration, the symmetric sidebands have a differential phase change depending on the cavity dispersion, resulting in a rotation of the squeeze ellipse in the quadrature plane.

Here, we theoretically derive the squeezing angle rotation by the filter cavity based on [52]. From Equation (3.18), the complex filter cavity reflectivity for a sideband frequency Ω can be written as follows:

$$r_{\rm fc}(\Omega) = r_{\rm in} - \frac{t_{\rm in}^2}{r_{\rm in}} \frac{r_{\rm rt} e^{-i\Phi(\Omega)}}{1 - r_{\rm rt} e^{-i\Phi(\Omega)}}, \tag{5.13}$$

where $r_{\rm in}$ is the amplitude reflectivity of the input mirror and $r_{\rm rt}$ is the cavity's round-trip amplitude reflectivity. The cavity round-trip phase $\Phi(\Omega)$ is

$$\Phi(\Omega) = (\Omega - \Delta\omega_{\rm fc}) \frac{2L_{\rm fc}}{c}, \tag{5.14}$$

where $\Delta\omega_{\rm fc} = \omega_{\rm fc} - \omega_0$ is the filter cavity detuning with respect to the carrier frequency ω_0 and $L_{\rm fc}$ is the filter cavity length.

For a high-finesse cavity near the resonance, we can assume that

$$e^{-i\Phi(\Omega)} \simeq 1 - i\Phi(\Omega), \tag{5.15}$$

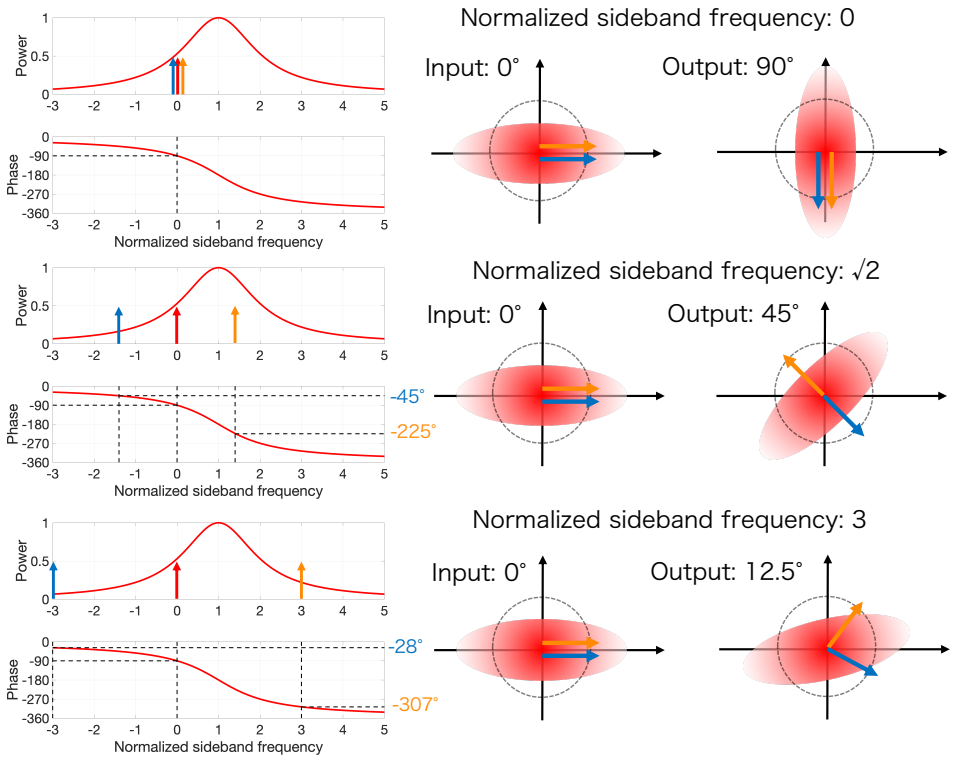

Figure 5.8: Squeezing angle rotation by the filter cavity. The red, orange, and blue arrows represent the carrier, upper sideband, and lower sideband, respectively. The left three plots represent the normalized intracavity power of the filter cavity and the phase of the filter cavity reflectivity for the normalized sideband frequency 0, $\sqrt{2}$, 3. The horizontal axis represents the sideband frequency normalized with respect to $\Delta\omega_{\mathrm{fc},0}$.

and

$$r_{\mathrm{rt}} \simeq r_{\mathrm{in}} \simeq \sqrt{1 - t_{\mathrm{in}}^2 - \Lambda_{\mathrm{rt}}^2} \simeq 1 - (t_{\mathrm{in}}^2 + \Lambda_{\mathrm{rt}}^2)/2, \tag{5.16}$$

where Λ_{rt}^2 is the round-trip loss in the cavity (not including the input mirror transmission).

Under these assumptions, the complex reflectivity of the filter cavity (5.13) can be written as follows:

$$r_{\mathrm{fc}}(\Omega) \simeq 1 - \frac{2-\epsilon}{1 + i\xi(\Omega)}, \tag{5.17}$$

where

$$\epsilon = \frac{f_{\mathrm{FSR}}}{\gamma_{\mathrm{fc}}}\Lambda_{\mathrm{rt}}^2, \tag{5.18}$$

$$\xi(\Omega) = \frac{\Omega - \Delta\omega_{\mathrm{fc}}}{\gamma_{\mathrm{fc}}}, \tag{5.19}$$

with f_{FSR} is the FSR of the filter cavity and γ_{fc} is the filter cavity half-bandwidth.

The amplitude and phase of the filter cavity reflectivity can be written as follows:

$$\rho_{\rm fc}(\Omega) = |r_{\rm fc}(\Omega)| = \sqrt{1 - \frac{(2-\epsilon)\epsilon}{1+\xi^2(\Omega)}}, \tag{5.20}$$

$$\alpha_{\rm fc}(\Omega) = \arg\{r_{\rm fc}(\Omega)\} = \arg\{-1+\epsilon+\xi^2(\Omega) + \ i(2-\epsilon)\xi(\Omega)\}. \tag{5.21}$$

We define the sum and difference of the amplitude and phase of the filter cavity reflectivity for the symmetric sidebands as follows:

$$\begin{aligned} \rho_{\pm} &= \rho_{\rm fc}(\pm\Omega), \ \alpha_{\pm} = \alpha_{\rm fc}(\pm\Omega), \\ \rho^{p}_{m} &= \frac{\rho_{+} \pm \rho_{-}}{2}, \ \alpha^{p}_{m} = \frac{\alpha_{+} \pm \alpha_{-}}{2}. \end{aligned} \tag{5.22}$$

The transfer matrix of the filter cavity in the two-photon formalism is

$$\mathbf{T_{fc}} = \mathbf{A_2} \cdot \begin{pmatrix} r_{+} & 0 \\ 0 & r_{-}^{*} \end{pmatrix} \cdot \mathbf{A_2^{-1}}, \tag{5.23}$$

where $r_{\pm} = r_{\rm fc}(\pm\Omega)$ and $\mathbf{A_2}$ is the conversion matrix from one-photon to the two-photon formalism,

$$\mathbf{A_2} = \frac{1}{\sqrt{2}} \begin{pmatrix} 1 & 1 \\ -i & i \end{pmatrix}. \tag{5.24}$$

From Equation (5.22) and (5.23), the transfer matrix of the filter cavity is

$$\mathbf{T_{fc}} = e^{i\alpha_m} \mathbf{R}_{\alpha_p} (\rho_p \mathbf{I} - i\rho_m \mathbf{R}_{\pi/2}), \tag{5.25}$$

where $\mathbf{R}_\theta$ is the 2×2 rotation matrix with the rotation angle θ and $\mathbf{I}$ is the 2×2 identity matrix. The first term represents the sidebands' phase rotation by α_p, which induces the squeezing angle rotation. The second term represents the effect of the filter cavity losses.

From (5.21) and (5.22), the squeezing rotation angle by the filter cavity is

$$\alpha_p(\Omega) \simeq \arctan\left(\frac{(2-\epsilon)\gamma_{\rm fc}\Delta\omega_{\rm fc}}{(1-\epsilon)\gamma_{\rm fc}^2 - \Delta\omega_{\rm fc}^2 + \Omega^2}\right), \tag{5.26}$$

which holds for the typical filter cavity parameters, $\epsilon \ll 1$ or $\Lambda_{\rm rt}^2 \ll t_{\rm in}^2$.

As the frequency region where the squeezing angle rotates is smaller than the interferometer bandwidth $\Omega \ll \gamma_{\rm ifo}$, Equation (5.2) can be approximated as follows:

$$\mathcal{K} \simeq \left(\frac{\Omega_{\rm SQL}}{\Omega}\right)^2. \tag{5.27}$$

The required squeezing angle rotation by the filter cavity is

$$\alpha_p \simeq \arctan\left(\frac{\Omega_{\rm SQL}}{\Omega}\right)^2. \tag{5.28}$$

From Equation (5.26) and (5.28), the optimal filter cavity bandwidth and detuning are

$$\Delta\omega_{\mathrm{fc},0} = \sqrt{1-\epsilon}\gamma_{\mathrm{fc}}, \tag{5.29}$$

$$\gamma_{\mathrm{fc}} = \sqrt{\frac{2}{(2-\epsilon)\sqrt{1-\epsilon}}}\frac{\Omega_{\mathrm{SQL}}}{\sqrt{2}}. \tag{5.30}$$

In the case of KAGRA, $\Omega_{\mathrm{SQL}} = 76$ Hz and the filter cavity half bandwidth should be $\gamma_{\mathrm{fc}} \sim \Omega_{\mathrm{SQL}}/\sqrt{2} = 54$ Hz. This requires a long and high finesse filter cavity.

From Equation (5.18) and (5.30), we can solve for ϵ as follows:

$$\epsilon = \frac{4}{2+\sqrt{2+2\sqrt{1+\left(\frac{2\Omega_{\mathrm{SQL}}}{f_{\mathrm{FSR}}\Lambda_{\mathrm{rt}}^2}\right)^4}}}. \tag{5.31}$$

From this formula, the effect of the filter cavity losses ϵ is determined by $\Lambda_{\mathrm{rt}}^2/L_{\mathrm{fc}}$ once Ω_{SQL} is fixed. When we have a longer filter cavity, the finesse of the filter cavity will be lower to achieve the same half bandwidth of the filter cavity, and therefore, the effect of the filter cavity losses decreases. As these filter cavity losses are one of the most dominant squeezing degradation sources, LIGO and Virgo plan to install a 300 m filter cavity from O4.

5.5 Analytical model of squeezing degradation sources

In this section, an analytical model of the squeezing degradation sources and a calculation of quantum noise with the filter cavity based on [52] is introduced. The squeezing degradation sources in GW detectors with the filter cavity are shown in Figure 5.9. There are mainly three degradation sources: loss, phase noise, and mode mismatch. The loss is composed of extra-cavity/intracavity loss of the filter cavity. The extra-cavity loss can be divided into the injection/readout loss of the interferometer. The phase noise is composed of an extra-cavity/intracavity phase fluctuation. The mode mismatch is composed of a mismatch between the squeezer/filter cavity and the squeezer/local oscillator.

To calculate the quantum noise with the squeezing degradation sources, we divide the quantum noise into the following three parts: noise due to vacuum fluctuations passing through the squeezer N_1, noise due to vacuum fluctuations that do not pass through squeezer N_2, and noise due to vacuum fluctuations in the readout N_3.

Quantum noise at the interferometer readout is given by the following:

$$\begin{aligned} N(\zeta) &= |\bar{\mathbf{b}}_\zeta \cdot \mathbf{T}_1 \cdot v_1|^2 + |\bar{\mathbf{b}}_\zeta \cdot \mathbf{T}_2 \cdot v_2|^2 + |\bar{\mathbf{b}}_\zeta \cdot \mathbf{T}_3 \cdot v_3|^2 \\ &\equiv N_1 + N_2 + N_3, \end{aligned} \tag{5.32}$$

where $v_i = \sqrt{2\hbar\omega_0}\mathbf{I}$ $(i = 1, 2, 3)$ is vacuum fluctuation and $\mathbf{I}$ is 2×2 identity matrix. $\bar{\mathbf{b}}_\zeta = A_{\mathrm{LO}}(\sin\zeta \;\; \cos\zeta)$ is local oscillator and $N(\zeta = 0)$ is the quantum noise in the quadrature containing the interferometer signal.

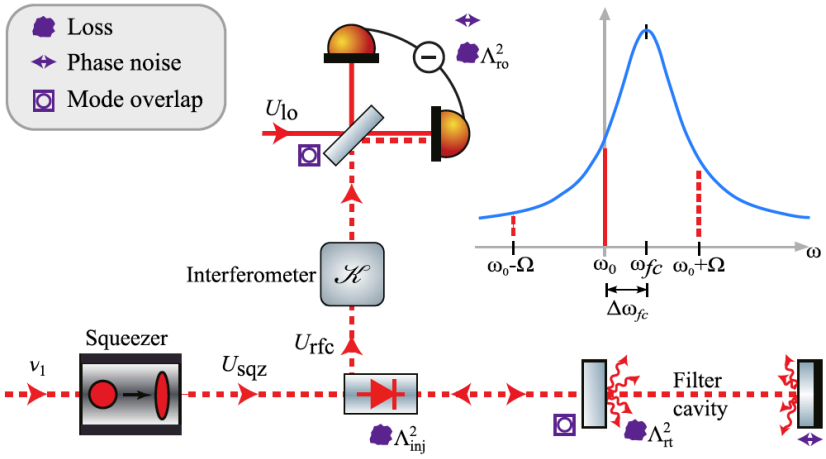

Figure 5.9: Squeezing degradation sources with the filter cavity in the GW detectors [52].

$\mathbf{T}_1$ is written as

$$\mathbf{T}_1 = \tau_{ro}\mathbf{T_{ifo}}(\mathbf{T_{00}}\mathbf{T_{fc}} + \mathbf{T_{mm}})\mathbf{T_{inj}}, \tag{5.33}$$

$$\mathbf{T_{ifo}} = \begin{pmatrix} 1 & 0 \\ -\mathcal{K} & 1 \end{pmatrix}, \tag{5.34}$$

$$\mathbf{T_{00}} = |t_{00}|\mathbf{R}_{\arg(t_{00})}, \mathbf{T_{mm}} = |t_{mm}|\mathbf{R}_{\arg(t_{mm})}, \tag{5.35}$$

$$\mathbf{T_{inj}} = \tau_{inj}\mathbf{R}_{\phi}\begin{pmatrix} e^{\sigma} & 0 \\ 0 & e^{-\sigma} \end{pmatrix}\mathbf{R}_{-\phi}, \tag{5.36}$$

where $\mathbf{T_{ifo}}$, $\mathbf{T_{fc}}$, and $\mathbf{T_{inj}}$ are transfer matrices of interferometer, optimally matched filter cavity, and injection field, respectively. $\mathbf{T_{00}}$ and $\mathbf{T_{mm}}$ are transfer matrices of 00 mode and higher order modes, respectively.

τ_{inj}, τ_{ro} in Equation (5.33) and (5.36) are the injection and readout transmissivity, respectively, and can be written as

$$\tau_{inj} = \sqrt{1-\Lambda^2_{inj}}, \tag{5.37}$$

$$\tau_{ro} = \sqrt{1-\Lambda^2_{ro}}, \tag{5.38}$$

where Λ^2_{inj} and Λ^2_{ro} are injection and readout losses, respectively.

t_{00}, t_{mm} in Equation (5.35) can be written as $t_{00} = a_0 b_0^*$, $t_{mm} = \sum_{n=1}^{\infty} a_n b_n^*$ where a_n, b_n are complex coefficients when we express the squeezed vacuum states and the local oscillator in the basis of the filter cavity mode and can be written as

$$U_{sqz} = \sum_{n=0}^{\infty} a_n U_n, \text{with} \sum_{n=0}^{\infty} |a_n|^2 = 1, \tag{5.39}$$

$$U_{lo} = \sum_{n=0}^{\infty} b_n U_n, \text{with} \sum_{n=0}^{\infty} |b_n|^2 = 1, \tag{5.40}$$

where U_n are the orthogonal basis of spatial modes and U_0 is the filter cavity fundamental mode.

σ and ϕ in Equation (5.36) are the injection squeezing factor and injection squeezing angle.

$\mathbf{T}_2$ is written as

$$\begin{aligned} \mathbf{T}_2 &= \tau_{\mathrm{ro}}\mathbf{T}_{\mathbf{ifo}}\Lambda_2, && (5.41)\\ \Lambda_2 &= \sqrt{1-(|\tau_2(\Omega)|^2+|\tau_2(-\Omega)|^2)/2}, && (5.42)\\ \tau_2(\Omega) &= (t_{00}r_{\mathrm{fc}}(\Omega)+t_{\mathrm{mm}})\tau_{\mathrm{inj}}. && (5.43) \end{aligned}$$

$\mathbf{T}_3$ is written as

$$\mathbf{T}_3 = \Lambda_{\mathrm{ro}}. \tag{5.44}$$

Quantum noise normalized with respect to shot noise level is

$$\hat{N} = \frac{N}{2\hbar\omega_0 A_{\mathrm{LO}}^2}. \tag{5.45}$$

Phase noise

Phase noise is the squeezing angle fluctuation that degrades the squeezing level by coupling to anti-squeezing. Phase noise in the filter cavity can be divided into two components: extra-cavity fluctuations (i.e., frequency-independent phase noise) and intracavity fluctuations (i.e., frequency-dependent phase noise).

Assuming multiple incoherent noise parameters X_n in quantum noise $\hat{N}$ have small Gaussian-distributed fluctuations with a variance δX_n^2, the average readout noise is given by

$$\hat{N}_{\mathrm{avg}} \simeq \hat{N} + \sum_n \left(\frac{\hat{N}(X_n+\delta X_n)+\hat{N}(X_n-\delta X_n)}{2} - \hat{N} \right). \tag{5.46}$$

For frequency-independent phase noise, $X_n = \phi$, which is the injection squeezing angle. For frequency-dependent phase noise, $X_n = \Delta\omega_{\mathrm{fc}}$, which is the filter cavity detuning. This detuning noise results from filter cavity length noise δL_{fc}, driven by seismic motion of the cavity mirrors or sensor noise of the filter cavity length control loop, according to

$$\delta\Delta\omega_{\mathrm{fc}} = \frac{\omega_0}{L_{\mathrm{fc}}}\delta L_{\mathrm{fc}}. \tag{5.47}$$

First, the calculation of frequency-independent phase noise is presented. Frequency-independent phase noise can be represented by variations of injection squeezing angle, $\delta\phi$.

To calculate the effect of only phase noise, we restrict our discussion to an optimally matched filter cavity and without injection and readout losses. From Equation (5.32)-(5.38) and (5.45), quantum noise owing to vacuum fluctuations passing through the

squeezer, $\hat{N}_1$ can be written as follows:

$$\begin{aligned}
\hat{N}_1(\phi) &= A\cos^2\phi + 2B\cos\phi\sin\phi + C\sin^2\phi, && (5.48)\\
A &= (\rho_p^2 e^{-2\sigma} + \rho_m^2 e^{2\sigma})(\cos\alpha_p + \mathcal{K}\sin\alpha_p)^2 \\
&+ (\rho_p^2 e^{2\sigma} + \rho_m^2 e^{-2\sigma})(\mathcal{K}\cos\alpha_p - \sin\alpha_p)^2, && (5.49)\\
B &= (e^{2\sigma} - e^{-2\sigma})(\rho_m^2 - \rho_p^2) \\
&\times (\cos\alpha_p + \mathcal{K}\sin\alpha_p)(\mathcal{K}\cos\alpha_p - \sin\alpha_p), && (5.50)\\
C &= (\rho_p^2 e^{2\sigma} + \rho_m^2 e^{-2\sigma})(\cos\alpha_p + \mathcal{K}\sin\alpha_p)^2 \\
&+ (\rho_p^2 e^{-2\sigma} + \rho_m^2 e^{2\sigma})(\mathcal{K}\cos\alpha_p - \sin\alpha_p)^2. && (5.51)
\end{aligned}$$

When $\phi = 0$, $\hat{N}_1(\phi = 0) = A$ and this represents the quantum noise of an optimally matched filter cavity without injection and readout losses, Equation (44) in [52].

From Equation (5.46), the frequency-independent phase noise of $\hat{N}_1$ can be calculated as follows:

$$\hat{N}_{1,\mathrm{avg}}(\phi) = \frac{\hat{N}_1(\delta\phi) + \hat{N}_1(-\delta\phi)}{2} = A\cos^2\delta\phi + C\sin^2\delta\phi. \tag{5.52}$$

Frequency-dependent phase noise can be calculated by averaging $\hat{N}_1(\Delta\omega_{\mathrm{fc},0} + \delta\Delta\omega_{\mathrm{fc}})$ and $\hat{N}_1(\Delta\omega_{\mathrm{fc},0} - \delta\Delta\omega_{\mathrm{fc}})$,

$$\hat{N}_{1,\mathrm{avg}}(\Delta\omega_{\mathrm{fc},0}) = \frac{\hat{N}_1(\Delta\omega_{\mathrm{fc},0} + \delta\Delta\omega_{\mathrm{fc}}) + \hat{N}_1(\Delta\omega_{\mathrm{fc},0} - \delta\Delta\omega_{\mathrm{fc}})}{2}. \tag{5.53}$$

For the calculation of frequency-dependent phase noise, we can consider only N_1 because the frequency-dependent phase noise for N_2 is negligible compared to N_1, and N_3 is independent of the filter cavity.

5.6 Squeezing degradation budget in 300 m filter cavity

Quantum noise with the squeezing degradation sources in the filter cavity (5.32) can be numerically calculated. The realistic squeezing degradation sources in the 300 m filter cavity and the corresponding squeezing degradation budget are presented in Table 5.2 and Figure 5.10. The quantum noise can be reduced at all frequencies with a 300 m filter cavity. In particular, the quantum noise can be reduced by 4 dB at low frequencies and 6 dB at high frequencies.

As shown in Figure 5.10, the mode mismatch is the most dominant degradation source at low frequencies, while the injection and readout losses are the most dominant at high frequencies. As the filter cavity losses are not the most dominant noise source, increasing the filter cavity length more than 300 m will not significantly improve the overall sensitivity.

Table 5.2: Squeezing degradation sources in 300 m filter cavity.

Parameter	Symbol	Value
Filter cavity losses	Λ^2_{rt}	80 ppm
Injection losses	Λ^2_{inj}	5 %
Readout losses	Λ^2_{ro}	5 %
Mode-mismatch squeezer-filter cavity	$\Lambda^2_{\mathrm{mmFC}}$	2 %
Mode-mismatch squeezer-local oscillator	$\Lambda^2_{\mathrm{mmLO}}$	5 %
Frequency-independent phase noise (RMS)	$\delta\phi$	30 mrad
Filter cavity length noise (RMS)	δL_{fc}	1 pm
Generated squeezing	σ_{dB}	9 dB

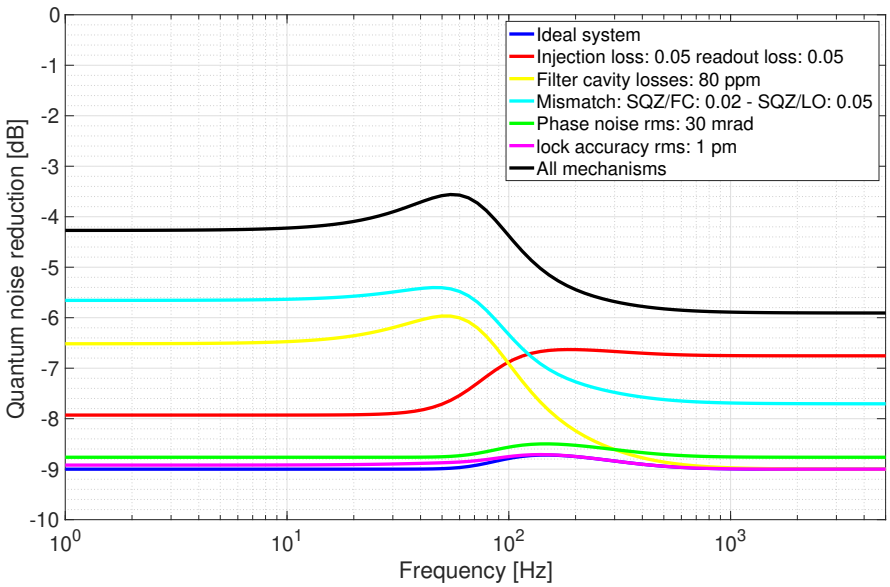

Figure 5.10: Squeezing degradation budget in 300 m filter cavity. The squeezing degradation parameters are listed in Table 5.2.

5.7 Sensitivity improvement of KAGRA

The sensitivity improvement of KAGRA with a 300 m filter cavity is shown in Figure 5.11. The KAGRA sensitivity for BRSE without a filter cavity is 129 Mpc, and the filter cavity can improve the sensitivity up to 188 Mpc. The GW event rate will improve by a factor of 3.

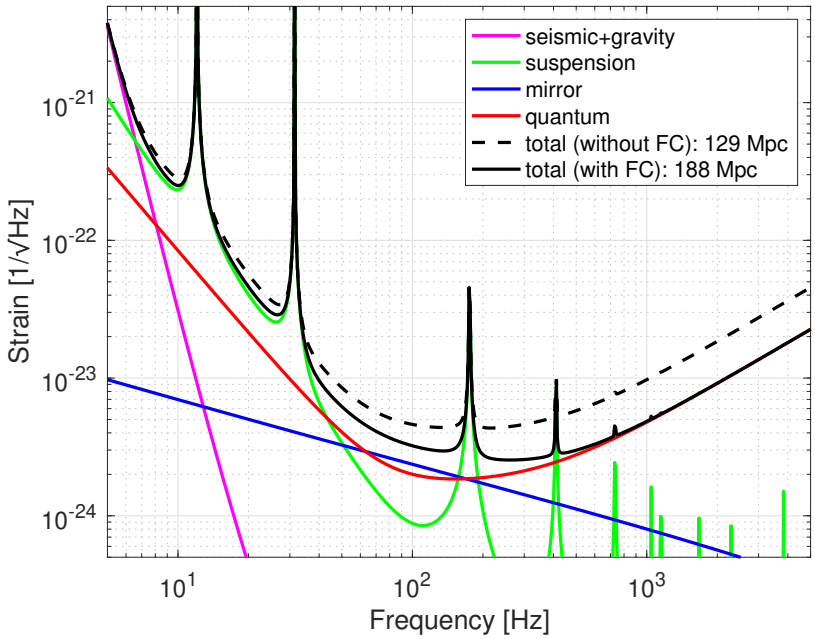

Figure 5.11: Sensitivity improvement of KAGRA with a 300 m filter cavity. The black solid and dashed lines represent the KAGRA sensitivity (BRSE) with and without the 300 m filter cavity, respectively. In this calculation, the arm intracavity power is 337 kW, which corresponds to the power at BS of 674 W. The half bandwidth and detuning of the filter cavity are 51 Hz and 47 Hz, respectively. The squeezing degradation parameters are based on Table 5.2, although the mode mismatch and phase noise are not included in this calculation.

Chapter 6

Frequency-Independent Squeezing

The two key components to realize the frequency-dependent squeezing are the filter cavity and the squeezed vacuum source. To realize frequency-dependent squeezing with rotation below 100 Hz, a frequency-independent squeezed vacuum source capable of producing squeezing below 100 Hz is necessary. In this chapter, the development of the frequency-independent squeezed vacuum source is explained. I mainly contributed to the implementation of the homodyne detector and coherent control and realization of the 5.4 dB of frequency-independent squeezing down to 20 Hz in this chapter.

6.1 Experimental setup

The in-air squeezed vacuum source in this experiment follows the design of the GEO600 squeezer [53]. The optical layout of the squeezed vacuum source is shown in Figure 6.1. The simplified optical layout is shown in Figure 6.2. The core part is an optical parametric oscillator (OPO) which is a linear cavity hosting a periodically poled potassium titanyl phosphate (PPKTP) crystal. The squeezed vacuum is generated from a parametric down-conversion process in the crystal. This process requires a pump field at twice the frequency of the squeezed field and the pump field is generated by injecting a 1064 nm laser into a second harmonic generator (SHG). The main laser, a 2-W 1064-nm Nd:YAG laser, is used to pump the SHG, which generates a green field with a wavelength of 532 nm, and is used as a local oscillator (LO) for the balanced homodyne detector to measure the squeezing. An infrared mode cleaner (IRMC) cavity is installed to clean the beam shape of the LO before it reaches the homodyne detector. A green mode cleaner (GRMC) cavity and a Mach-Zehnder interferometer (MZ) are installed along the green path, respectively, to clean the beam shape and to stabilize the power of the green pump field before it reaches the OPO. Two auxiliary lasers, which are phase-locked to the main laser with a frequency offset, are also used. The first one (Auxiliary Laser 1 or coherent control (CC) laser) is injected into the OPO and copropagates with the squeezed vacuum field up to the homodyne detector for CC. The second one (Auxiliary Laser 2 or p-pol laser) is also injected into the OPO with an orthogonal polarization with respect to the generated squeezed field and is used to control the OPO length.

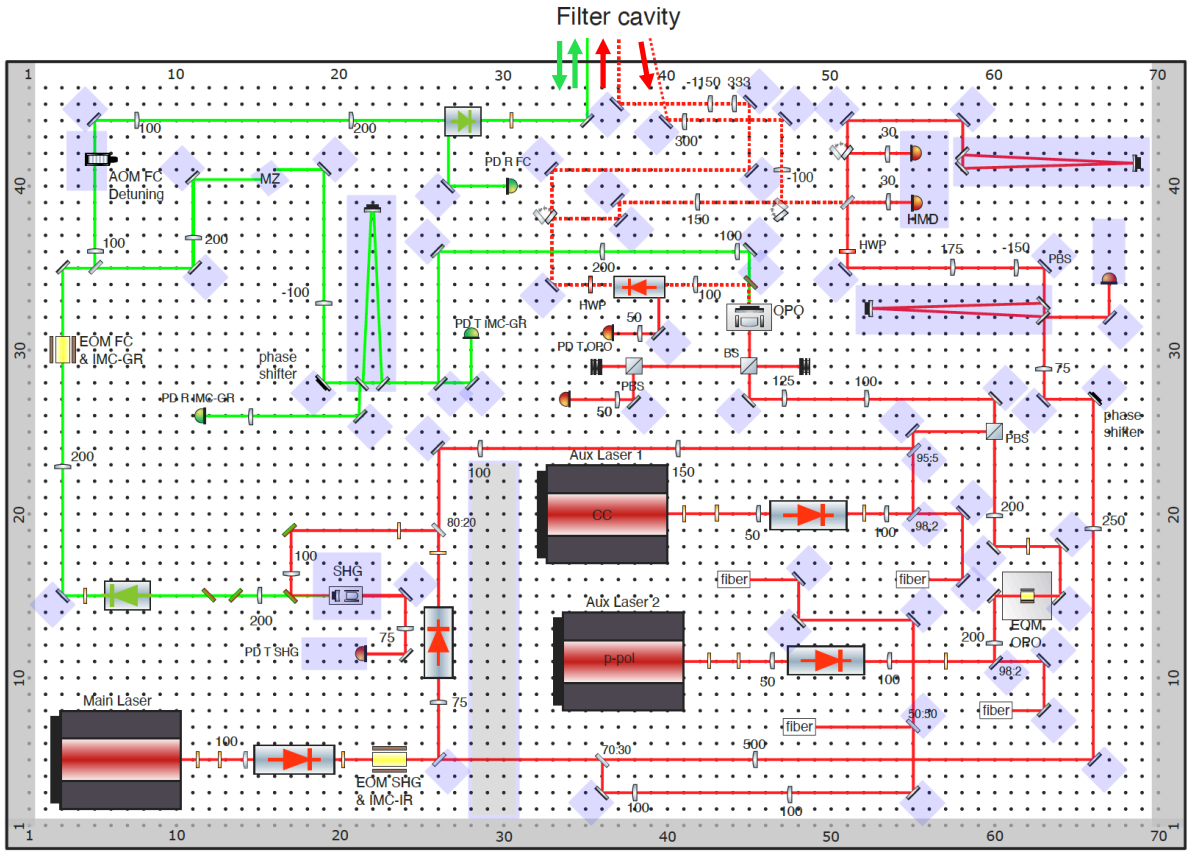

Figure 6.1: Optical layout of frequency-independent squeezed vacuum source.

For the alignment of the squeezed vacuum field, a pickoff of the main laser is temporarily injected into the OPO and copropagates with the squeezed vacuum field (we refer to this beam as a seed beam or bright alignment beam). This beam is also used for the characterization of the OPO (such as nonlinear gain) and the filter cavity (such as finesse, locking accuracy, and round-trip losses), which will be explained later.

Two flipping mirrors are placed on the squeezing path so that we can switch between sending the squeezing directly to the homodyne detector and sending it to the filter cavity. A steering mirror placed before the homodyne detector is also a flipping mirror so that we can switch between sending the squeezing to the homodyne detector and sending it to an alignment mode cleaner (AMC), which will be explained in Section 6.9. It should be noted that the AMC is not shown in Figure 6.2.

6.2 Laser sources

The laser sources used in this experiment are 1064 nm Nd:YAG lasers. There are mainly two constraints on the current and temperature of the laser sources. One is the mode hopping of the lasers and another is the limited frequency range (400 MHz) of the phase-

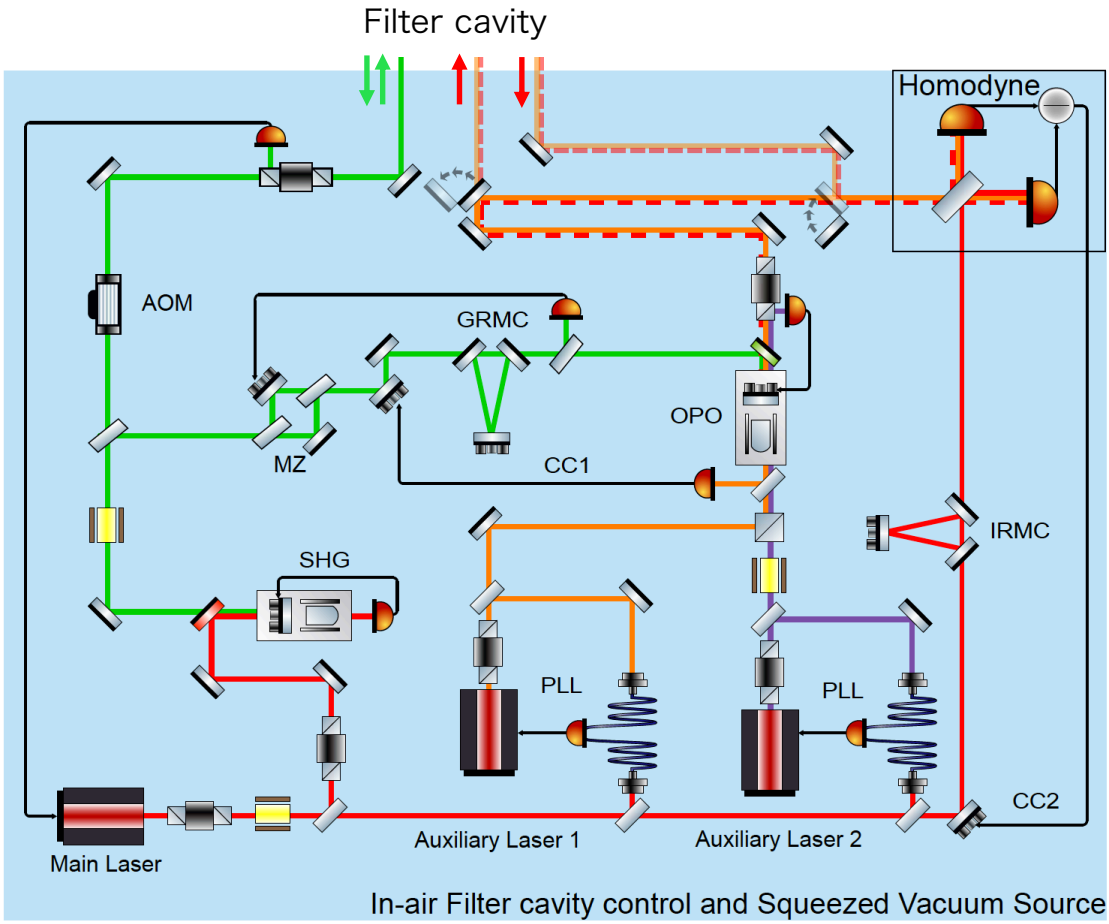

Figure 6.2: Simplified optical layout of frequency-independent squeezed vacuum source.

locked loop (PLL), which limits the maximum frequency offset that the auxiliary lasers can have with respect to the main laser. Therefore, the current and temperature of the lasers have to be chosen so that we can avoid the mode hopping of the three lasers and ensure that the two beat notes of the main laser/p-pol laser and the main laser/CC laser are within the PLL frequency range. The current and temperature settings used are listed in Table 6.1.

Table 6.1: Current and temperature of the laser sources.

	Main laser	CC laser	p-pol laser
Current (A)	1.832	1.185	1.338
Temperature (°C)	23.11	38.15	32.49

6.3 Direct digital synthesizer

All the RF sources used in the experiment were generated using direct digital synthesizers (DDS). The amplitude, frequency, and phase of the RF sources were digitally controlled.

There were three DDS boards, and each DDS board has four RF channels. The DDS channel list used in this experiment is shown in Table 6.2. In DDS1, CH0 and CH1 provided the modulation and demodulation RF sources for SHG/IRMC. CH2 and CH3 in DDS1 provided the modulation and demodulation RF sources for OPO. In DDS2, CH0 provided the modulation RF sources for FC/GRMC (FC indicates green lock for the filter cavity, which will be explained in Chapter 7), and CH1 and CH2 provided the demodulation RF sources for FC and GRMC. CH3 in DDS2 provided the demodulation RF sources for the two quadrant photodiodes (QPDs) for auto alignment. In DDS3, CH0 and CH1 provided the LO for the CC and p-pol PLL, respectively. CH2 in DDS3 provided the demodulation RF sources for CC1/CCFC (CCFC is a control loop for the filter cavity with coherent control sidebands, which will be explained in Chapter 8). CH3 in DDS3 provided the demodulation RF source for CC2. CH1 in DDS1 (for SHG/IRMC demodulation), CH3 in DDS2 (for two QPDs demodulation), and CH2 in DDS3 (for CC1/CCFC demodulation) were split with 50:50 power splitters (Z99SC-62-S+).

Table 6.2: DDS channel list

DDS1		
channel	function	frequency
CH0	SHG/IRMC EOM	15.2 MHz
CH1	SHG/IRMC demod	15.2 MHz
CH2	OPO EOM	87.6 MHz
CH3	OPO demod	87.6 MHz
DDS2		
channel	function	frequency
CH0	FC/GRMC EOM	78 MHz
CH1	FC demod	78 MHz
CH2	GRMC demod	78 MHz
CH3	AA demod	78 MHz
DDS3		
channel	function	frequency
CH0	CC PLL LO	7 MHz
CH1	p-pol PLL LO	< 400 MHz
CH2	CC1/CCFC demod	14 MHz
CH3	CC2 demod	7 MHz

6.4 Phase-locked loop

The frequencies of the main laser and the auxiliary lasers are locked by the phase-locked loop (PLL). The configuration of the PLL is shown in Figure 6.3. The Phase Detector/Frequency Synthesizer (ADF4002 in Analog devices) is used for the PLL. The frequency range that the ADF4002 can handle as a voltage-controlled oscillator (VCO) is 400 MHz.

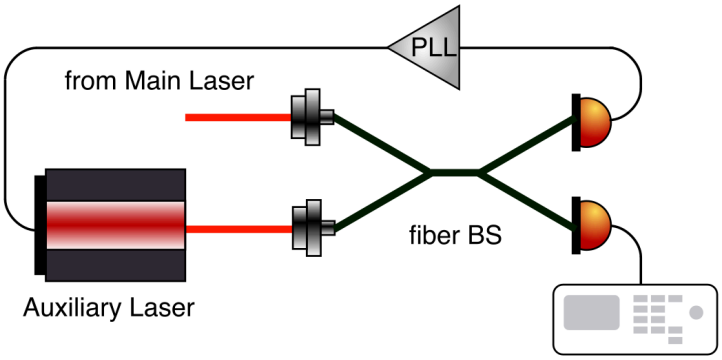

Figure 6.3: Configuration of PLL. Parts of the main laser and the auxiliary lasers are picked off and combined with a fiber BS. One of the two outputs is fed back to the frequency of the auxiliary lasers to follow the frequency of the main laser. Another output of the fiber BS is used for monitoring the frequency of the beat note.

6.5 Second harmonic generator

The second harmonic generator (SHG) is a cavity composed of a nonlinear crystal ($MgO : LiNbO_3$) and a meniscus mirror. The SHG converts 1064 nm of the IR field into 532 nm of the green field through a nonlinear process. The schematic of the cross section of the SHG cavity used in this experiment is shown in Figure 6.4. The optical parameters of the SHG are listed in Table 6.3.

Table 6.3: SHG design parameters.

Cavity parameter	Value
$MgO : LiNbO_3$ HR reflectivity	99.95 % (IR), 99.8 % (GR)
$MgO : LiNbO_3$ AR reflectivity	< 0.1 % (IR, GR)
Meniscus HR reflectivity	92 % (IR), 2 % (GR)
$MgO : LiNbO_3$ RoC	12 mm (HR), ∞ (AR)
Meniscus RoC	25 mm (HR), 20 mm (AR)
Optical cavity length	38 mm
FSR	4 GHz
FWHM	55 MHz (IR), 2.9 GHz (GR)
Finesse	73 (IR), 1.4 (GR)

6.5.1 Finesse

The IR finesse of the SHG was measured by the cavity scan. To avoid the conversion from IR to green in the SHG, the SHG temperature was set in the region where the nonlinear effect in the SHG is small during the cavity scan. The SHG cavity scan is shown in Figure 6.5. The measured IR finesse of the SHG is 70, which is close to the design finesse.

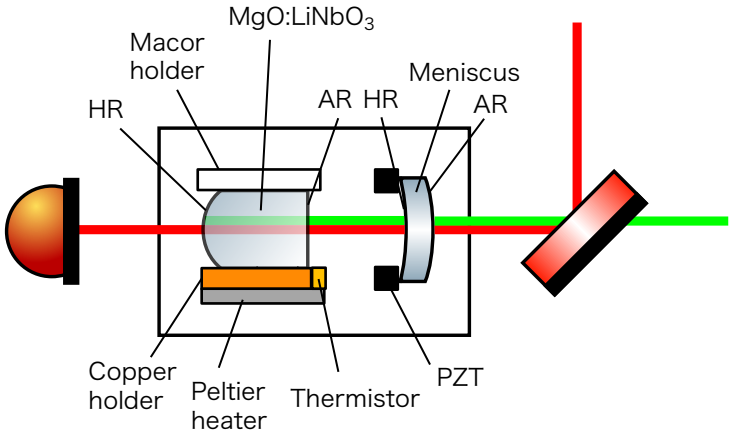

Figure 6.4: Schematic of cross section of SHG. The injected IR field is p-polarized and generated green field is s-polarized. The conversion efficiency of the SHG from IR to green is 35 %. The SHG cavity length is controlled with a Piezoelectric (PZT) actuator attached to the meniscus mirror. The PDH signal of the SHG cavity is obtained at the SHG transmission and fed back to the PZT actuator. The temperature of the crystal is monitored with the thermistors and controlled with the Peltier heaters.

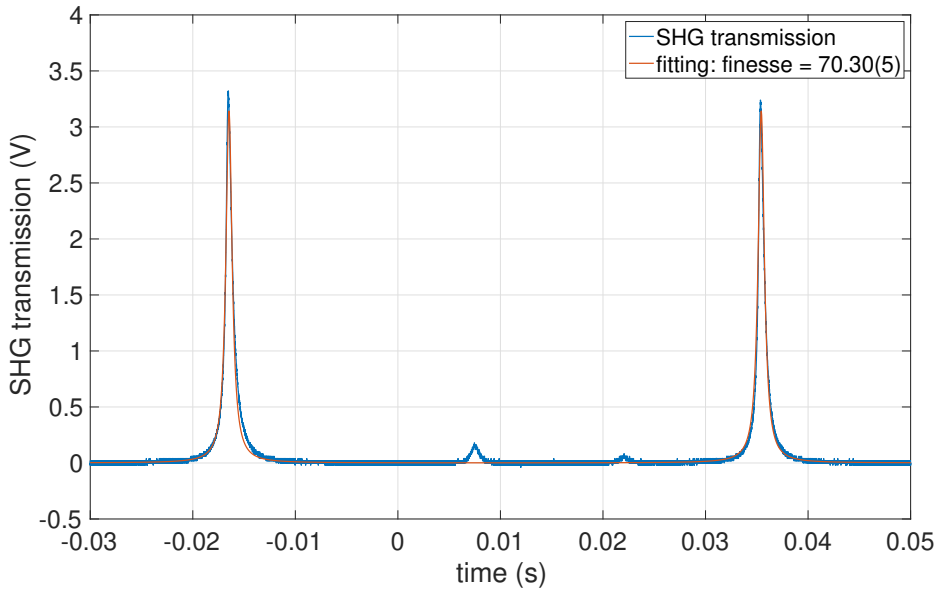

Figure 6.5: SHG cavity scan. The blue and red lines represent the SHG transmission curve and its fitting curve, respectively. The offset was removed from the data. The finesse value obtained from the fitting is 70.30(5) which is close to the expected value.

6.5.2 Length control

The open-loop transfer function of SHG cavity length control is shown in Figure 6.6.

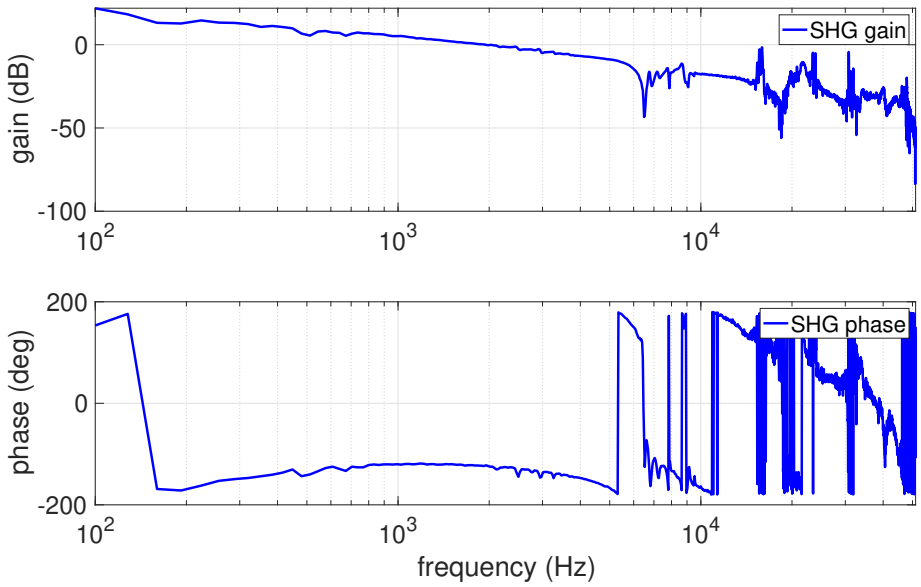

Figure 6.6: Open-loop transfer function of SHG cavity length control. The UGF is 2 kHz and the phase margin is 56 deg.

6.5.3 Temperature control

The temperature of the nonlinear crystal inside the SHG is controlled for phase matching. The temperature control is composed of thermistors (103JT-025), Peltier heaters (CP0.8-31-06L), and a temperature controller (Thorlabs TED200C). According to the manual of the thermistor and temperature controller, the relation between the resistance R and the temperature T of the thermistor is

$$T(R) = \frac{BT_0}{T_0 \ln \frac{R}{R_0} + B}, \tag{6.1}$$

where $R_0 = 10$ kΩ is the nominal resistance of the thermistor at the nominal temperature of $T_0 = 298.15$ K and $B = 3435$ K is the energy constant of the thermistor. We can set the target resistance of the thermistor in the temperature controller and the difference between the target resistance and current resistance is sent to the Peltier heaters.

To determine the optimal temperature for the SHG, we measured the generated green power from the SHG as a function of the SHG temperature as shown in Figure 6.7. The shape of the generated green power is not symmetric around the optimal temperature unlike Figure 4.2, which is the case for the single-pass SHG. This asymmetry is caused by the phase shift of the fundamental and second harmonics in the forward and backward passes in the SHG cavity (double pass) [54, 55, 56]. The generated second harmonic power with the double pass can be written as

$$P_2 \propto \left| \int_0^L \left[\frac{e^{i\Delta k z}}{1 - i\frac{z - z_0}{z_R}} + e^{i\phi + i\Delta k L} \frac{e^{i\Delta k z}}{1 - i\frac{z - (L - z_0)}{z_R}} \right] dz \right|^2, \tag{6.2}$$

where L is the crystal length, z_0 is the distance between the entrance surface of the crystal and the beam waist, $z_R = kw_0^2/2$ is the Rayleigh range, and w_0 is the radius of the beam waist. $\phi = \phi_2 - 2\phi_1$ where ϕ_1 and ϕ_2 are the phases of the fundamental and second harmonics, respectively.

For the plane wave ($z_R \to \infty$), the generated second harmonic power is

$$P_2 \propto \mathrm{sinc}^2\left(\frac{\Delta kL}{2}\right)\cos^2\left(\frac{\phi + \Delta kL}{2}\right). \tag{6.3}$$

There is an additional factor of $\cos^2\left(\frac{\phi+\Delta kL}{2}\right)$ compared with the single pass, which causes the asymmetry around the optimal temperature, as shown in Figure 6.7.

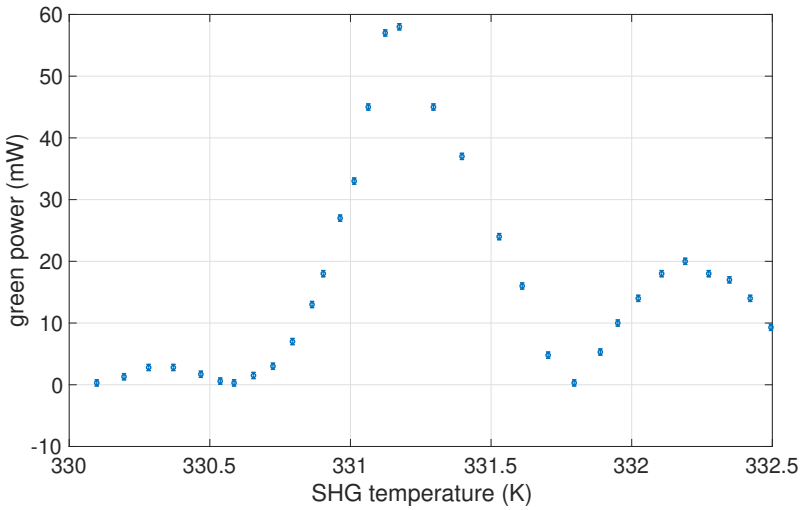

Figure 6.7: Generated green power from SHG as a function of SHG temperature.

6.6 Green and infrared mode cleaners

The GRMC and IRMC are triangular cavities used to clean the beam shapes of the green pump field and the LO, respectively. The configurations of GRMC and IRMC are shown in Figure 6.8. They have the same configurations, apart from wavelength.

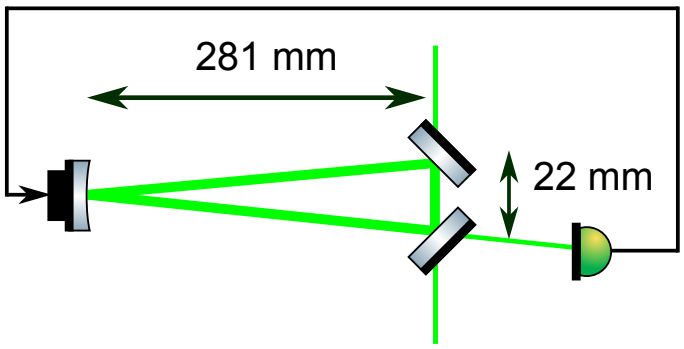

Figure 6.8: Configuration of GRMC. The configuration of IRMC is the same as GRMC apart from wavelength. The triangular cavity is composed of one top mirror with the PZT actuator and two bottom mirrors (input, output mirrors). The PDH signal of the cavity is obtained at the cavity reflection and fed back to the PZT actuator of the top mirror.

The optical parameters of the green and infrared mode cleaners are shown in Table 6.4. The optical parameters of the GRMC/IRMC are also the same, apart from the wavelength. The nominal GRMC/IRMC transmissivity is 89 % without any losses.

Table 6.4: Design parameters of GRMC and IRMC.

	GRMC/IRMC
top mirror RoC	1 m
bottom mirrors RoC	∞
top mirror reflectivity	99.9 % (0° AOI)
bottom mirrors reflectivity	99.2 % (s-pol)
nominal cavity transmissivity	89 %
cavity length	0.584 m
FSR	513 MHz
FWHM	1.39 MHz
finesse	368

The finesse of GRMC and IRMC are measured by a cavity scan. The GRMC and IRMC cavity scans are shown in Figure 6.9 and 6.10, respectively. The measured finesse of GRMC and IRMC are 323 and 291, respectively.

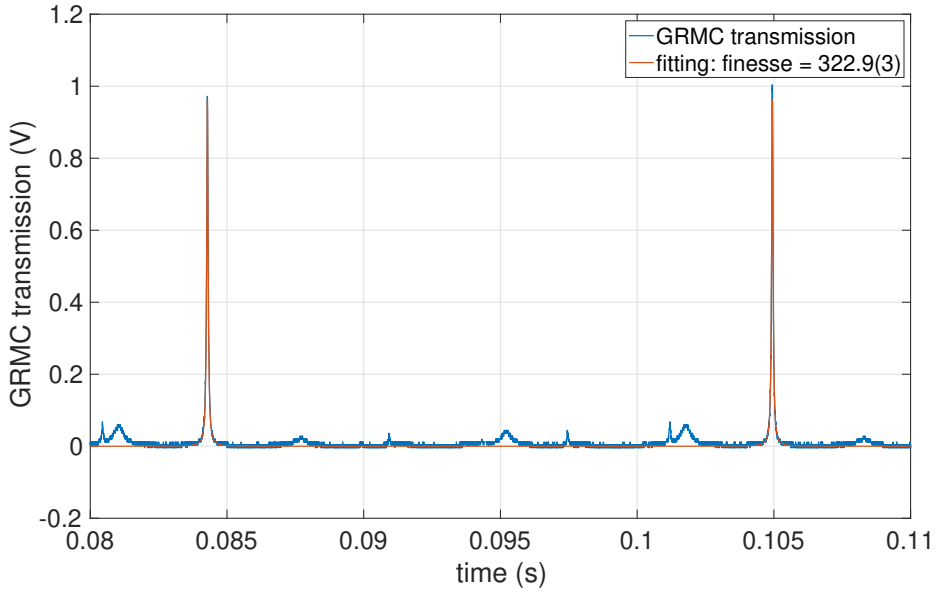

Figure 6.9: GRMC cavity scan. The blue and red lines represent the GRMC transmission curve and its fitting curve, respectively. The offset was removed from the data. The finesse value obtained from the fitting is 322.9(3) which is close to the expected value.

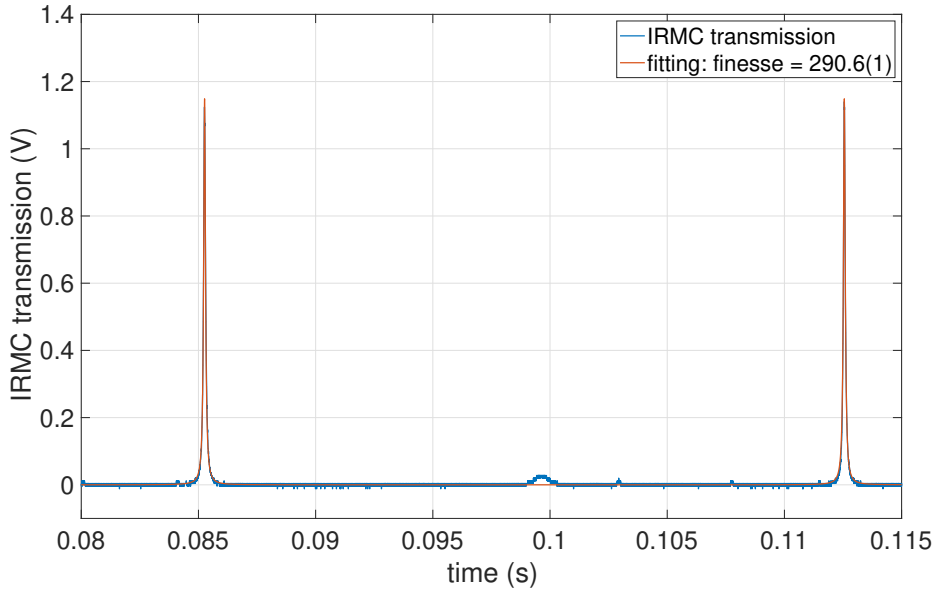

Figure 6.10: IRMC cavity scan. The blue and red lines represent the IRMC transmission curve and its fitting curve, respectively. The offset was removed from the data. The finesse value obtained from the fitting is 290.6(1) which is close to the expected value.

The open-loop transfer functions of GRMC and IRMC cavity length control are shown in Figure 6.11 and 6.12.

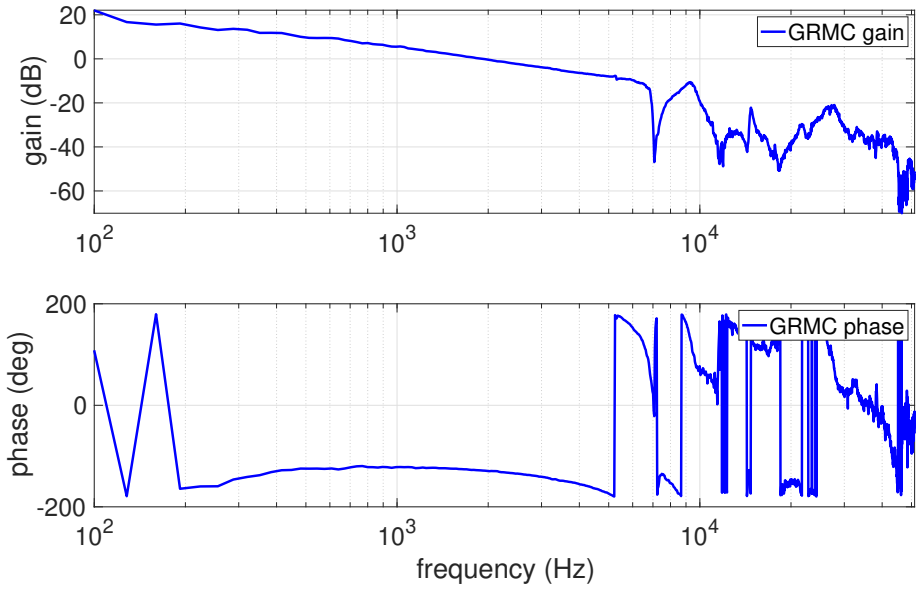

Figure 6.11: Open-loop transfer function of GRMC cavity length control. The UGF is 1.9 kHz and the phase margin is 52 deg.

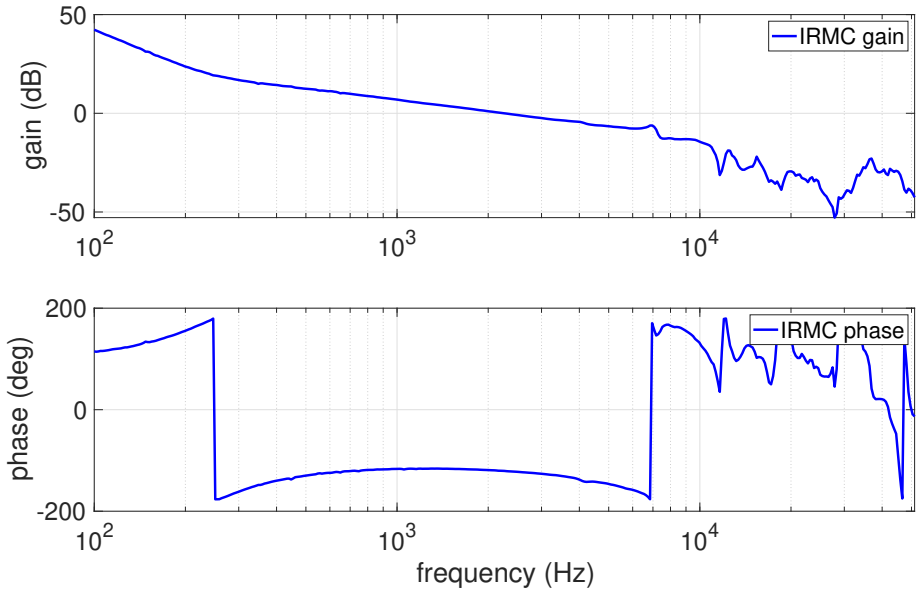

Figure 6.12: Open-loop transfer function of IRMC cavity length control. The UGF is 2.2 kHz and the phase margin is 60 deg.

6.7 Mach-Zehnder interferometer

The Mach-Zehnder interferometer (MZ) is placed on the path of the green pump after the SHG before the GRMC to stabilize the green pump power injected into the OPO. The

configuration of the MZ is shown in Figure 6.13. The open-loop transfer function of the MZ is shown in Figure 6.14.

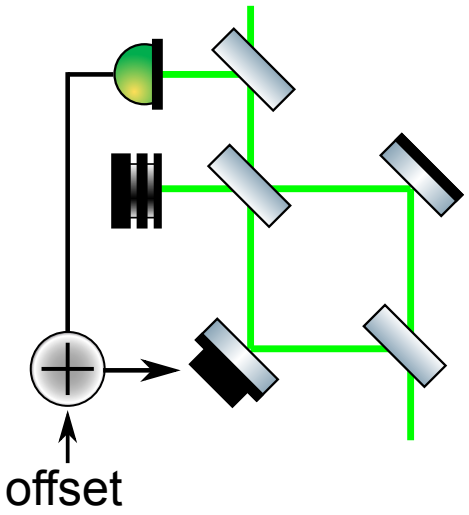

Figure 6.13: Configuration of Mach-Zehnder interferometer. One of the mirrors in the MZ has a PZT actuator for MZ control. The error signal is obtained by picking off the GRMC transmission and fed back to the PZT actuator in the MZ. The green pump power after the MZ can be controlled by changing the offset in the MZ control loop.

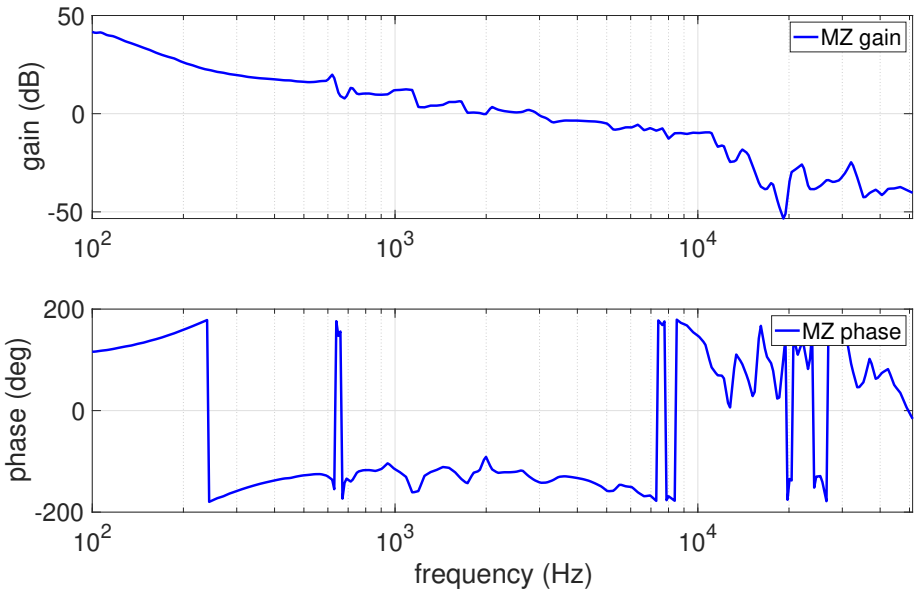

Figure 6.14: Open-loop transfer function of MZ control loop. The UGF is 2 kHz and the phase margin is 89 deg.

6.8 Optical parametric oscillator

The OPO is a cavity composed of a nonlinear crystal (PPKTP) and a meniscus mirror. The schematic cross section of OPO used in this experiment is shown in Figure 6.15. The OPO design parameters are listed in Table 6.5.

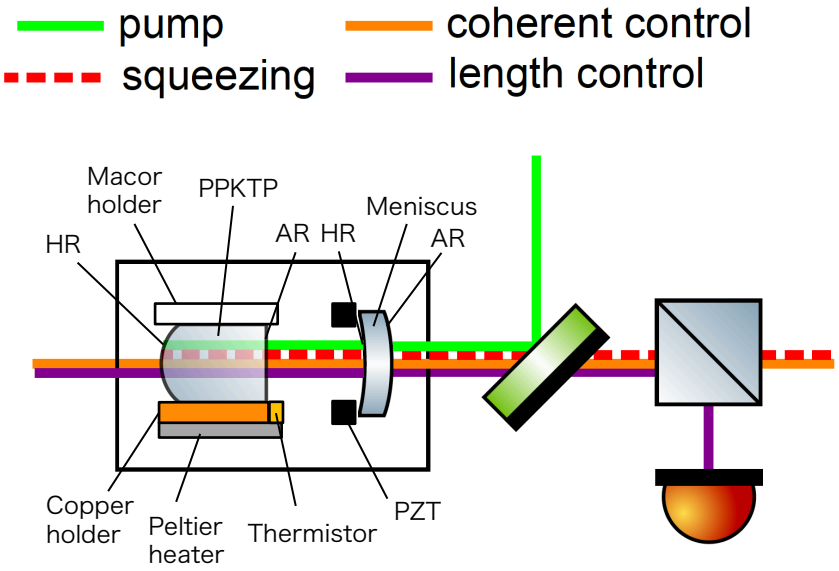

Figure 6.15: Schematic cross section of OPO. The pump, squeezing, and CC fields are s-polarized, while the length control field is p-polarized. The OPO cavity length is controlled with the PZT actuator attached to the meniscus mirror. A PDH signal of the OPO cavity is obtained by picking off the length control field with PBS at OPO transmission and fed back to the PZT actuator. The temperature of the crystal is monitored with thermistors and controlled with Peltier heaters.

Table 6.5: OPO design parameters

Cavity parameter	Value
PPKTP HR reflectivity	99.975 % (IR, GR)
PPKTP AR reflectivity	< 0.2 % (IR, GR)
Meniscus HR reflectivity	92 % (IR), 20 % (GR)
PPKTP RoC	8 mm (HR), ∞ (AR)
Meniscus RoC	25 mm (HR), 20 mm (AR)
Escape efficiency	95 %
Optical cavity length	38 mm
FSR	4 GHz
FWHM	56 MHz (IR), 1.1 GHz (GR)
Finesse	72 (IR), 3.8 (GR)

6.8.1 Escape efficiency

The OPO escape efficiency can be written as

$$\eta_{\text{esc}} = \frac{\kappa_o^a}{\kappa^a} = \frac{T}{T + L_{\text{cav}}}, \tag{6.4}$$

where $T = 8$ % is the transmissivity of the meniscus mirror and L_{cav} is the intracavity round-trip loss of the OPO (not including T). Because the PPKTP AR reflectivity is 0.2 % and the PPKTP HR transmissivity is 0.025 %, the intracavity round-trip loss of the OPO is $L_{\text{cav}} = 0.2 \cdot 2 + 0.025 = 0.425$ %. Therefore, the design escape efficiency is $\eta_{\text{esc}} = 8/(8 + 0.425) = 95$ %.

6.8.2 Finesse

To measure the IR finesse of the OPO cavity, the OPO cavity length was scanned and the IR transmission was measured as shown in Figure 6.16. The measured IR finesse of the OPO is 69.

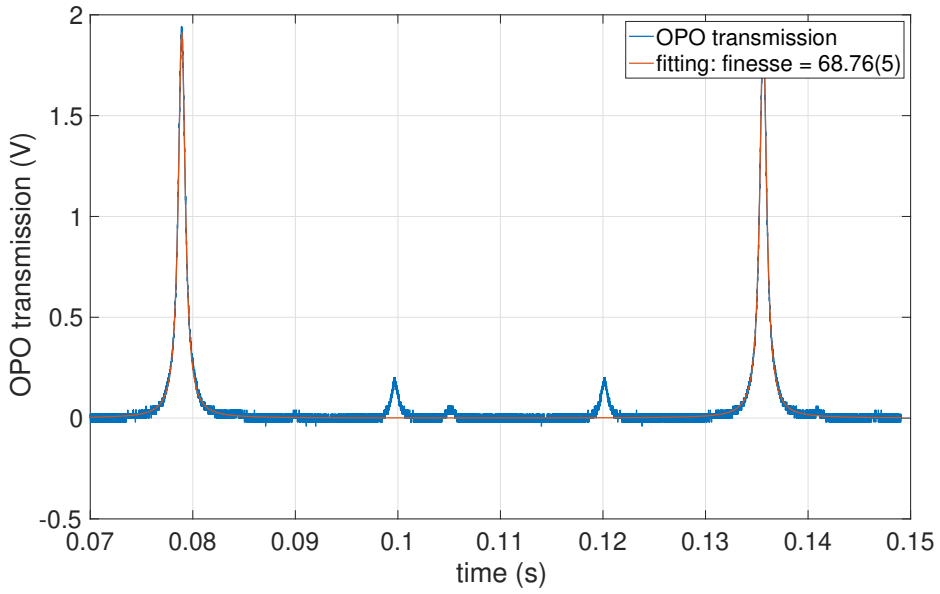

Figure 6.16: OPO cavity scan. The blue and red lines represent the OPO IR transmission curve and its fitting curve, respectively. The offset was removed from the data. The finesse value obtained from the fitting is 68.76(5), which is close to the expected value.

6.8.3 Length control

The OPO cavity length is controlled with a p-polarized laser so as not to interfere with the squeezed vacuum field, which is s-polarized. The frequency of the p-polarized laser has to be chosen such that both the p- and s-polarized beams are resonant inside the OPO. The open-loop transfer function of the OPO cavity length control is shown in Figure 6.17.

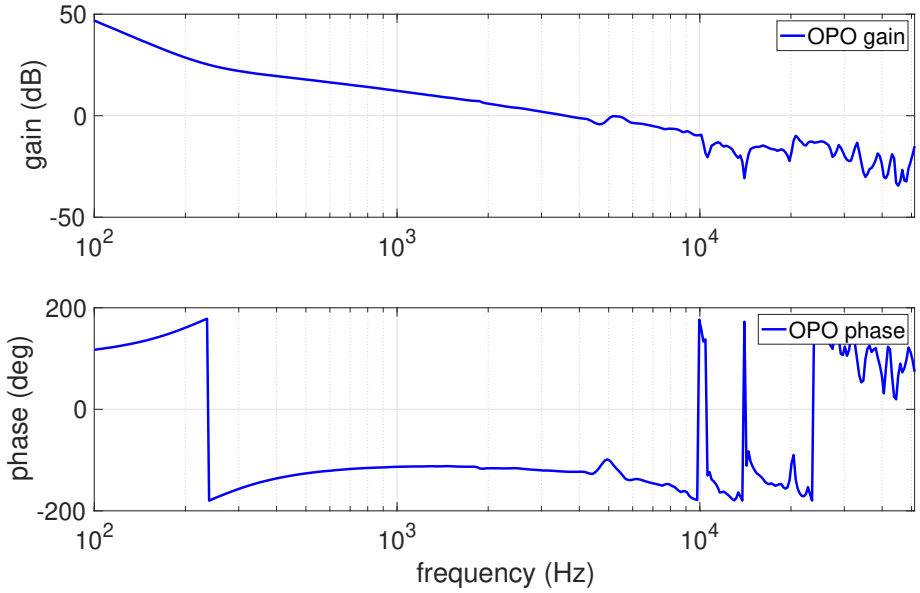

Figure 6.17: Open-loop transfer function of OPO cavity length control. The UGF is 3.6 kHz and the phase margin is 57 deg.

6.8.4 Temperature control

To find the optimal temperature for OPO, we injected the seed IR field into the OPO and measured the generated green power. The generated green power from the OPO as a function of the OPO temperature is shown in Figure 6.18. Similar to the SHG, it is not symmetric around the optimal temperature owing to the double pass configuration.

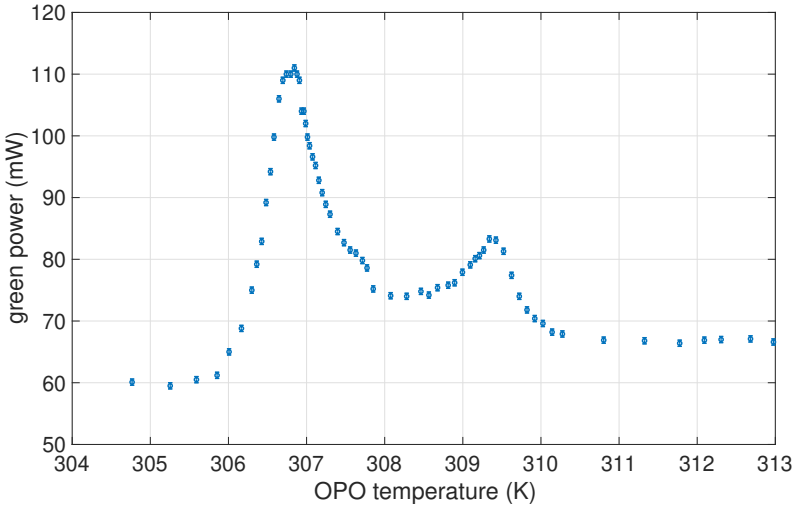

Figure 6.18: Generated green power from OPO as a function of the OPO temperature.

6.8.5 Threshold

The OPO threshold power can be measured from the parametric amplification and de-amplification of the IR seed beam injected into the OPO. The parametric amplification and de-amplification can be measured from the maximum and minimum values of the OPO transmission of the IR seed beam, while the phase of the pump field is scanned with a phase shifter, which will be explained in Section 6.11. From Equation (4.66), the parametric gain G is written as

$$G = \frac{1}{\left(1 \mp \sqrt{\frac{P_{\mathrm{pump}}}{P_{\mathrm{th}}}}\right)^2}, \tag{6.5}$$

where $-$ and $+$ correspond to the parametric amplification and deamplification, respectively.

The measured parametric (de)amplification as a function of the pump green power is shown in Figure 6.19. From this measurement, the OPO threshold power is determined as 80.6(2) mW.

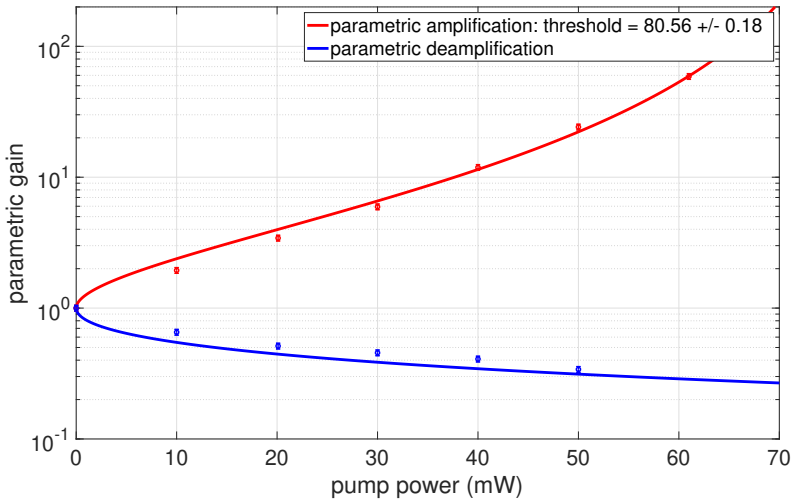

Figure 6.19: Parametric (de)amplification as a function of the pump green power. The measured parametric amplification is used for fitting.

The expected generated squeezing as a function of the pump power with $P_{\mathrm{th}} = 80.6$ mW is shown in Figure 6.20.

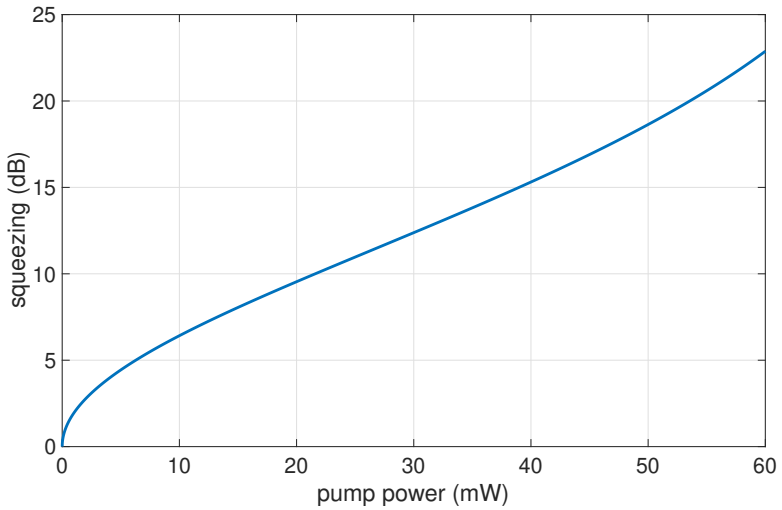

Figure 6.20: Expected generated squeezing as a function of the pump power with $P_{\mathrm{th}} = 80.6$ mW.

6.9 Alignment mode cleaner

To overlap LO and squeezed field completely, an alignment mode cleaner (AMC) was put next to the homodyne detector as shown in Figure 6.21. The specification of the AMC is the same as the IRMC. The overlapping of LO and squeezed field is achieved by aligning the LO and the seed beam to the AMC.

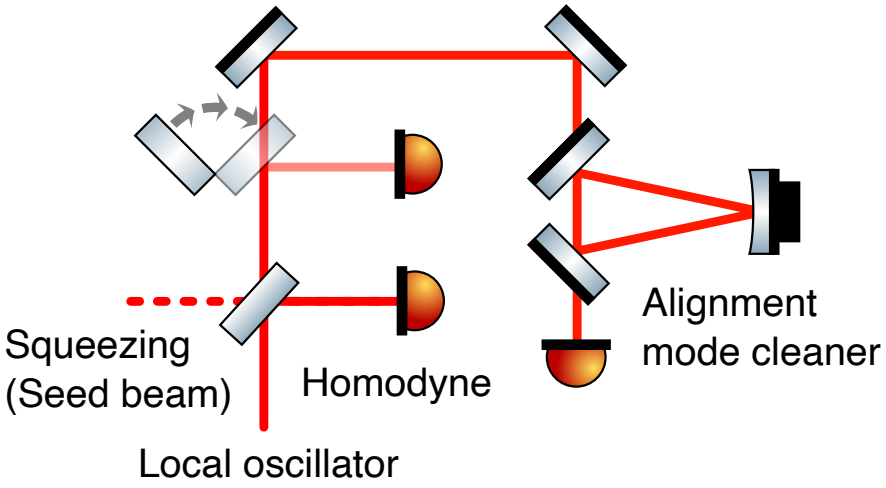

Figure 6.21: Configuration of AMC.

The nonoptimal overlapping of the LO and a squeezed field introduces losses. The overlapping of the LO and the squeezed field is called visibility, which can be determined by measuring the maximum and minimum values of the beat note between the LO and

the seed beam, as follows:

$$V_{\mathrm{exp}} = \frac{V_{\mathrm{max}} - V_{\mathrm{min}}}{V_{\mathrm{max}} + V_{\mathrm{min}}}. \tag{6.6}$$

When the LO power is P_1 and the seed beam power is P_2, the optimal visibility is

$$V_{\mathrm{opt}} = \frac{2\sqrt{P_1 P_2}}{P_1 + P_2}. \tag{6.7}$$

The optimal visibility is 1 when $P_1 = P_2$, and it is smaller than 1 otherwise. The efficiency of the visibility is $\eta_{\mathrm{vis}} = V_{\mathrm{exp}}^2 / V_{\mathrm{opt}}^2$. The typical efficiency of the visibility is $\eta_{\mathrm{vis}} = 0.98$ when the seed beam is directly sent to the homodyne detector without the filter cavity.

6.10 Homodyne detector

The homodyne detector in this experiment was designed and developed in the Albert Einstein Institute (AEI) in Germany. A picture of the homodyne detector is shown in Figure 6.22. The homodyne detector has DC and RF outputs. The DC output is proportional to the difference of photocurrents in each PD and is used for measuring squeezing. The RF output is the demodulated signal at 7 MHz and is used for the CC2 control loop.

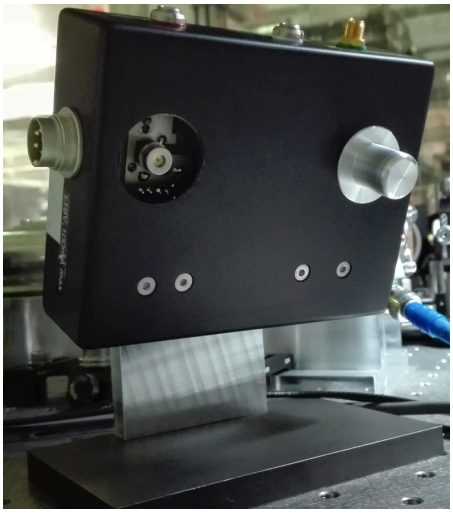

Figure 6.22: A picture of homodyne detector. The homodyne detector has two photodiodes, and one of the photodiodes is covered with an aluminum cover in the picture. The photodiodes of the homodyne detector are vertically tilted by 20° for higher quantum efficiency with photon recycling [57]. Photon recycling has not been implemented in this experiment.

The dark noise of the homodyne detector and the LO shot noise are shown in Figure 6.23. The dark noise of the homodyne detector is a noise source for squeezing and it is equivalent to the optical losses of 1.6 %. Other noise sources for squeezing are coherent control sidebands (CCSB), and the fundamental noise from the CCSB is their shot noise.

Because the LO power is 1.78 mW and the CCSB power is around 10 μW before the BS for the homodyne detector, the CCSB shot noise is more than 20 dB lower than the LO shot noise. The corresponding loss from the CCSB shot noise is less than 1 %.

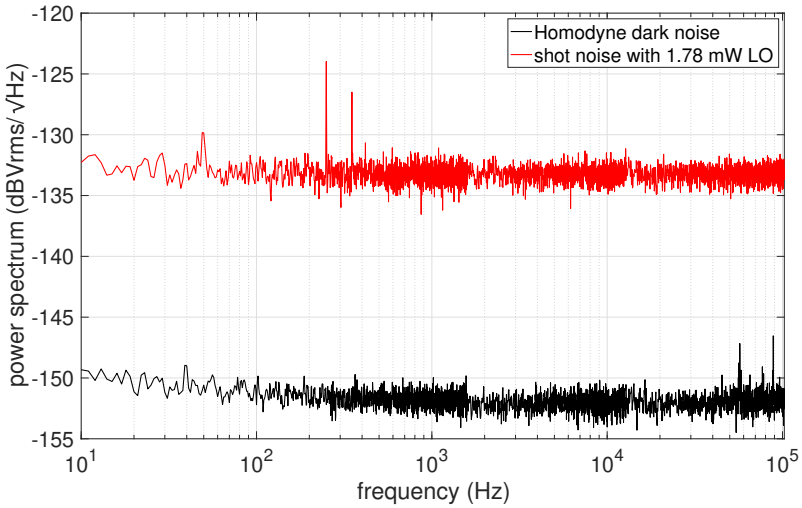

Figure 6.23: Dark noise of the homodyne detector and LO shot noise. The black line is the dark noise of the homodyne detector and the red line is the shot noise with 1.78 mW LO (0.89 mW LO in each PD). The clearance between the dark noise and shot noise with the 1.78 mW LO is about 18 dB. The loss from the dark noise is $l = V_{\text{class}}/V_{\text{vac}}^{\text{obs}} = 10^{-18/10}$ = 1.6 %.

Alignment procedure of LO and squeezed field

For common mode rejection of the classical noise of the LO, the LO power on each homodyne PD should be very well balanced. In addition, the LO and the squeezed field should be aligned accurately to the AMC for overlapping. Thus, the LO and the squeezed field should be properly aligned as follows.

1. DC balance of LO

The condition of balance for the LO field is achieved when the homodyne DC signal is 0. The homodyne DC signal for the LO is set to 0 by tweaking two lenses before the homodyne detector. If tweaking the lenses is not enough for DC balance, the BS for the homodyne detector is tweaked so that the DC signal of the homodyne detector becomes 0.

2. Alignment of LO and seed beam into AMC

The LO is aligned to the AMC with two steering mirrors before the AMC. Then, the seed beam is aligned to the AMC with steering mirrors on the path of the squeezing before the seed beam combines with the LO.

6.11 Coherent control

To control the squeezing angle, the CC laser, which has an offset frequency of 7 MHz with respect to the main laser, is injected into the OPO. CC is composed of two control loops (CC1 and CC2). The CC1 error signal is obtained at the OPO reflection by detecting the beat notes of the two sidebands (CCSB) at 14 MHz, and the CC2 error signal is obtained at the homodyne detector by detecting the beat notes of the CCSB and LO at 7 MHz. To control the green pump phase for CC1 and the LO phase for CC2, the optical paths of the green and LO fields are changed using phase shifters (see the PZT actuated mirror as shown in Figure 6.24.) located before the GRMC on the green path and before the IRMC on the LO path.

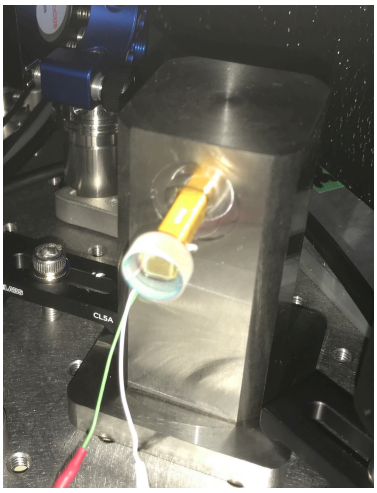

Figure 6.24: Phase shifter for coherent control. The mirror position can be adjusted by a PZT actuator which is fixed on a rigid metal mount.

The open-loop transfer functions of the CC1 and CC2 are shown in Figure 6.25 and 6.26.

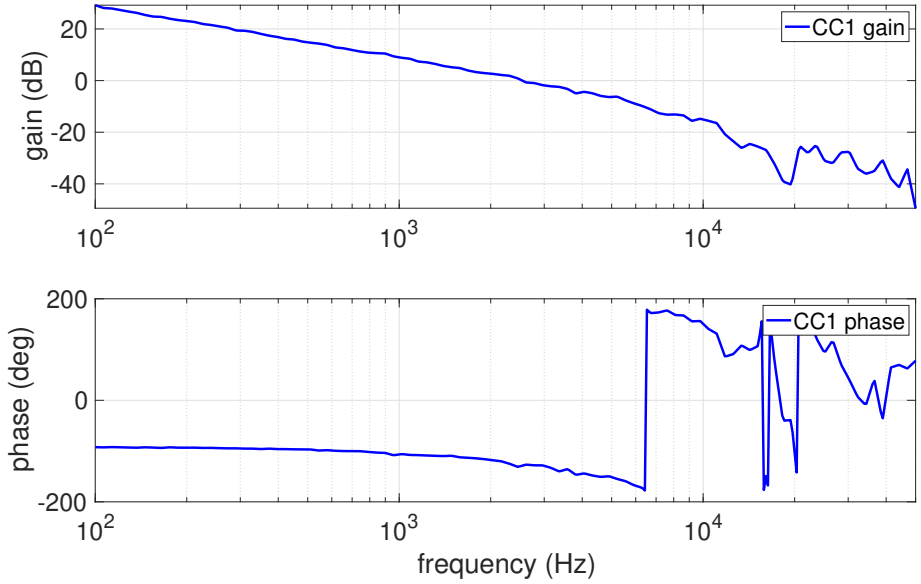

Figure 6.25: Open-loop transfer function of CC1. The UGF is 2.5 kHz and the phase margin is 51 deg.

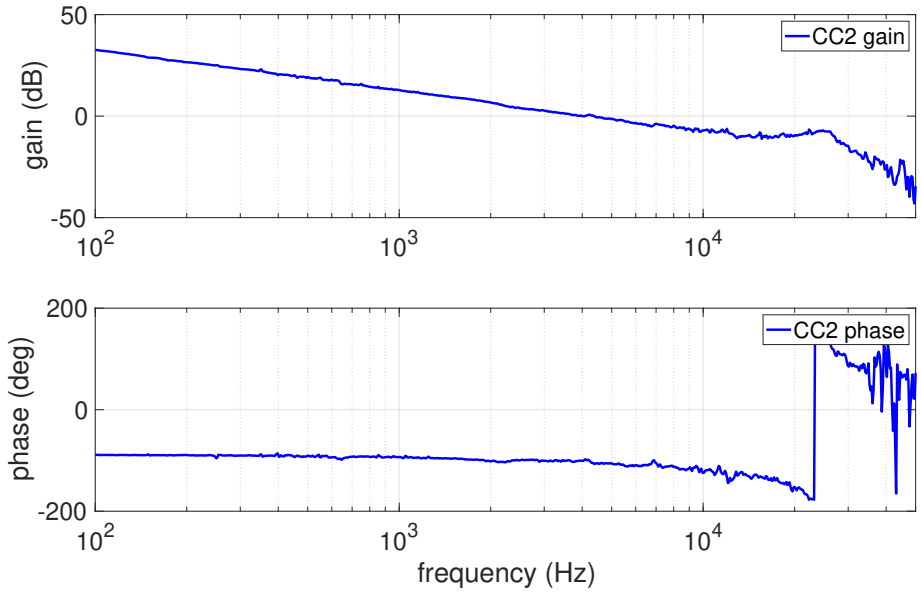

Figure 6.26: Open-loop transfer function of CC2. The UGF is 4 kHz and the the phase margin is 80 deg

The phase noise of CC1 and CC2 can be estimated from the in-loop CC1, 2 error signals. To calibrate the phase noise, the peak-to-peak values of CC1, 2 error signals were measured by scanning the phase shifter for CC1, 2. The CC1, 2 error signals can be

written as follows:

$$V_{\mathrm{err}} = \frac{V_{\mathrm{pp}}}{2} \sin\theta, \tag{6.8}$$

where V_{err} are the CC1, 2 error signals, V_{pp} are the peak-to-peak values of the CC1, 2 error signals, and θ are CC1, 2 phase noise. From this equation, the conversion factor from the CC1, 2 error signals (V) to the CC1, 2 phase noises (rad) is determined as $2/V_{\mathrm{pp}}$ when $\theta \ll 1$. The measured CC1, 2 phase noises are shown in Figure 6.27 and 6.28. The CC1, 2 in-loop rms phase noises are 84.2 and 17.3 mrad, respectively.

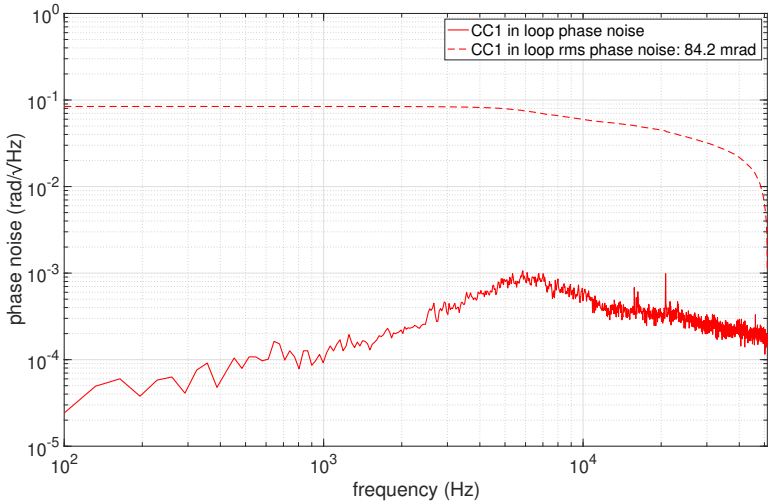

Figure 6.27: CC1 in-loop phase noise.

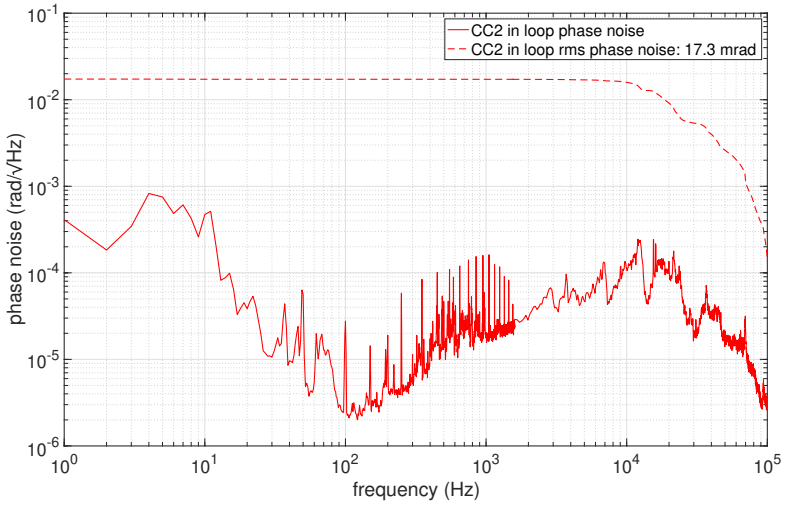

Figure 6.28: CC2 in-loop phase noise.

6.12 Squeezing spectrum

The measurement of the squeezing and anti-squeezing spectra are shown in Figure 6.29. The measured squeezing and anti-squeezing levels are 5.4 dB and 14.6 dB, respectively, between 100 Hz and 100 kHz. This measurement was performed with the pump green power of 40 mW, which is half of the OPO threshold. Around 5 dB of squeezing was achieved between 20 Hz and 100 Hz, where the frequency-dependent squeezing rotation occurs. Some peaks in the spectrum are harmonics of 50 Hz, which may originate from some electronic components.

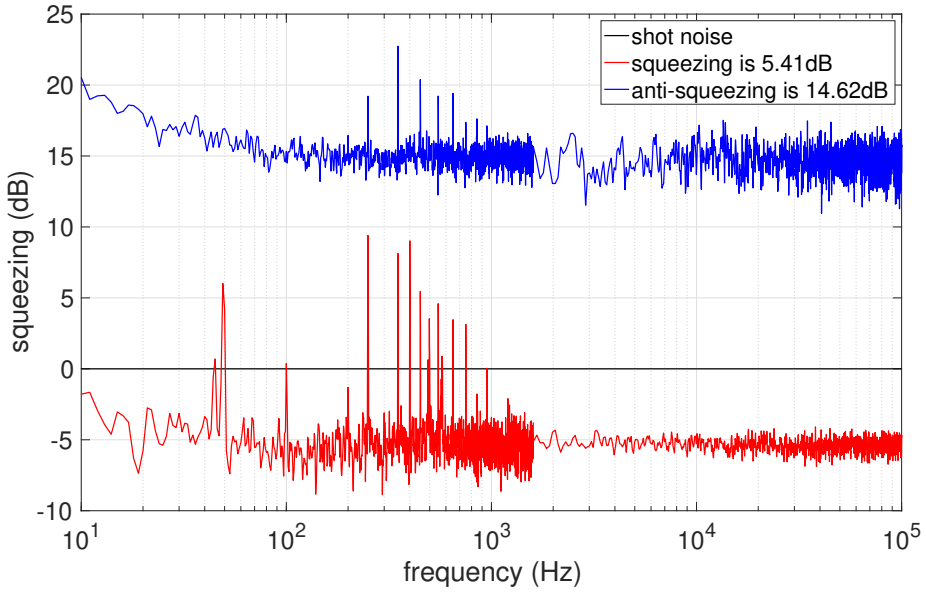

Figure 6.29: Squeezing and anti-squeezing spectrum. The measured squeezing level is 5.4 dB and anti-squeezing level is 15.6 dB.

6.13 Loss and phase noise

The loss and phase noise in the frequency-independent squeezed vacuum source can be estimated by measuring the squeezing and anti-squeezing levels with different pump green powers as shown in Figure 6.30. By fitting this data with Equation (4.115), we determine the loss as 25.2(2) % and the phase noise as 21.4(5) mrad. The current squeezing level is mainly limited by optical losses.

Loss budget

The loss budget of the frequency-independent squeezed vacuum source is summarized in Table 6.6. The classical noise listed in the Table includes dark noise of the homodyne detector (1.6 %) and shot noise of the CCSB (1 %). The unknown loss is around 9 % and the origin of the unknown loss is under investigation. However, we notice that the IR

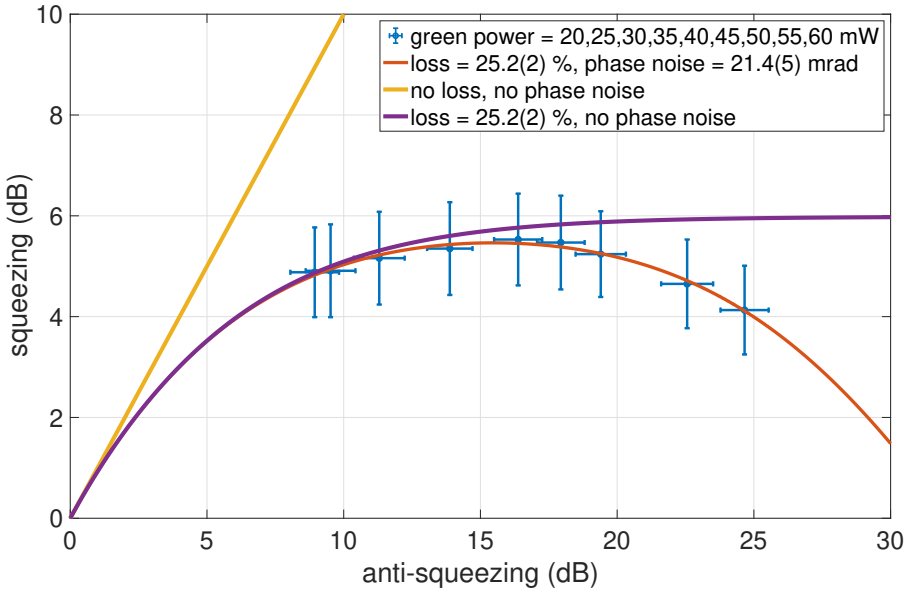

Figure 6.30: Measured squeezing and anti-squeezing levels with different pump green powers. The pump green power was increased from 20 mW to 60 mW and the anti-squeezing level increased accordingly. The error bars of the data are determined from the standard deviation of the data. From this measurement, the loss and phase noise are estimated to be 25.2(2) % and 21.4(5) mrad, respectively.

transmission from the OPO is decreased by around 7 % after propagation in free space. This reduction could be an indication of some scattering present inside the OPO.

Table 6.6: Loss budget of frequency-independent squeezed vacuum source.

loss source	loss
OPO escape efficiency (design)	5 %
mirror, lens, Faraday isolator	6 %
quantum efficiency of photodiodes	1 %
visibility	2 %
classical noise	2.6 %
unknown	8.6 %
total	25.2 %

6.14 Conclusion

To realize frequency-dependent squeezing below 100 Hz, a frequency-independent squeezed vacuum source capable of producing squeezing below 100 Hz is necessary. In this chapter, the development of the frequency-independent squeezed vacuum source was presented, and 5.4 dB of squeezing down to 20 Hz was achieved. The current squeezing level is limited by optical losses, and a part of their origin is still under investigation. It is expected that an OPO with escape efficiency as high as 99% [58] will significantly reduce the optical losses.

Chapter 7

Frequency-Dependent Squeezing with 300 m Filter Cavity

To realize frequency-dependent squeezing with rotation below 100 Hz, a 300 m-long filter cavity in the former TAMA interferometer was used. Combining the 300 m filter cavity and the squeezed vacuum source presented in the previous chapter, the first demonstration of the frequency-dependent squeezing with the rotation frequency below 100 Hz has been realized [17]. In this chapter, the experimental characterization of the 300 m filter cavity and the result of the frequency-dependent squeezing are presented. I mainly contributed to the realization and characterization of the frequency-dependent squeezing in this chapter, while the simulation and characterization of the filter cavity mirrors and initial measurement of round-trip losses were done before I joined this experiment and are reported in [62, 63, 64].

7.1 Overview

The filter cavity used in this experiment is one of the 300 m arms of the former TAMA300 interferometer [59] in National Astronomical Observatory of Japan (NAOJ). The cavity mirrors, with 10 cm in diameter, are suspended with a double pendulum system [60] placed on a vibration isolation multilayer stack [61]. Mirror motion is sensed by optical levers and controlled using coil-magnet actuators to align the cavity and to damp the mechanical resonances of the suspension [64]. To realize a squeezing rotation around 70 Hz, a storage time of about 3 ms in a filter cavity is necessary, which requires either a long or a very high-finesse cavity. As the longer cavity is more robust to length-dependent squeezing degradation sources such as cavity losses and cavity length noise, the use of several 100 m-long filter cavities have been considered for advanced detectors [52, 62]. The squeezing rotation frequency by the filter cavity depends on the cavity bandwidth, which is inversely proportional to its length and finesse. Given the 300 m length of the cavity, the finesse should be 4360 at a wavelength of 1064 nm to provide the squeeze angle rotation at approximately 75 Hz, which corresponds to an optimal quantum noise reduction for KAGRA.

Because the filter cavity losses are one of the major limitations to squeezing, as discussed in Section 5.6, the requirements of surface quality of the filter cavity mirrors were firstly determined by numerical simulations [62]. After the cavity assembly, the round-trip losses were measured as 50-90 ppm, which is consistent with the requirements [63]. The filter cavity parameters are listed in Table 7.1.

Table 7.1: Summary of the filter cavity parameters. The mirror transmissivity and radius of curvature have been measured at the Laboratoire des Matériaux Avancés (LMA). It should be noted that the round-trip losses include the end mirror transmissivity [63].

Cavity parameter	Value
Length	300 m
Mirror diameter	10 cm
Input mirror radius of curvature	438 m
End mirror radius of curvature	445 m
Input mirror transmissivity (1064 nm)	0.136%
End mirror transmissivity (1064 nm)	3.9 ppm
Finesse (1064 nm)	4360
Input mirror transmissivity (532 nm)	0.7%
End mirror transmissivity (532 nm)	2.9%
Finesse (532 nm)	172
Beam diameter at waist	1.68 cm
Beam diameter at the mirrors	2.01 cm

7.2 Experimental setup

The experimental setup used to achieve the frequency-dependent squeezing is shown in Figure 7.1. It is composed of two parts: a frequency-independent squeezed vacuum source and a filter cavity whose mirrors are suspended with a double pendulum for seismic noise isolation. These two parts are connected through an in-vacuum injection system, which includes two suspended mirrors.

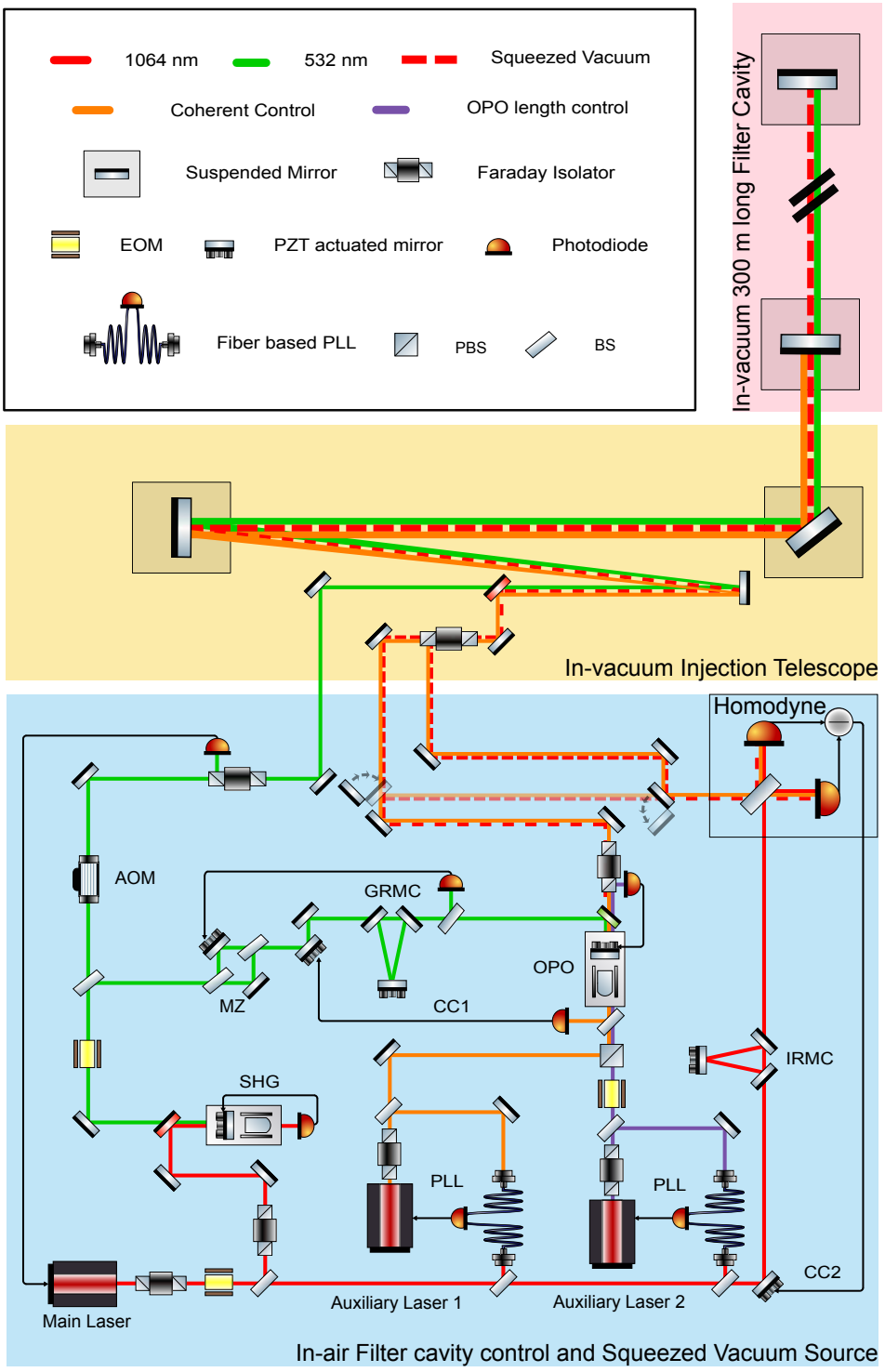

Figure 7.1: Schematic view of the experimental setup. The squeezed vacuum field is generated by the OPO and injected into the filter cavity using an in-vacuum injection telescope. The frequency-dependent squeezed vacuum field from the filter cavity is reflected by the in-vacuum Faraday isolator and measured by the homodyne detector. The green field generated by the SHG is used to pump the OPO and to control the filter cavity.

7.3 300 m filter cavity

To realize frequency-dependent squeezing with a rotation frequency around 75 Hz, a crucial parameter is the filter cavity half bandwidth (or filter cavity finesse). As we discussed in Section 5.5, the filter cavity losses and length noise, which are the main degradation sources for squeezing, are also important parameters. In this section, the characterization of the 300 m filter cavity, such as filter cavity length noise, finesse, and round-trip losses, is presented.

7.3.1 Green lock

The length of the filter cavity is controlled using an auxiliary green field that is picked off the SHG output. The cavity finesse for the auxiliary green field is about 25 times smaller than that for the infrared field. The green field is superposed to the squeezed field at an in-vacuum dichroic mirror, as shown in Figure 7.1. The PDH signal is obtained from the reflected green field, and the correction signal is sent to the PZT actuator of the main laser to act on its frequency. An acousto-optic modulator (AOM) is placed on the green field path before injection into the filter cavity. By driving the AOM at different frequencies, it is possible to control the detuning of the carrier with respect to the cavity resonance by changing the relative frequencies of the green and squeezed fields.

Table 7.2 and 7.3 show the zeros, poles, and frequency dependence of the open-loop transfer function for the green lock.

Table 7.2: Zeros and poles of open-loop transfer function for green lock.

zeros	Q	quantity	origin
145 Hz	simple	1	servo
2.68 kHz	simple	4	servo
88 kHz	simple	1	servo
poles	Q	quantity	origin
0.0001 Hz	simple	5	servo
1.45 kHz	simple	1	cavity
90 kHz	simple	1	piezo
142 kHz	0.78	2	servo
329 kHz	simple	1	servo
380 kHz	simple	1	servo
658 kHz	simple	1	servo
675 kHz	simple	1	servo

The measured open-loop transfer function of the green lock for the filter cavity is shown in Figure 7.2.

Table 7.3: Frequency dependence of the open-loop transfer function for green lock.

frequency	frequency dependence of OLTF
DC $< f <$ 145 Hz	f^{-5}
145 Hz $< f <$ 1.45 kHz	f^{-4}
1.45 kHz $< f <$ 2.68 kHz	f^{-5}
2.68 kHz $< f <$ 88 kHz	f^{-1}

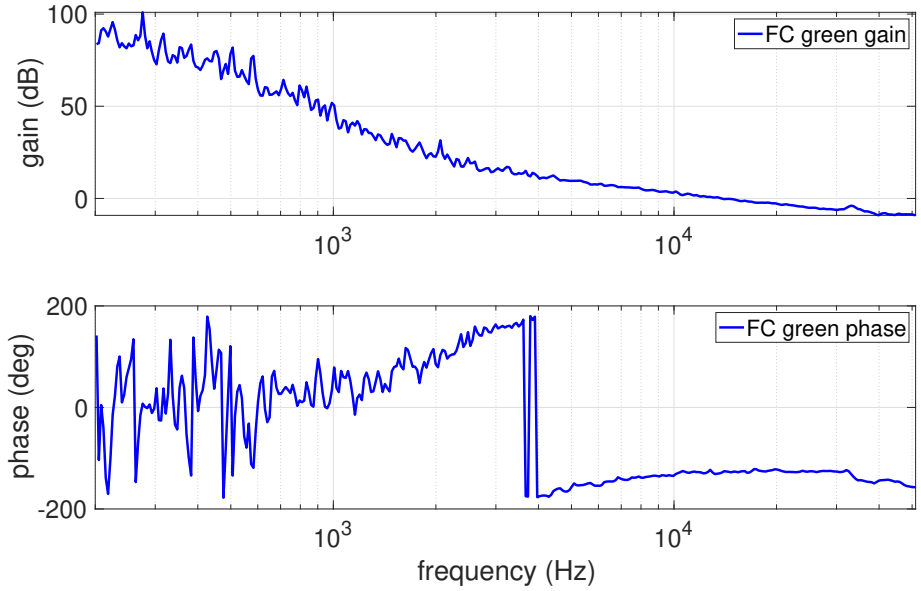

Figure 7.2: Open-loop transfer function of the green lock for the filter cavity. The UGF is 14 kHz and the phase margin is 54 deg.

7.3.2 Locking accuracy

Locking accuracy of green field

The locking accuracy of the green field is evaluated using the in-loop green PDH signal. The calibration of the green PDH signal is achieved by injecting a line at 28 kHz, which is above the UGF of the green lock $\sim$ 14 kHz, and therefore, the effect of the noise suppression by the control loop is small. The line was injected into the PZT actuator of the main laser and measured at the PZT monitor channel and the PDH signal, which are respectively before and after the servo for the green lock. By comparing the two line amplitudes, the calibration factor from the error signal to the locking accuracy (Hz/V) can be obtained. The amplitude of the 28 kHz line in Hz is

$$S_{\mathrm{Hz}} = V_{\mathrm{in}}\ (\mathrm{V_{rms}}) \cdot \sqrt{2} \cdot 100 \cdot 2 \cdot 10^6\ (\mathrm{Hz/V}) = 5827\ (\mathrm{Hz}) \tag{7.1}$$

where $V_{\mathrm{in}} = 20.6 \cdot 10^{-6}$ $\mathrm{V_{rms}}$ has been measured at the PZT monitor channel and the factor of $\sqrt{2}$ is the conversion factor from $\mathrm{V_{rms}}$ to V. The factor of 100 is the attenuation

factor of the PZT monitor channel. 10^6 Hz/V is the gain of the PZT actuator of the main laser and the factor of 2 represents the frequency doubling in the SHG.

Considering the cavity pole of the filter cavity and the open-loop transfer function of the green lock, the injected line in the error signal is

$$V_{\mathrm{err}} = \frac{1}{|1 + G_{\mathrm{GR}}(f)|} \cdot \frac{1}{K\ (\mathrm{Hz/V})} \cdot \frac{S_{\mathrm{Hz}}}{\sqrt{1 + \left(\frac{f}{f_p}\right)^2}} \tag{7.2}$$

where $V_{\mathrm{err}} = 1.3\ \mathrm{V_{rms}} = \sqrt{2} \cdot 1.3$ V is the measured amplitude of the injected line in the error signal, K is the calibration factor (Hz/V), G_{GR} is the open-loop transfer function of the green lock at the frequency of the injected line, $f = 28$ kHz is the frequency of the injected line, and $f_p = 1.45$ kHz is the cavity pole for the green field. From Figure 7.2, the gain and phase of G_{GR} at 28 kHz are -5.8 dB and -125 deg, respectively. From Equation (7.1) and (7.2), the calibration factor is $K = 2.0 \times 10^2$ Hz/V.

The measured green locking accuracy is shown in Figure 7.3. The green locking accuracy (rms) is 20.3 Hz.

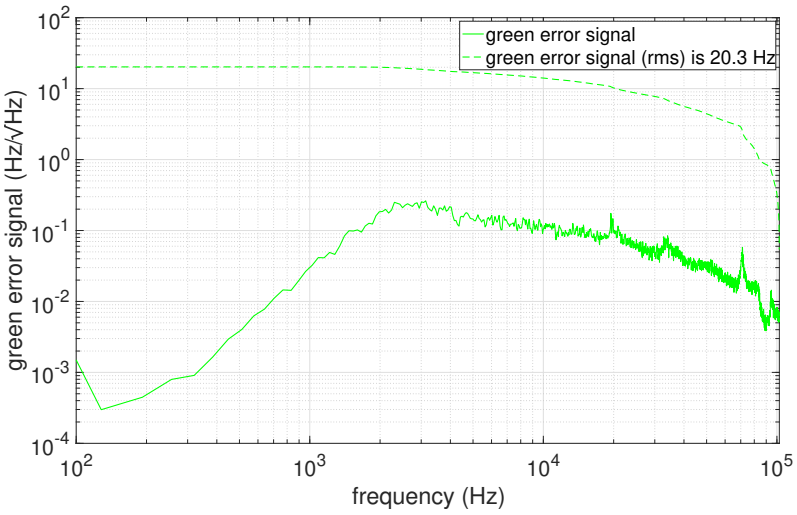

Figure 7.3: Locking accuracy of green field with green lock. The spectrum of the in-loop green PDH signal is calibrated in units of Hz/$\sqrt{\mathrm{Hz}}$ using the calibration factor of $K = 2.0 \times 10^2$ Hz/V. The green locking accuracy (rms) is 20.3 Hz.

Locking accuracy of IR field

The locking accuracy of the IR field is a significant parameter because it represents the filter cavity length noise for squeezing. To evaluate the locking accuracy of the IR field, the IR seed beam was injected into the filter cavity and the reflected seed beam was detected using an auxiliary RFPD. The reflected IR signal was demodulated at 15.2 MHz to obtain the IR PDH signal. To calibrate the IR PDH signal, the filter cavity was locked with the green field and the frequency of the AOM was scanned around the IR resonance. The

calibration factor from the IR PDH signal to frequency (Hz/V) is

$$c_{\mathrm{PDH}} = \frac{s_{\mathrm{AOM}} t_{\mathrm{pp}}}{2V_{\mathrm{pp}}} \tag{7.3}$$

where s_{AOM} is the scan speed of the AOM for IR (Hz/s), V_{pp} is the peak-to-peak value of the IR PDH signal (V), and t_{pp} is the time difference of the peak-to-peak of IR PDH signal (s). It should be noted that the scan speed of the AOM for IR is half of that for the green field. The factor of 2 in Equation (7.3) is used because the slope of the error signal around the resonance is as about twice as the slope of the peak-to-peak value.

To measure the locking accuracy, the IR seed field was set on resonance by adjusting the AOM driving frequency and the IR PDH signal was measured. The measured IR error signal is shown in Figure 7.4. The IR locking accuracy with green lock (rms) is 3.2 Hz. The conversion from frequency noise δf to length noise δL in the 300 m cavity is

$$\frac{\delta L}{\delta f} = \frac{L_{\mathrm{fc}}}{f_0} = \frac{L_{\mathrm{fc}}\lambda}{c} = 1.06 \text{ pm/Hz}. \tag{7.4}$$

Therefore, the frequency noise of 3.2 Hz corresponds to the filter cavity length noise of 3.4 pm, while the target filter cavity length noise is 1 pm. The IR locking accuracy below 10 Hz is dominated by the filter cavity length noise and it is dominated by the laser frequency or the phase noise above 10 Hz. Although the IR locking accuracy (rms) above 10 Hz is $\sim$ 1 Hz, the filter cavity length noise below 10 Hz contributes to the IR locking accuracy of $\sim$ 2 Hz. This means that the green lock is not enough to stabilize the IR locking accuracy below 1 pm.

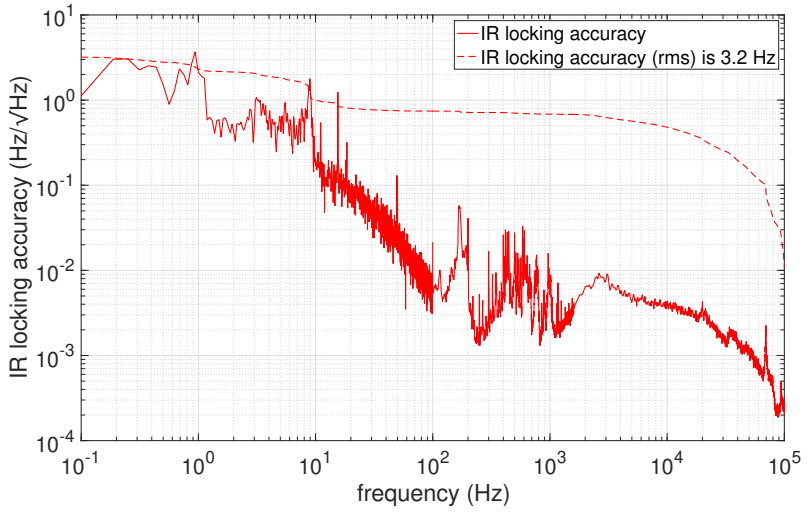

Figure 7.4: IR locking accuracy with the green lock. The IR locking accuracy with the green lock (rms) is 3.2 Hz, which corresponds to the filter cavity length noise of 3.4 pm. It should be noted that this is an out-of-loop estimation of the IR locking accuracy.

7.3.3 Finesse

The finesse of the filter cavity was estimated by measuring the decay time of the cavity. The filter cavity was set on resonance for an IR seed field and, by driving the AOM, it was suddenly driven out of resonance. The IR transmission was monitored during this process. The ringdown measurement is shown in Figure 7.5. By fitting the ringdown measurement with Equation (3.28), the decay time is determined as $\tau = 2.680(1)$ ms. Using Equation (3.29), the finesse is estimated to be $\mathcal{F} = \pi f_{\mathrm{FSR}} \tau = 4210(2)$, which is close to the design value of 4360.

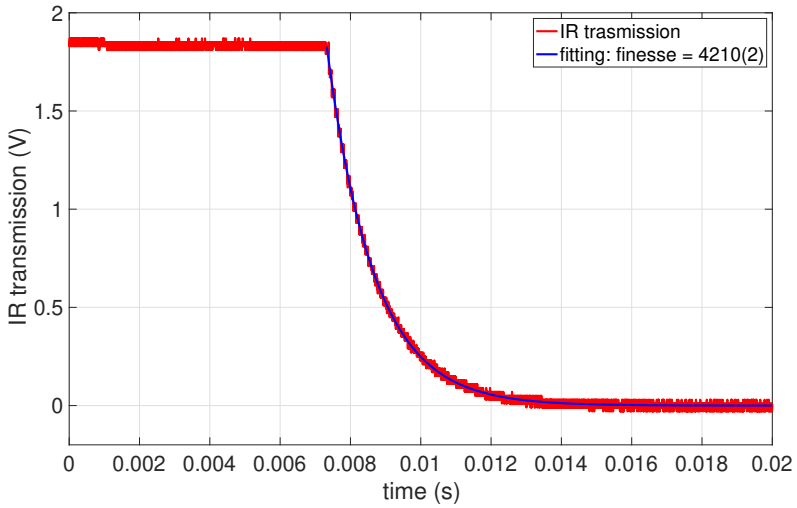

Figure 7.5: Finesse measurement with ringdown. The measured decay time is $\tau = 2.680(1)$ ms, and the corresponding finesse is 4210(2). The offset was removed from the data.

7.3.4 Round-trip losses

The round-trip losses of the filter cavity can be measured from the ratio of the IR reflected power from the cavity when it is on/off resonance. From Equation (3.18), this ratio can be written as follows:

$$R_{\mathrm{cav}} = \frac{P_{\mathrm{res}}}{P_{\mathrm{in}}} = \left[\frac{r_{\mathrm{I}} - r_{\mathrm{E}}}{1 - r_{\mathrm{I}} r_{\mathrm{E}}}\right]^2 \simeq \left[\frac{r_{\mathrm{I}} - \sqrt{1 - \Lambda_{\mathrm{rt}}^2}}{1 - r_{\mathrm{I}}\sqrt{1 - \Lambda_{\mathrm{rt}}^2}}\right]^2, \tag{7.5}$$

where P_{res} is the IR reflected power on resonance and P_{in} is the input power, which can be measured from the IR reflected power when it is off resonance. Here it is assumed that

$$r_{\mathrm{E}} = \sqrt{1 - T_{\mathrm{E}}} \simeq \sqrt{1 - \Lambda_{\mathrm{rt}}^2}. \tag{7.6}$$

This means that the transmissivity of the end mirror is included in the round-trip losses.

By solving Equation (7.5), we obtain the following:

$$\Lambda_{\mathrm{rt}}^2 = \frac{T_{\mathrm{I}}(1 - R_{\mathrm{cav}})}{(\sqrt{R_{\mathrm{cav}}} r_{\mathrm{I}} + 1)^2}. \tag{7.7}$$

The first round-trip loss measurement was done in 2018 before I joined this experiment. The round-trip losses measured at that time were 50-90 ppm [63]. After I joined this experiment, the round-trip losses were measured again in 2020. The result is shown in Table 7.4. The result indicates that the round-trip losses are a bit larger than before. One possible explanation is that the filter cavity mirrors might be contaminated becase the vacuum chamber was opened several times and no cleaning was done during the last two years. We also measured frequency-dependent squeezing during a similar period in 2020, and therefore, we estimate that the round-trip losses are 120(30) ppm during the frequency-dependent squeezing measurement.

Table 7.4: Measurement of round-trip losses in 2020.

Measurement date	Round-trip losses
2020.01.23	148 ppm
2020.02.07	122 ppm
2020.02.10	95 ppm

7.4 Loss and phase noise outside the filter cavity

In addition to the filter cavity losses and length noise, loss and phase noise outside the filter cavity are also the main squeezing degradation sources. The loss and phase noise outside the filter cavity was determined by measuring the squeezing and anti-squeezing levels with different pump green powers in a frequency region where the squeezing is off resonance of the filter cavity. Under this condition, the squeezed field sees the filter cavity as a perfect mirror, and therefore, the loss and phase noise outside the filter cavity can be measured. The result is shown in Figure 7.6. From this measurement, we find that the loss and phase noise outside the filter cavity are 40(1) % and 30(5) mrad, respectively. The optical loss is increased by 15 % as compared with that without the filter cavity, as shown in Figure 6.30. The increase in the optical loss is mainly due to the in-vacuum Faraday isolator with $\sim$ 15 % loss for double pass.

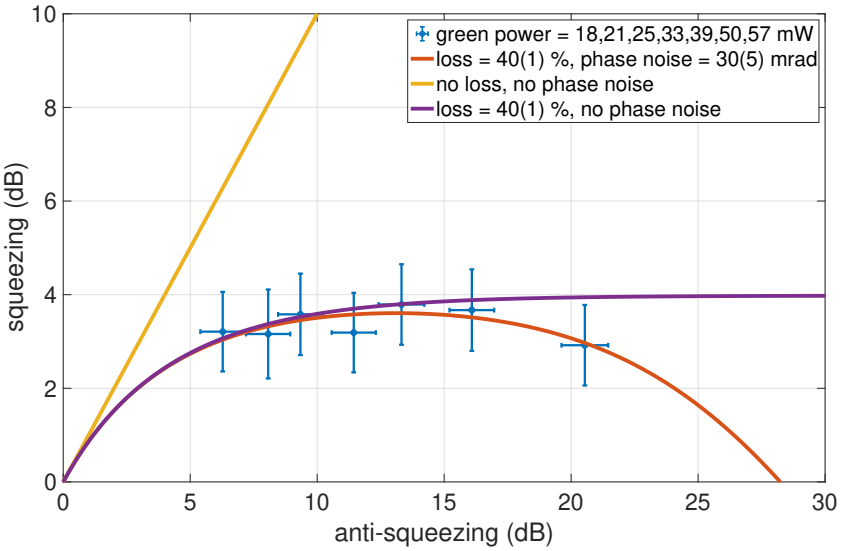

Figure 7.6: Squeezing and anti-squeezing levels with different pump green powers. The pump green power was increased from 18 mW to 57 mW and the anti-squeezing level increased accordingly. The error bars of the data are determined from the standard deviation of the data. From this measurement, the loss and phase noise outside the filter cavity are estimated to be 40(1) % and 30(5) mrad, respectively.

7.5 Frequency-dependent squeezing measurement

The measurement of the frequency-dependent squeezing was done by measuring the quantum noise of the LO at the homodyne detector, changing the relative phase of the LO and the squeezing angle (homodyne angle). The theoretical frequency-dependent squeezing spectra for different homodyne angles are shown in Figure 7.7.

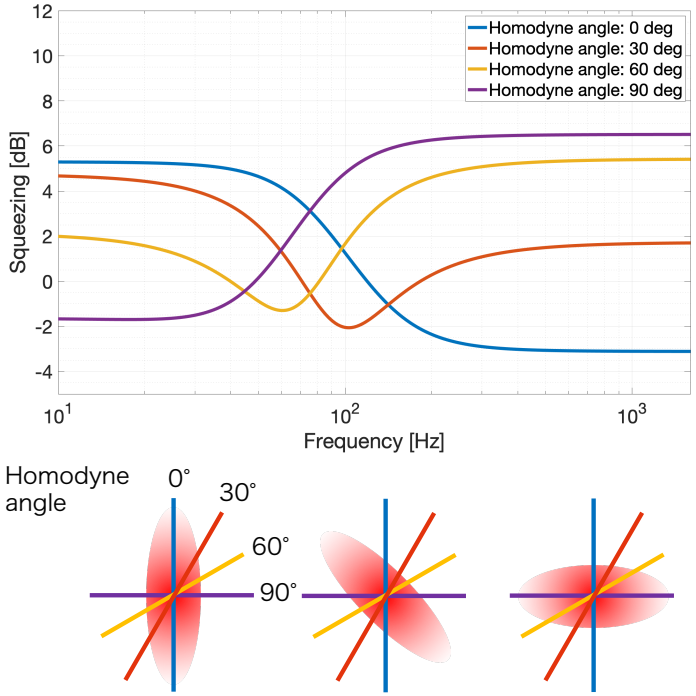

Figure 7.7: Theoretical quantum noise spectra of the frequency-dependent squeezing for different homodyne angles. The degradation parameters in Table 7.5 are assumed.

The measured frequency-dependent squeezing spectra for different homodyne angles are shown in Figure 7.8. The measured squeezing level was 3.4 ± 0.4 dB above the rotation frequency and $\sim$1 dB below the rotation frequency. The measured spectra are fitted with a theoretical model that uses the squeezing degradation parameters listed in Table 7.5. These parameters are the same for every curve, while the homodyne angle and the cavity detuning are fitted for each curve. The average of the fitted cavity detuning in Figure 7.8 was about 63 Hz, which corresponds to the squeezing rotation frequency of about $63 \times \sqrt{2} = 90$ Hz.

Although it is possible to operate the cavity at the optimal detuning, the detuning in Figure 7.8 was set to have a squeezing rotation at a slightly higher frequency than the optimal one (about 90 Hz instead of 75 Hz) because the spectrum is dominated by the backscattering noise below $\sim$70 Hz. The backscattering noise comes from a leaked LO which is reflected by the filter cavity and injected into the homodyne detector. This backscattering noise depends on the mirror motion and alignment condition of the filter cavity.

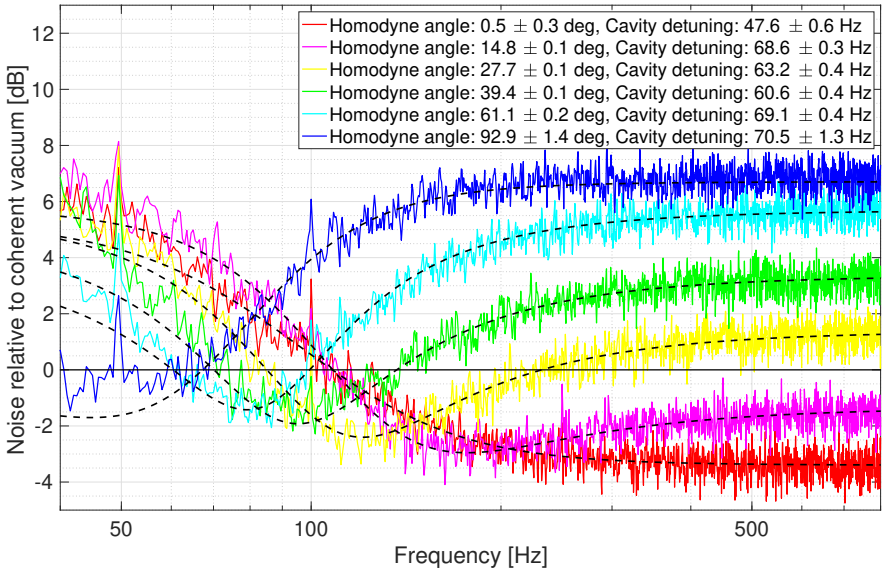

Figure 7.8: Measured noise spectra of the frequency-dependent squeezing for different homodyne angles. The measured squeezing level was 3.4 ± 0.4 dB above the rotation frequency and $\sim$1 dB below the rotation frequency. Each curve above 70 Hz has been fitted with a theoretical model assuming the degradation parameters listed in Table 7.5, and the homodyne angle and the cavity detuning are extracted from the fitting. Each spectrum has a resolution of 0.5 Hz and is averaged 100 times, leading to an acquisition time of 200 s.

Table 7.5: Current and target squeezing degradation parameters.

Parameter	Current	Target
Filter cavity losses	120 ± 30 ppm	80 ppm
Propagation losses	36 % ± 1%	10 %
Mode-mismatch squeezer-filter cavity	6 % ± 1%	2 %
Mode-mismatch squeezer-local oscillator	2 % ± 1%	5 %
Frequency-independent phase noise (rms)	30 ± 5 mrad	30 mrad
Filter cavity length noise (rms)	3 ± 0.5 pm	1 pm
Generated squeezing	8.3 ± 0.1 dB	9 dB

To check the reproducibility of the frequency-dependent squeezing spectra, the noise spectra for homodyne angles around 90 deg were measured as shown in Figure 7.9. Although the noise level below $\sim$70 Hz fluctuated due to the backscattering noise, each spectrum has a rotation frequency around 100 Hz and agrees with the theoretical curve above 70 Hz.

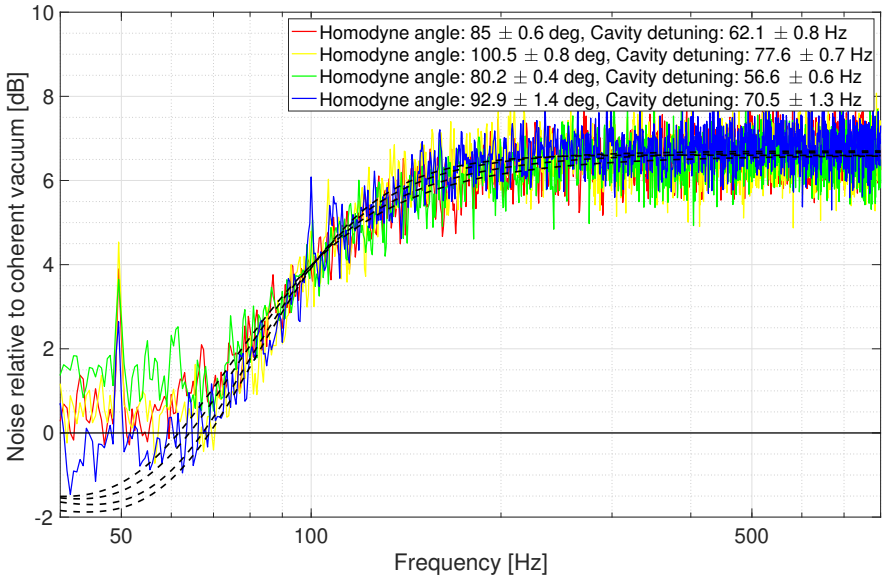

Figure 7.9: Measured noise spectra of the frequency-dependent squeezing for homodyne angles around 90 deg. The measured noise relative to the coherent vacuum were around ±1.5 dB below the rotation frequency due to the backscattering noise. Each curve above 70 Hz has been fitted with a theoretical model assuming the degradation parameters listed in Table 7.5, and the homodyne angle and the cavity detuning are extracted from the fitting. Each spectrum has a resolution of 0.5 Hz and is averaged 100 times, leading to an acquisition time of 200 s.

7.6 Discussion

The achievable quantum noise reduction in GW detectors with the filter cavity described in this chapter is shown in Figure 7.10. Here, a squeezing angle rotation at 75 Hz, which is the optimal frequency for KAGRA, is assumed. This plot also assumes a lossless matching with the interferometer. Because the loss values used in Figure 7.10 are larger than those for advanced detectors in the next observation runs (including the losses due to a non-optimal coupling between the squeezer and the interferometer), the quantum noise reduction expected in advanced detectors will be higher than that shown in Figure 7.10 [65, 66].

The drift of the alignment condition of the suspended mirrors, such as cavity mirrors and mirrors used to inject the squeezing into the cavity, limits the mode matching between the squeezed field and the cavity to ∼94 %. Therefore, the auto alignment of the filter cavity is necessary to improve the mode matching.

Propagation losses for the squeezed field are dominated by the low OPO escape efficiency (∼90 %) as well as the in-vacuum Faraday isolator loss (∼15 % for double pass). Both components will be replaced with lower loss components. In particular, Faraday isolators with losses below 1% [67] and the OPO with an escape efficiency as high as 99 % [58] have been realized. It is expected that the integration of a Faraday isolator with better

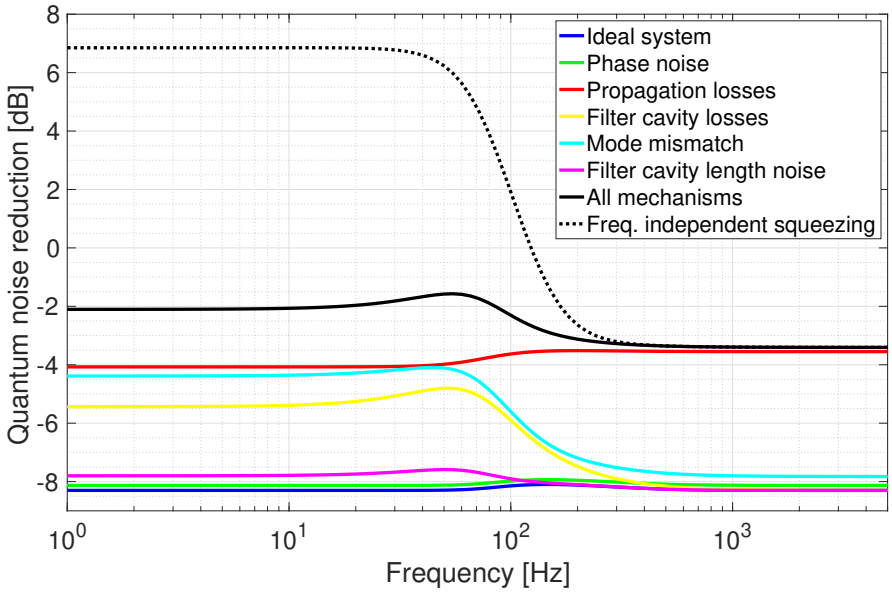

Figure 7.10: Estimated degradation budget for the frequency-dependent squeezing source. The squeezing degradation parameters used in this plot are listed in Table 7.5. The solid black curve represents the expected quantum noise reduction for a GW detector such as KAGRA. The dashed black curve represents the case for a frequency-independent squeezing (with the same squeezing level as the frequency-dependent case). As expected, quantum noise is significantly reduced at low frequencies owing to frequency-dependent squeezing as compared with frequency-independent squeezing.

isolation factor and a better vibration isolation system will also reduce the backscattering noise to below ∼50 Hz.

Because the filter cavity was controlled and aligned with respect to the auxiliary green field, any relative misalignment of the squeezed field with respect to the green field will not be corrected. In fact, a slow drift of the squeezed field axis with respect to the green one was observed. This drift limits the long-term operation of the filter cavity. A correlation was also observed between the alignment condition of the squeezed field and its detuning with respect to the cavity resonance. This relation is suspected to be the cause of the cavity detuning fluctuation observed in Figure 7.8. The mechanisms that couple the alignment fluctuation with the detuning fluctuation are still under investigation. To solve these problems, I proposed a new control scheme which uses the already present coherent control field for both length and alignment control [18]. This scheme will be explained in Chapter 8. A similar scheme, using an additional field at near the squeezing frequency, has been demonstrated for the length control of a 16 m filter cavity at MIT [68].

7.7 Conclusion

In this chapter, the characterization of the 300 m filter cavity and the first demonstration of frequency-dependent squeezing with the squeezing angle rotation below 100 Hz were

reported.

Regarding the characterization of the 300 m filter cavity, the squeezing degradation sources were characterized and the method to reduce them was discussed. In particular, it is revealed that the conventional control scheme for the filter cavity with an auxiliary green field is not enough to stabilize the locking accuracy of the filter cavity.

Regarding the demonstration of frequency-dependent squeezing, the rotation frequency of the squeezing angle was below 100 Hz, which is necessary for broadband quantum noise reduction in current GW detectors. It is indicated that the frequency-dependent squeezing source reported in this chapter can reduce the quantum noise in GW detectors at all frequencies. Because filter cavities whose length is comparable with 300 m, as in our demonstration, are planned to be installed soon in Advanced LIGO, Advanced Virgo, and KAGRA, the results presented in this chapter play a key role in realizing this technology in advanced detectors.

This result is not only a step toward for the integration of filter cavities with the current GW detectors in planned upgrades, but also a demonstration of the technology planned in the third-generation detectors such as the Einstein Telescope and Cosmic Explorer, which will use the frequency-dependent squeezing with kilometer-scale filter cavities [35, 36].

Chapter 8

Control of a Filter Cavity with Coherent Control Sidebands

One of the main challenges in the generation of frequency-dependent squeezing by using filter cavities is the length and alignment control of the filter cavity. Because squeezed vacuum has no coherent amplitude, it cannot provide the error signals necessary for the control. Therefore the use of auxiliary fields is necessary. In the experiments described in the previous chapter, the filter cavity was controlled using an auxiliary green field with a wavelength of 532 nm, while the wavelength of the squeezed field is 1064 nm. Because the optical paths for the green and squeezed fields are different and the relative alignment between them can drift, the length and alignment control of the filter cavity with the green field do not ensure the alignment of the squeezed field to the filter cavity. In addition, the fluctuation of the relative phase delay between the green and squeezed fields induced by the anisotropies or temperature dependency of the cavity mirror coating can lead to a detuning fluctuation [69].

In this chapter, I study a new scheme for the length and alignment control for the filter cavity whose length and alignment error signals can be provided by the coherent control (CC) field [18]. The CC field is present in all the squeezed vacuum sources for GW detectors and it is used to control the squeezing angle [49]. Because the coherent control sidebands (CCSB) are generated inside the OPO together with the squeezed vacuum field, they have the same mode matching conditions and almost the same frequency. The relative frequency of the squeezed field and CCSB can be controlled accurately using a PLL and can be tuned so that the squeezed field is properly detuned in the filter cavity. This frequency difference is only a few MHz which makes any possible phase delay effect caused by the coating negligible. Therefore, the length and alignment controls with CCSB ensure the appropriate detuning and alignment of the filter cavity for the squeezed vacuum field.

This new control scheme was also implemented in the 300 m filter cavity for the length control and an improvement of the locking accuracy from 3.4 pm to 0.75 pm was successfully demonstrated. The experimental demonstration of the new control scheme is also presented in this chapter.

8.1 Principle

8.1.1 Filter cavity length signal

From Equation (4.93), the CC field passing through the OPO can be written as

$$E_{\rm cc} = \sqrt{2\kappa_o^a} a_{\rm cav,cc} = a_{\rm cc}\frac{1}{(1-x^2)} e^{i(\omega_0+\Omega_{\rm cc})t} + a_{\rm cc}\frac{x}{(1-x^2)} e^{i(\omega_0-\Omega_{\rm cc})t+i\phi_{\rm pump}}, \tag{8.1}$$

where $a_{\rm cc}$ is the amplitude of the CC field at the OPO transmission without the pump field,

$$a_{\rm cc} = \frac{2\sqrt{\kappa_i^a\kappa_o^a}A_{\rm cc}}{\kappa^a}. \tag{8.2}$$

It should be noted that Equation (8.1) assumes that $\Omega_{\rm cc}$ is significantly smaller than the OPO bandwidth κ^a, $\Omega_{\rm cc} \ll \kappa^a$. In this chapter, we assume that $\phi_{\rm pump}$ is maintained at a constant value equal to 0 by CC1, but has residual noise, $\phi_{\rm pump} = \delta\phi_{\rm pump} \ll 1$.

To obtain frequency-dependent squeezing from a filter cavity, the resonance of the filter cavity must be properly detuned from the carrier. By choosing the frequency of the CC field ($\Omega_{\rm cc}$) as follows, the CC field can be resonant inside the filter cavity, while the resonance of the filter cavity is properly detuned from the carrier (Figure 8.1):

$$\Omega_{\rm cc} = n \times \omega_{\rm FSR} + \Delta\omega_{\rm fc,0}, \tag{8.3}$$

where n is an integer number, $\omega_{\rm FSR} = 2\pi f_{\rm FSR} = \pi c/L_{\rm fc}$ is the FSR of the filter cavity, $L_{\rm fc}$ is the filter cavity length, and $\Delta\omega_{\rm fc,0}$ is the optimal filter cavity detuning with respect to the carrier (5.29). Under this condition, the CC sideband at $-\Omega_{\rm cc}$ is detuned by $-2\Delta\omega_{\rm fc,0}$ with respect to the filter cavity resonance. Thus, this sideband is almost reflected by the filter cavity. The phase of the filter cavity reflectivity is shown in Figure 8.2. Because the phase of the filter cavity reflectivity for the CC field, which is on resonance, is sensitive to the filter cavity length change compared with the other sideband, which is off resonance, the filter cavity length signal can be obtained by detecting the beat notes of CCSB.

The CCSB reflected by the filter cavity can be written as

$$E_{\rm cc} \quad = \quad a_+ r_+ e^{i(\omega_0+\Omega_{\rm cc})t} + a_- r_- e^{i(\omega_0-\Omega_{\rm cc})t+i\delta\phi_{\rm pump}}, \tag{8.4}$$

where $a_\pm$ is

$$a_+ = a_{\rm cc}\frac{1}{(1-x^2)},\ a_- = a_{\rm cc}\frac{x}{(1-x^2)}, \tag{8.5}$$

and $r_\pm(\Delta\omega_{\rm fc}) = r_{\rm fc}(\pm\Delta\omega_{\rm fc,0}, \Delta\omega_{\rm fc})$ is the complex reflectivity of the filter cavity for the CCSB. From Equation (5.17), the reflectivity can be written as

$$r_{\rm fc}(\pm\Delta\omega_{\rm fc,0}, \Delta\omega_{\rm fc}) \simeq 1 - \frac{2-\epsilon}{1+i\xi(\pm\Delta\omega_{\rm fc,0}, \Delta\omega_{\rm fc})}, \tag{8.6}$$

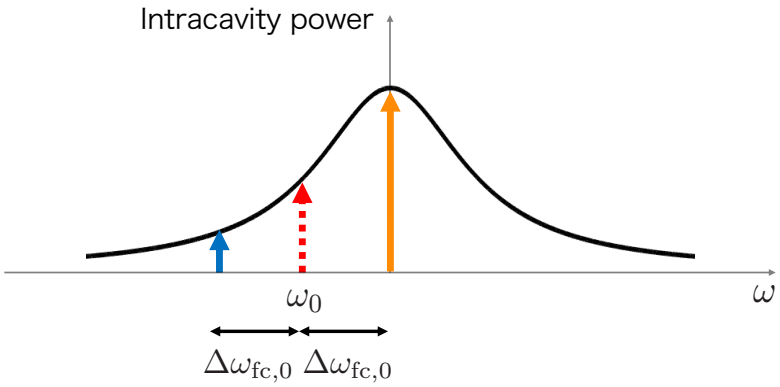

Figure 8.1: Frequency relationship inside the filter cavity. The red dashed line represents a carrier, and the orange and blue lines represent the CCSB.

where

$$\xi(\pm\Delta\omega_{\mathrm{fc},0}, \Delta\omega_{\mathrm{fc}}) = \frac{\pm\Delta\omega_{\mathrm{fc},0} - \Delta\omega_{\mathrm{fc}}}{\gamma_{\mathrm{fc}}}. \tag{8.7}$$

It should be noted that the sideband frequency Ω is fixed at $\pm\Delta\omega_{\mathrm{fc},0}$ for the CCSB under the condition expressed in Equation (8.3) and $\Delta\omega_{\mathrm{fc}}$ is the variable representing the actual (nonoptimal) filter cavity detuning.

Amplitude and phase of the filter cavity reflectivity for the CCSB can be written as

$$\begin{aligned}
\rho_{\pm}(\Delta\omega_{\mathrm{fc}}) &= |r_{\mathrm{fc}}(\pm\Delta\omega_{\mathrm{fc},0}, \Delta\omega_{\mathrm{fc}})| \\
&= \sqrt{1 - \frac{(2-\epsilon)\epsilon}{1+\xi^2(\pm\Delta\omega_{\mathrm{fc},0}, \Delta\omega_{\mathrm{fc}})}}, \qquad (8.8) \\
\alpha_{\pm}(\Delta\omega_{\mathrm{fc}}) &= \arg\{r_{\mathrm{fc}}(\pm\Delta\omega_{\mathrm{fc},0}, \Delta\omega_{\mathrm{fc}})\} \\
&= \arg\{-1+\epsilon+\xi^2(\pm\Delta\omega_{\mathrm{fc},0}, \Delta\omega_{\mathrm{fc}}) + \ i(2-\epsilon)\xi(\pm\Delta\omega_{\mathrm{fc},0}, \Delta\omega_{\mathrm{fc}})\}. \qquad (8.9)
\end{aligned}$$

The filter cavity length signal can be obtained by detecting the beat notes of the CCSB as follows:

$$\begin{aligned}
P_{\mathrm{cc}} &= \left| a_+ r_+ e^{i(\omega_0+\Omega_{\mathrm{cc}})t} + a_- r_- e^{i(\omega_0-\Omega_{\mathrm{cc}})t + i\delta\phi_{\mathrm{pump}}} \right|^2 \\
&= (\text{DC term}) \ + \ 2a_+a_-\mathrm{Re}\{r_+ r_-^* e^{i(2\Omega_{\mathrm{cc}}t - \delta\phi_{\mathrm{pump}})}\}. \qquad (8.10)
\end{aligned}$$

Demodulating this signal by $\sin(2\Omega_{\mathrm{cc}}t - \alpha_-(\Delta\omega_{\mathrm{fc},0}))$ (in-phase) and $\cos(2\Omega_{\mathrm{cc}}t - \alpha_-(\Delta\omega_{\mathrm{fc},0}))$ (quadrature) and low-passing it, we can obtain the filter cavity length signal as a function

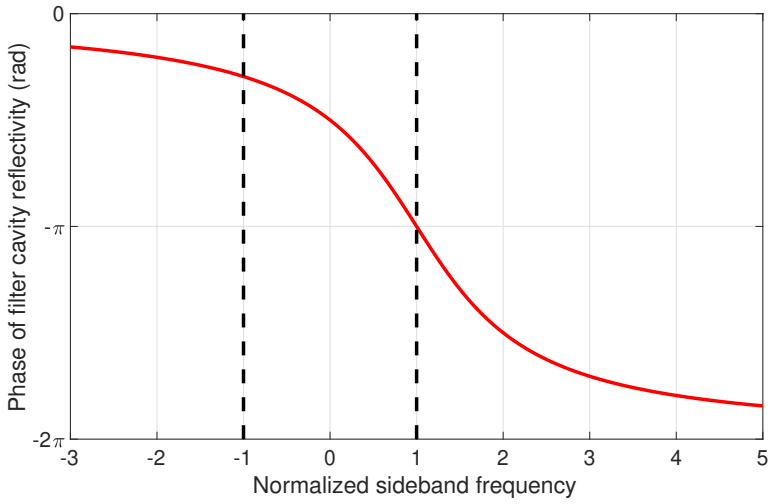

Figure 8.2: Phase of filter cavity reflectivity. The horizontal axis is the sideband frequency normalized with respect to $\Delta\omega_{\mathrm{fc},0}$. The black dashed lines represent the sideband frequency of the CCSB.

of the filter cavity detuning $\Delta\omega_{\mathrm{fc}}$ as follows:

$$\begin{aligned} P_I &= -a_+ a_- \rho_+(\Delta\omega_{\mathrm{fc}})\rho_-(\Delta\omega_{\mathrm{fc}}) \\ &\times \sin\left(\alpha_+(\Delta\omega_{\mathrm{fc}}) - \alpha_-(\Delta\omega_{\mathrm{fc}}) + \alpha_-(\Delta\omega_{\mathrm{fc},0}) - \delta\phi_{\mathrm{pump}}\right), \qquad (8.11) \\ P_Q &= a_+ a_- \rho_+(\Delta\omega_{\mathrm{fc}})\rho_-(\Delta\omega_{\mathrm{fc}}) \\ &\times \cos\left(\alpha_+(\Delta\omega_{\mathrm{fc}}) - \alpha_-(\Delta\omega_{\mathrm{fc}}) + \alpha_-(\Delta\omega_{\mathrm{fc},0}) - \delta\phi_{\mathrm{pump}}\right). \qquad (8.12) \end{aligned}$$

The relative phase noise of the CCSB $\delta\phi_{\mathrm{pump}}$ is a noise source for the filter cavity length signal. Assuming $\delta\phi_{\mathrm{pump}} = 0$, the normalized filter cavity length signals (8.11) and (8.12) with respect to $a_+ a_-$ are shown in Figure 8.3. The parameters used in this calculation are listed in Table 8.1.

The filter cavity length noise δL_{fc} causes detuning noise $\delta\Delta\omega_{\mathrm{fc}}$ as follows:

$$\delta\Delta\omega_{\mathrm{fc}} = \frac{\omega_0}{L_{\mathrm{fc}}}\delta L_{\mathrm{fc}}. \qquad (8.13)$$

When $\Delta\omega_{\mathrm{fc}} \equiv \Delta\omega_{\mathrm{fc},0} + \delta\Delta\omega_{\mathrm{fc}}$ is defined, the phase response of the filter cavity reflectivity to the detuning noise can be calculated from Equation (8.9) as follows:

$$\begin{aligned} \delta\alpha(\Omega) &= \left.\frac{d\alpha(\Omega,\Delta\omega_{\mathrm{fc}})}{d\Delta\omega_{\mathrm{fc}}}\right|_{\Delta\omega_{\mathrm{fc}}=\Delta\omega_{\mathrm{fc},0}} \delta\Delta\omega_{\mathrm{fc}} \\ &\simeq \left(\frac{(\Omega-\Delta\omega_{\mathrm{fc},0})^2}{\gamma_{\mathrm{fc}}^2}+1\right)^{-1}\frac{8\mathcal{F}}{\lambda}\delta L_{\mathrm{fc}}, \qquad (8.14) \end{aligned}$$

where $\alpha(\Omega,\Delta\omega_{\mathrm{fc}}) = \arg\{r_{\mathrm{fc}}(\Omega,\Delta\omega_{\mathrm{fc}})\}$, λ is the wavelength of the carrier, and $\mathcal{F}$ is the filter cavity finesse. Here, it is assumed that $\epsilon \ll 1$, which is true for the parameters listed

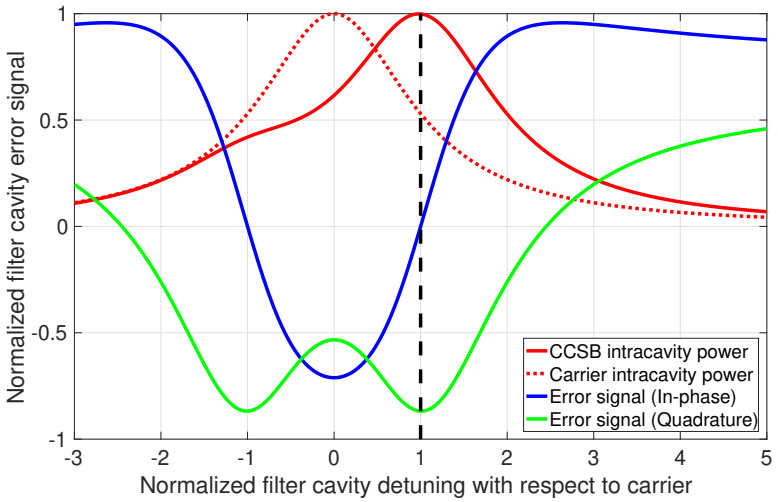

Figure 8.3: Filter cavity error signal normalized with respect to a_+a_-. The horizontal axis is the filter cavity detuning normalized with respect to $\Delta\omega_{\mathrm{fc},0}$. The red solid and dashed lines represent the intracavity power of the CCSB and carrier in the filter cavity normalized with respect to their maximum intracavity powers, respectively. The blue and green lines represent the filter cavity length signal (in-phase and quadrature). The filter cavity length signal (in-phase) becomes 0 when $\Delta\omega_{\mathrm{fc}} = \Delta\omega_{\mathrm{fc},0}$.

in Table 8.1. The filter cavity length signal (In-phase) (8.11) is

$$\begin{aligned}\frac{P_I}{a_+a_-\rho_+\rho_-} &= \sin(\alpha_+(\Delta\omega_{\mathrm{fc},0}+\delta\Delta\omega_{\mathrm{fc}}) - \alpha_+(\Delta\omega_{\mathrm{fc},0}) - \alpha_-(\Delta\omega_{\mathrm{fc},0}+\delta\Delta\omega_{\mathrm{fc}}) + \alpha_-(\Delta\omega_{\mathrm{fc},0})) \\ &\simeq \delta\alpha(\Delta\omega_{\mathrm{fc},0}) - \delta\alpha(-\Delta\omega_{\mathrm{fc},0}) \\ &= 26\ \mathrm{mrad}\left(\frac{1064\ \mathrm{nm}}{\lambda}\right)\left(\frac{\mathcal{F}}{4360}\right)\left(\frac{\delta L_{\mathrm{fc}}}{1\ \mathrm{pm}}\right). \end{aligned} \tag{8.15}$$

Because the relative phase noise of the CCSB ($\delta\phi_{\mathrm{pump}}$) can be stabilized by CC1 below 1.7 mrad [58], the residual filter cavity length signal (8.15) can be obtained with a good enough SNR. The phase noise of an RF source for the demodulation also becomes a noise source for the filter cavity length signal. The typical phase noise of an RF source for the demodulation is several tens of μrad and, therefore, significantly smaller than the residual filter cavity length signal (8.15).

8.1.2 Filter cavity alignment signal

The CCSB can be also used to control the alignment of the filter cavity using the wave front sensing (WFS) technique [70]. The principle of wave front sensing is explained in Appendix A.

The misalignment of the filter cavity axis with respect to the input beam axis as well as that of the immediately reflected beam axis with respect to the filter cavity axis can be

Table 8.1: Parameters for 300 m filter cavity [62].

Parameter	Symbol	Value
Filter cavity length	$L_{\rm fc}$	300 m
Filter cavity half-bandwidth	$\gamma_{\rm fc}$	$2\pi \times 57.3$ Hz
Filter cavity detuning	$\Delta\omega_{\rm fc,0}$	$2\pi \times 54$ Hz
Filter cavity finesse	$\mathcal{F}$	4360
Filter cavity input mirror transmissivity	$t_{\rm in}^2$	0.00136
Filter cavity round-trip losses	$\Lambda_{\rm rt}^2$	80 ppm
Injection losses	$\Lambda_{\rm inj}^2$	5 %
Readout losses	$\Lambda_{\rm ro}^2$	5 %
Mode-mismatch losses (squeezer-filter cavity)	$\Lambda_{\rm mmFC}^2$	2 %
Mode-mismatch losses (squeezer-local oscillator)	$\Lambda_{\rm mmLO}^2$	5 %
Frequency-independent phase noise (rms)	$\delta\phi$	30 mrad
Filter cavity length noise (rms)	$\delta L_{\rm fc}$	1 pm
Generated squeezing	$\sigma_{\rm dB}$	9 dB
Nonlinear gain	g	3.6

represented in terms of the dimensionless coupling factors γ and γ_r as follows:

$$\gamma = \delta x/w_0 + i\delta\theta/\theta_0, \tag{8.16}$$

$$\gamma_r = \delta x'/w_0 + i\delta\theta'/\theta_0, \tag{8.17}$$

where w_0 is the beam radius at the waist position and $\theta_0 = \lambda/\pi w_0$ is the beam divergence. δx and $\delta x'$ represent the shift in the x-axis direction measured at the waist position of the filter cavity axis with respect to the input beam axis and the immediately reflected beam axis with respect to the filter cavity axis, respectively. $\delta\theta$ and $\delta\theta'$ represent the tilt around the y-axis of the filter cavity axis with respect to the input beam axis and the immediately reflected beam axis with respect to the filter cavity axis, respectively. Here, the z-axis is the beam axis and the y-axis is orthogonal to the x- and z-axis. $z = 0$ is the beam waist position. γ and γ_r can be expressed in terms of the input and end mirror misalignment of the filter cavity as follows:

$$\gamma = \frac{R}{2}\frac{\delta\theta_I + \delta\theta_E}{w_0} + i\frac{R}{2R - L_{\rm fc}}\frac{\delta\theta_I - \delta\theta_E}{\theta_0} \tag{8.18}$$

$$\begin{aligned}\gamma_r &= \frac{L_{\rm fc}\delta\theta_I - \frac{R}{2}(\delta\theta_I + \delta\theta_E)}{w_0} + i\frac{2\delta\theta_I - \frac{R}{2R-L_{\rm fc}}(\delta\theta_I - \delta\theta_E)}{\theta_0}, \\ &= \left(\frac{L_{\rm fc}}{w_0} + i\frac{2}{\theta_0}\right)\delta\theta_I - \gamma,\end{aligned} \tag{8.19}$$

where R is the radius of curvature of the input and end mirrors, $\delta\theta_I$ and $\delta\theta_E$ are the angular misalignments of the input and end mirrors, respectively. The directions of the input and end mirror misalignments are defined so that the positive direction of the misalignment

causes the shift of the filter cavity axis in the positive direction of the x-axis.

We treat only the x-axis misalignment (HG 10 mode), and the calculations of the y-axis misalignment (HG 01 mode) are entirely analogous.

From Equation (A.21) and (A.22), the $2\Omega_{\rm cc}$ term of the filter cavity error signal (8.10) can be written as

$$\begin{aligned} P_{\rm cc}(2\Omega_{\rm cc}) &= 2a_+a_-{\rm Re}\{r_+r_-^*e^{i2\Omega_{\rm cc}t}\} \\ &= 2a_+a_-{\rm Re}\{(U_{00}r_{c0}-U_{10}C)(U_{00}^*r_{s0}^*-U_{10}^*S^*)e^{i2\Omega_{\rm cc}t}\} \\ &= 2a_+a_-{\rm Re}\{(U_{00}U_{00}^*r_{c0}r_{s0}^*-U_{00}U_{10}^*r_{c0}S^* \\ &\qquad -U_{00}^*U_{10}r_{s0}^*C+U_{10}U_{10}^*CS^*)e^{i2\Omega_{\rm cc}t}\}. \end{aligned} \tag{8.20}$$

The WFS signal (W) is expressed as the sum of the second and the third terms of Equation (8.20). Defining $U = U_{00}U_{10}^*$ yields

$$\begin{aligned} W &= 2a_+a_-{\rm Re}(\{-Ur_{c0}(r_{s0}^*\gamma_r^*+r_{s1}^*\gamma)- U^*r_{s0}^*(r_{c0}\gamma_r+r_{c1}\gamma^*)\}e^{i2\Omega_{\rm cc}t}) \\ &= 2a_+a_-{\rm Re}(\{-r_{c0}r_{s0}^*(U\gamma_r^*+U^*\gamma_r)- r_{c0}r_{s1}^*U\gamma-r_{c1}r_{s0}^*U^*\gamma^*\}e^{i2\Omega_{\rm cc}t}). \end{aligned} \tag{8.21}$$

The differential signal of W in the x-axis direction with a QPD is

$$W_{\rm diff} = \int\int dxdy\{W(x>0)-W(x<0)\}. \tag{8.22}$$

As

$$\int\int dxdy\{U(x>0)-U(x<0)\} = \sqrt{\frac{2}{\pi}}e^{-i\eta(z)}, \tag{8.23}$$

and $r_{c1}, r_{s1} \simeq 1$ because of the Gouy phase separation in the cavity, the WFS signal can be written as

$$W_{\rm diff} = 2a_+a_-\sqrt{\frac{2}{\pi}}{\rm Re}(\{-r_+r_-^*(e^{-i\eta}\gamma_r^*+e^{i\eta}\gamma_r)-r_+e^{-i\eta}\gamma-r_-^*e^{i\eta}\gamma^*\}e^{i2\Omega_{\rm cc}t}), \tag{8.24}$$

where $r_\pm = r_\pm(\Delta\omega_{\rm fc,0})$ and η represents the Gouy phase. Demodulating (8.24) by $\sin(2\Omega_{\rm cc}t-\alpha_-(\Delta\omega_{\rm fc,0}))$ (In-phase) and low-passing it, the first term of Equation (8.24), which is proportional to the filter cavity length signal, will disappear.

The WFS signal after the demodulation is

$$\begin{aligned} W_I &= \sqrt{\frac{2}{\pi}}a_+a_- \\ &\times \{{\rm Re}(r_+e^{-i\eta}\gamma+r_-^*e^{i\eta}\gamma^*)\sin\alpha_-(\Delta\omega_{\rm fc,0}) \\ &+ {\rm Im}(r_+e^{-i\eta}\gamma+r_-^*e^{i\eta}\gamma^*)\cos\alpha_-(\Delta\omega_{\rm fc,0})\}. \end{aligned} \tag{8.25}$$

The WFS signal as a function of the Gouy phase is shown in Figure 8.4. The displacement

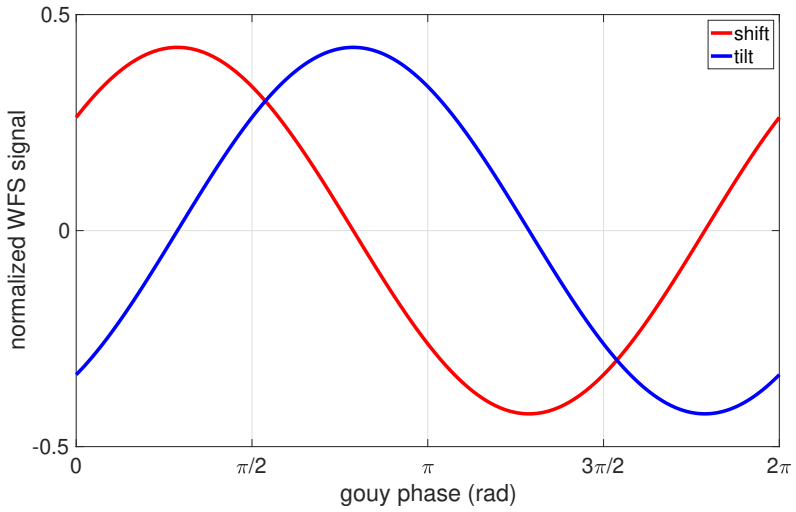

Figure 8.4: Filter cavity WFS signal as a function of the Gouy phase normalized with $\sqrt{\frac{2}{\pi}}a_+a_-$. The red and blue lines represent the shift signal with $\delta x = w_0$ and the tilt signal with $\delta\theta = \theta_0$, respectively.

and tilt signals of the filter cavity can be obtained with two different Gouy phases.

The fourth term in Equation (8.20) is the beat note of the CCSB HG10 mode and becomes a noise source for the filter cavity length signal, which is the first term in Equation (8.20). The fourth term in Equation (8.20) is

$$\begin{aligned} & 2a_+a_-|U_{10}|^2\mathrm{Re}\{CS^*e^{i2\Omega_{\mathrm{cc}}t}\} \\ = \; & 2a_+a_-|U_{10}|^2\mathrm{Re}\{(r_{c0}r_{s0}^*|\gamma_r|^2 + r_{c0}r_{s1}^*\gamma_r\gamma + r_{c1}r_{s0}^*\gamma^*\gamma_r^* + r_{c1}r_{s1}^*|\gamma|^2)e^{i2\Omega_{\mathrm{cc}}t}\}. \end{aligned} \tag{8.26}$$

Demodulating by $\sin(2\Omega_{\mathrm{cc}}t - \alpha_-(\Delta\omega_{\mathrm{fc},0}))$, the first term in Equation (8.26), which is proportional to the filter cavity length signal, will disappear. After integration with respect to x, y, Equation (8.26) will become

$$\begin{aligned} -a_+a_- \quad \{ \quad & \mathrm{Re}(r_{c0}\gamma_r\gamma + r_{s0}^*\gamma^*\gamma_r^*)\sin\alpha_-(\Delta\omega_{\mathrm{fc},0}) \\ + \quad & \mathrm{Im}(r_{c0}\gamma_r\gamma + r_{s0}^*\gamma^*\gamma_r^*)\cos\alpha_-(\Delta\omega_{\mathrm{fc},0}) \\ + \quad & |\gamma|^2\sin\alpha_-(\Delta\omega_{\mathrm{fc},0})\}, \end{aligned} \tag{8.27}$$

where $r_{c1}, r_{s1} \simeq 1$ is used. From Equation (8.18) and (8.19), Equation (8.27) can be numerically calculated in terms of the input and end mirror misalignment $\delta\theta_I, \delta\theta_E$ as shown in Figure 8.5. Here it is assumed that $R = 415$ m and $w_0 = 0.825$ cm [63]. Equation (8.27) normalized with a_+a_- should be smaller than the residual filter cavity length signal normalized with a_+a_- which is $P_I/a_+a_- = 23$ mrad. It should be noted that the filter cavity length signal in Equation (8.15) is normalized with $a_+a_-\rho_+\rho_-$. We consider the maximum angular motion of the filter cavity mirrors θ_{max} as $\delta\theta_I^2 + \delta\theta_E^2 = \theta_{\mathrm{max}}^2$

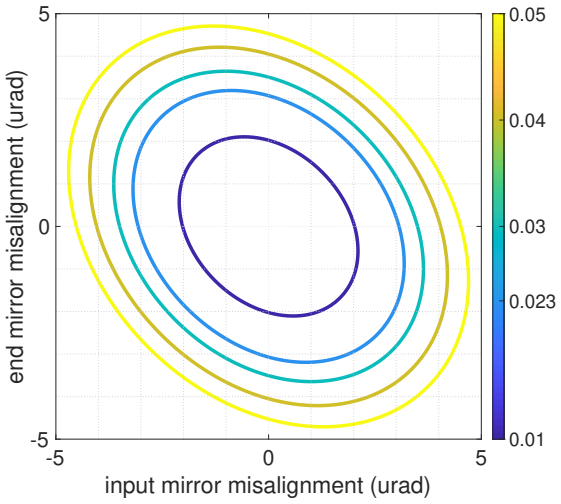

Figure 8.5: Coupling from input and end mirror misalignment of the filter cavity to the filter cavity length signal (8.27) normalized with respect to a_+a_-. As the coupling should be smaller than the filter cavity length signal ~ 0.023, the input and end mirror misalignment should be inside the ellipse corresponding to 0.023.

which corresponds to a circle with radius $\theta_{\rm max}$ in Figure 8.5. This circle should be smaller than the ellipse corresponding to 0.023. $\theta_{\rm max}$ can be determined from the semi-minor axis of the ellipse corresponding to 0.023 in Figure 8.5. Thus, the requirement of $\theta_{\rm max}$ is obtained as $\theta_{\rm max} = 2.7$ μrad, which is achievable through double pendulum suspensions in KAGRA [71]. By numerically calculating $|\gamma|^2$ as a functions of the input and end mirror misalignment, this requirement corresponds to $|\gamma|^2 = 0.01$. Because this requirement is more stringent than the requirement of mode-mismatch losses (squeezer-filter cavity), which is 2 %, the requirement of γ is set as $|\gamma|^2 = 0.01$.

8.1.3 Experimental setup in GW detectors

An example of the experimental implementation of this scheme in GW detectors is shown in Figure 8.6. There are three control loops related to the CC field which are CC1, CC2, and the filter cavity control loop with CCSB (hereafter, we refer to it as CCFC).

The CCFC error signal can be obtained at an output mode cleaner (OMC) reflection because the CCSB are almost fully reflected by the OMC, while the carrier is almost entirely transmitted. The CCFC error signal is obtained by demodulating the OMC reflection at a frequency of $2\Omega_{\rm cc}$ and is fed back to the filter cavity length. The demodulation phase can be determined by injecting the bright carrier field to the filter cavity and simultaneously checking the carrier transmission and CCFC error signal, as shown in Figure 8.3. The demodulation phase can be fine-tuned by optimizing the GW sensitivity. The CC1 error signal for controlling the relative phase between the green pump field and the CC field can be obtained at the OPO reflection and it is fed back to the optical path length of the pump field. The CC2 error signal for controlling the relative phase between the carrier and the CC field is obtained at the OMC transmission and fed back to the PLL

between the interferometer and squeezer lasers [72].

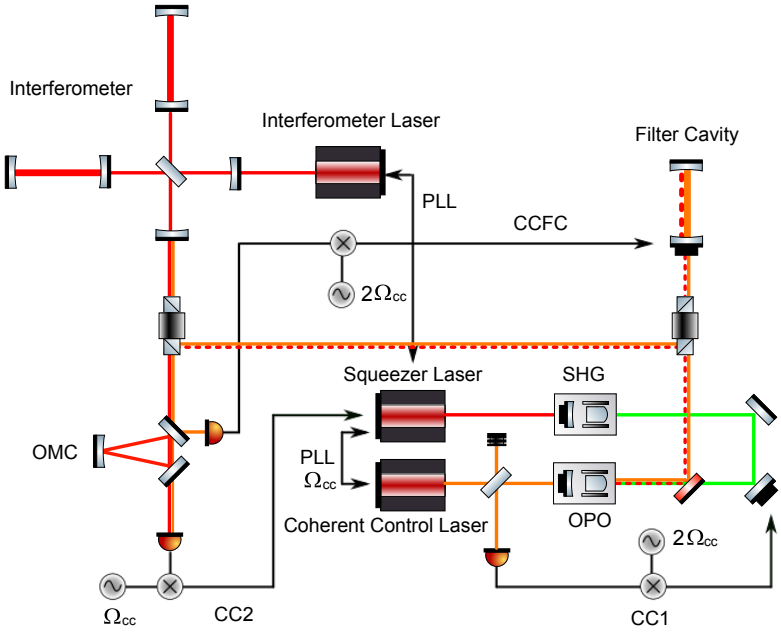

Figure 8.6: Example of experimental implementation of a CCFC scheme in GW detectors. The red solid, red dashed and orange lines represent the carrier, squeezed field, and CC field, respectively. The green line represents the green pump field, which is generated by the SHG and injected into the OPO.

8.1.4 Coherent control error signal

As either of CCSB enters the filter cavity and senses the filter cavity length noise, the filter cavity length noise appears in the CC2 loop, which controls the relative phase between the LO and CCSB. In the case of GW detectors, the LO is the interferometer laser. In this section, the CC2 error signal, which includes the phase noise coming from the filter cavity, is calculated. For simplicity, we write $\rho_\pm(\Delta\omega_{\rm fc}) = \rho_\pm$, $\alpha_\pm(\Delta\omega_{\rm fc}) = \alpha_\pm$ and $\alpha_\pm(\Delta\omega_{\rm fc,0}) = \alpha_{\pm,0}$.

The power at the OMC transmission is

$$\begin{aligned} P_{\rm CC2} &= \Big| a_0 e^{i(\omega_0 t+\phi_{\rm LO})} + \tau_{\rm cc} a_+ \rho_+ e^{i(\omega_0+\Omega_{\rm cc})t+i(\phi_{\rm CC}+\alpha_+)} \\ &+ \tau_{\rm cc} a_- \rho_- e^{i(\omega_0-\Omega_{\rm cc})t+i(\phi_{\rm CC}+\alpha_-+\delta\phi_{\rm pump})} \Big|^2 \\ &= 2\tau_{\rm cc} a_0 a_+ \rho_+ \cos\left(\Omega_{\rm cc} t - \phi_{\rm LO} + \phi_{\rm CC} + \alpha_+\right) \\ &+ 2\tau_{\rm cc} a_0 a_- \rho_- \cos\left(\Omega_{\rm cc} t + \phi_{\rm LO} - \phi_{\rm CC} - \alpha_- - \delta\phi_{\rm pump}\right) \\ &+ (\text{DC term}) + (2\Omega_{\rm cc}\text{ term}), \end{aligned} \tag{8.28}$$

where a_0 is the amplitude of the LO and $\tau_{\rm cc}$ is the transmissivity of the CCSB from the OPO to the OMC transmission.

Demodulating (8.28) by $\cos(\Omega_{\rm cc}t + \theta_{\rm dm,CC2})$ and low-passing it, where the demodulation phase $\theta_{\rm dm,CC2}$ is

$$\theta_{\rm dm,CC2} = \frac{\alpha_{+,0} - \alpha_{-,0}}{2}, \tag{8.29}$$

we find

$$\begin{aligned} P_{\rm I} &= \tau_{\rm cc} a_0 a_+ \rho_+ \sin\left(-\phi_{\rm LO} + \phi_{\rm CC} + \alpha_{p,0} + \delta\alpha_+ + \frac{\pi}{2}\right) \\ &- \tau_{\rm cc} a_0 a_- \rho_- \sin\left(\phi_{\rm LO} - \phi_{\rm CC} - \alpha_{p,0} - \delta\alpha_- - \frac{\pi}{2} - \delta\phi_{\rm pump}\right), \end{aligned} \tag{8.30}$$

where

$$\alpha_{p,0} = \frac{\alpha_{+,0} + \alpha_{-,0}}{2}, \tag{8.31}$$

$$\delta\alpha_\pm = \alpha_\pm - \alpha_{\pm,0}. \tag{8.32}$$

When the squeezing angle $\phi_{\rm sqz}$ is changed from $\pi/2$ (squeeze quadrature) by $\delta\phi_{\rm sqz}$, Equation (4.92) can be written as

$$\phi_{\rm sqz} = \phi_{\rm LO} - \phi_{\rm CC} = \frac{\pi}{2} + \delta\phi_{\rm sqz}. \tag{8.33}$$

Assuming $\delta\phi_{\rm sqz}, \delta\alpha_\pm, \delta\phi_{\rm pump} \ll 1$, the CC2 error signal (8.30) can be written as

$$\begin{aligned} P_{\rm I} &= \tau_{\rm cc} a_0 a_+ \rho_+ [(1 + a\rho)\sin\alpha_{p,0} \\ &+ \{-(1 + a\rho)\delta\phi_{\rm sqz} + 2\delta\alpha_p(\Delta\omega_{\rm fc}, a, \rho) + a\rho\delta\phi_{\rm pump}\}\cos\alpha_{p,0}], \end{aligned} \tag{8.34}$$

where $a = a_-/a_+ = x$ is the unbalance of the amplitude of the CCSB and $\rho = \rho_-/\rho_+$ is the unbalance of the filter cavity reflectivity of the CCSB. $\delta\alpha_p(\Delta\omega_{\rm fc}, a, \rho)$ becomes

$$\delta\alpha_p(\Delta\omega_{\rm fc}, a, \rho) = \frac{\delta\alpha_+ + a\rho\delta\alpha_-}{2}. \tag{8.35}$$

The first term in Equation (8.34) is the constant offset, the second term is the relative phase noise between CC and LO, which does not include the phase noise coming from the filter cavity (frequency-independent phase noise), the third term is the phase noise of the CCSB coming from the filter cavity length noise (frequency-dependent phase noise at the detuning frequency), and the fourth term is the phase noise coming from the relative phase noise of the CCSB. The constant offset in Equation (8.34) should be removed to obtain $\delta\phi_{\rm sqz}$. $\delta\alpha_p(\Delta\omega_{\rm fc}, a, \rho)$ is the coupling from the CCFC loop which reshapes frequency-dependent phase noise as explained in the following section.

8.1.5 Reshaping of frequency-dependent phase noise

The CC2 error signal calculated in Section 8.1.4 reshapes the frequency-dependent phase noise, which originates from the filter cavity length noise. This is caused by the coupling

between the CCFC and CC2 loops as shown in Figure 8.7.

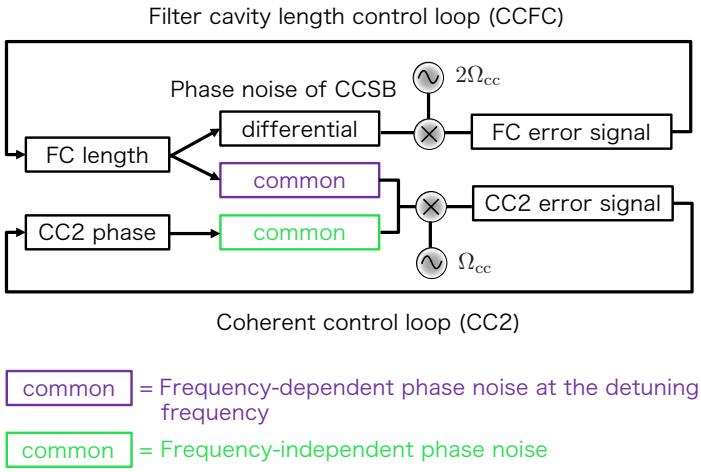

Figure 8.7: Coupling between CCFC and CC2 loops.

The fluctuation of the filter cavity length causes both differential and common phase noise of the CCSB. The differential phase noise of the CCSB is the CCFC error signal, while the common phase noise of the CCSB is the frequency-dependent phase noise at the detuning frequency, which is the second term in Equation (8.34). This frequency-dependent phase noise at the detuning frequency couples to the CC2 loop and is suppressed by the CC2 feedback loop, while the frequency-dependent phase noise increases at high frequencies. In this section, the calculation of the frequency-dependent phase noise with the feedback of the CC2 loop is explained.

The frequency-dependent phase noise when the CCSB are off resonance of the filter cavity can be calculated as Equation (5.53). However, with the CCFC scheme, the detuning noise of the filter cavity (8.35) is fed back by the CC2 loop. As shown in Figure 8.6, this feedback from the CC2 loop is sent to the squeezer laser, which leads to a change in the injection squeezing angle ϕ. Therefore, the frequency-dependent phase noise of $\hat{N}_1$ with feedback from the CC2 loop can be calculated as follows:

$$\begin{aligned} & \hat{N}_{1,\mathrm{avg}}(\phi, \Delta\omega_{\mathrm{fc},0}) \\ = \; & \frac{1}{2}\Big\{\hat{N}_1(-\delta\alpha_p(\Delta\omega_{\mathrm{fc},0} + \delta\Delta\omega_{\mathrm{fc}}, a, \rho), \Delta\omega_{\mathrm{fc},0} + \delta\Delta\omega_{\mathrm{fc}}) \\ & + \hat{N}_1(-\delta\alpha_p(\Delta\omega_{\mathrm{fc},0} - \delta\Delta\omega_{\mathrm{fc}}, a, \rho), \Delta\omega_{\mathrm{fc},0} - \delta\Delta\omega_{\mathrm{fc}})\Big\}. \end{aligned} \tag{8.36}$$

It should be noted that frequency-dependent phase noise $\delta\alpha_p$ is low above the cavity pole of the filter cavity $\sim$ 57 Hz, and it is assumed that the gain of the CC2 loop below the cavity pole is large enough such that the feedback of the CC2 loop is perfect.

Figure 8.8 and 8.9 show quantum noise relative to the coherent vacuum with filter cavity length noise $\delta L_{\mathrm{fc}} = 1$ pm and 3 pm. The frequency-dependent phase noise with

the CCFC scheme and the conventional scheme are represented as purple and dotted purple lines, which are almost overlapping in Figure 8.8. The parameters used in this calculation are listed in Table 8.1. The unbalance of the filter cavity reflectivity for the CCSB is $\rho = 1.1$ and the unbalance of the amplitude for the CCSB is $a = 0.47$ ($g = 3.6$). As shown in Figure 8.8, the frequency-dependent phase noise with the CCFC scheme and conventional schemes are low and almost the same with $\delta L_{\rm fc} = 1$ pm. However, as indicated in Figure 8.9, the frequency-dependent phase noise with the CCFC scheme is suppressed at low frequencies by the feedback from the CC2 loop, while it is increased at high frequencies.

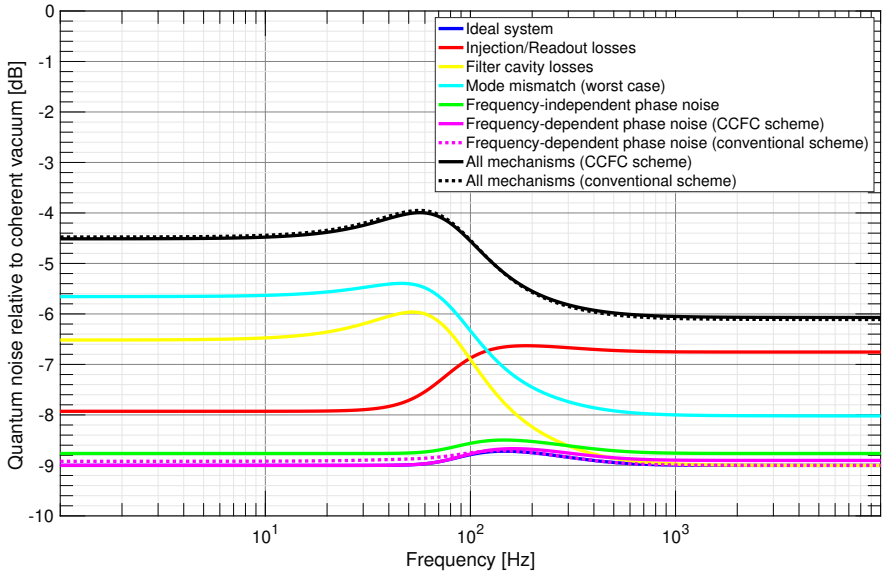

Figure 8.8: Quantum noise relative to coherent vacuum with $\delta L_{\rm fc} = 1$ pm. The solid purple and black lines represent the frequency-dependent phase noise and total noise with the CCFC scheme, respectively. The dotted purple and black lines represent the frequency-dependent phase noise and total noise with the conventional scheme, respectively. The solid lines and dotted lines are almost overlapping because the effect of the frequency-dependent phase noise is small with $\delta L_{\rm fc} = 1$ pm.

Effective phase noise at high frequencies with feedback from the CC2 loop ($\delta\alpha_p$ in Equation (8.36)) can be calculated from Equation (8.14) and (8.35) as follows:

$$\begin{aligned} |\delta\alpha_p(\Delta\omega_{\rm fc,0} \pm \delta\Delta\omega_{\rm fc}, a, \rho)| &= \frac{\delta\alpha(\Delta\omega_{\rm fc,0}) + a\rho\delta\alpha(-\Delta\omega_{\rm fc,0})}{2} \\ &\simeq 18 \text{ mrad} \left(\frac{1064 \text{ nm}}{\lambda}\right)\left(\frac{\mathcal{F}}{4360}\right)\left(\frac{\delta L_{\rm fc}}{1 \text{ pm}}\right). \end{aligned} \quad (8.37)$$

The squeezing angle is affected by the misalignment of LO and CC. The squeezing angle fluctuation at the OMC transmission, including the misalignment of the LO and CC, can

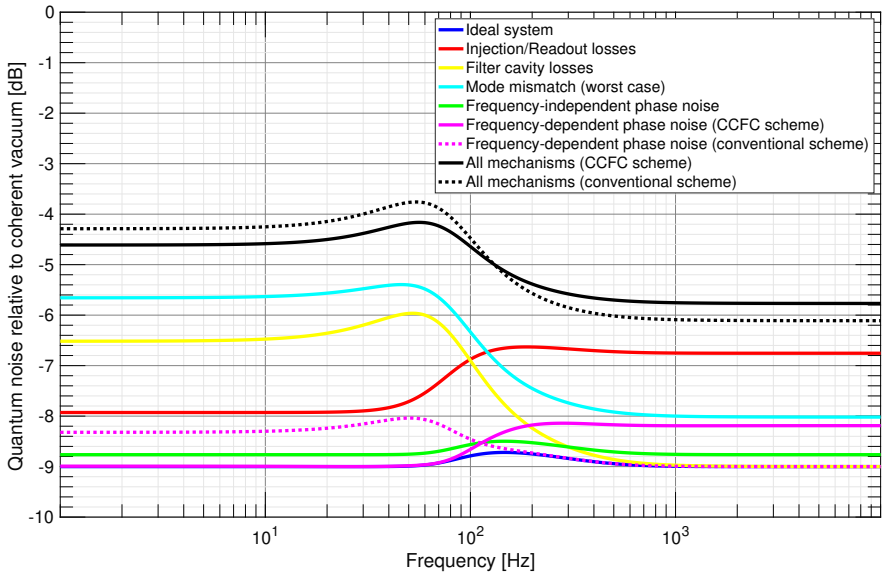

Figure 8.9: Quantum noise relative to coherent vacuum with $\delta L_{\rm fc} = 3$ pm. The solid purple and black lines represent the frequency-dependent phase noise and total noise with the CCFC scheme, respectively. The dotted purple and black lines represent the frequency-dependent phase noise and total noise with the conventional scheme, respectively. The frequency-dependent phase noise with the CCFC scheme is reduced at low frequencies, while it is increased at high frequencies compared with that with the conventional scheme.

be written as [73]

$$\delta\phi_{\rm alignment} \simeq \sum_{ij} A_{ij}\rho_{ij}^{\rm CC}\rho_{ij}^{\rm LO}\sin\phi_{ij}, \tag{8.38}$$

where $A_{ij} \sim 1/100$ is the attenuation factor of higher order modes caused by the OMC and $\rho_{ij}^{\rm CC}$ and $\rho_{ij}^{\rm LO}$ are the relative amplitudes of the CC and LO TEM ij modes with respect to the TEM 00 mode. $\phi_{ij} = \phi_{ij}^{\rm LO} - \phi_{ij}^{\rm CC}$ and $\phi_{ij}^{\rm LO}, \phi_{ij}^{\rm CC}$ are the relative phases of the CC and LO TEM ij modes with respect to the TEM 00 mode. Considering only the HG10/01 mode and assuming that $|\rho_{ij}^{\rm CC}|^2 = |\rho_{ij}^{\rm LO}|^2 = 10^{-2}$ for $i + j = 1$, the squeezing angle fluctuation will be $\delta\phi_{\rm alignment} \sim \mathcal{O}(10^{-4})$ rad, which is low enough compared with the frequency-independent/dependent phase noise.

8.2 Noise Calculation

The requirements of length and alignment control for the filter cavity are $\delta L_{\rm fc} = 1$ pm and $|\gamma|^2 = 0.01$, respectively. In this section, it is shown that shot noise and PLL noise satisfy these requirements. It is also illustrated that backscattering noise caused by the leaked carrier from the interferometer to the filter cavity does not spoil the quantum noise above 10 Hz, where the quantum noise limits the GW sensitivity.

8.2.1 Shot noise

Shot noise for length control

We assume that the power of the CC field after passing through the OPO is $P_+ = a_+^2 = 1$ μW and the power of the lower CC sideband is $P_- = a^2 P_+ = 0.22$ μW. When the filter cavity length signal is obtained at the OMC reflection, the junk light at the OMC reflection, which includes higher order modes and other RF sidebands, contributes to the shot noise.

The shot noise of the CCSB and the junk light at the OMC reflection is written as

$$P_{\rm shot} = \sqrt{2\hbar\omega_0(\rho_+^2 P_+ + \rho_-^2 P_- + P_{\rm junk})} \simeq \sqrt{2\hbar\omega_0 P_{\rm junk}}, \tag{8.39}$$

where it is assumed that the frequencies of the carrier, CCSB, and junk light are approximately the same and $\rho_\pm^2 P_\pm \ll P_{\rm junk}$. This shot noise within the filter cavity control bandwidth becomes the filter cavity length noise owing to the control loop. This shot noise is the most fundamental limit for the filter cavity length signal. From Equation (8.15), we can calculate the maximum power of the junk light at the OMC reflection so as not to spoil the filter cavity length signal as follows,

$$\rho_+\rho_-\sqrt{P_+P_-}\{\delta\alpha(\Delta\omega_{\rm fc,0}) - \delta\alpha(-\Delta\omega_{\rm fc,0})\} \quad > \quad \sqrt{2\hbar\omega_0 P_{\rm junk}\Delta f}, \tag{8.40}$$

$$\begin{aligned} P_{\rm junk} \quad &< \quad 15\frac{P_+P_-}{\hbar\omega_0\Delta f}\frac{\delta L_{\rm fc}^2}{\lambda^2}\mathcal{F}^2 \\ &= \quad 15\ {\rm W} \\ &\times \quad \left(\frac{P_+}{1\ \mu{\rm W}}\right)^2\left(\frac{\mathcal{F}}{4360}\right)^2\left(\frac{\delta L_{\rm fc}}{1\ {\rm pm}}\right)^2\left(\frac{20\ {\rm Hz}}{\Delta f}\right), \end{aligned} \tag{8.41}$$

where Δf is the filter cavity length control bandwidth which is set by the requirement of backscattering noise [65]. According to Equation (8.41) and assuming the parameters listed in Table 8.1, $P_{\rm junk} < 15$ W should be satisfied so as not to spoil the filter cavity length signal. This requirement is satisfied [74].

Shot noise for alignment control

In this section, we consider only the shot noise of the shift signal of the filter cavity. The calculation for the tilt signal is entirely analogous. From Equation (8.25), we can calculate the maximum power of the junk light at the OMC reflection so as not to spoil the filter cavity alignment signal as follows:

$$\sqrt{\frac{2}{\pi}}\sqrt{P_+P_-}a_{\rm WFS}\frac{\delta x}{w_0} > \sqrt{2\hbar\omega_0 P_{\rm junk}\Delta f_{\rm WFS}}, \tag{8.42}$$

$$
\begin{aligned}
P_{\rm junk} &< 0.056 \frac{P_+ P_-}{\hbar\omega_0 \Delta f_{\rm WFS}} \left(\frac{\delta x}{w_0}\right)^2 \\
&= 660 \text{ W} \\
&\times \left(\frac{P_+}{1\ \mu\text{W}}\right)^2 \left(\frac{(\delta x/w_0)^2}{0.01}\right) \left(\frac{1 \text{ Hz}}{\Delta f_{\rm WFS}}\right), \qquad (8.43)
\end{aligned}
$$

where $a_{\rm WFS} = 0.42$ is the maximum amplitude of the normalized WFS signal in Figure 8.4 and $\Delta f_{\rm WFS}$ is the filter cavity alignment control bandwidth. According to Equation (8.43), $P_{\rm junk} < 660$ W should be satisfied so as not to spoil the filter cavity alignment signal and this requirement is also satisfied.

8.2.2 Backscattering noise

The backscattering noise originates from the leaked carrier from the interferometer to the filter cavity. The leaked carrier is injected into the filter cavity and scattered by the filter cavity length noise and reinjected into the interferometer. Because this leaked carrier has the same frequency as the squeezed field, the fluctuation of the leaked carrier must be lower than the vacuum fluctuation so as not to spoil the quantum noise of the interferometer [65]. Considering the safety factor ($C_{\rm safe} = 1/10$) and the squeezing enhancement factor ($C_{\rm sqz} \simeq 1/2$ for 6 dB of quantum noise enhancement),

$$
\begin{aligned}
\delta\alpha(0)\sqrt{P_{\rm leak}} &< C_{\rm safe} C_{\rm sqz} \sqrt{2\hbar\omega_0}, \qquad (8.44) \\
P_{\rm leak} &< 3.1 \times 10^{-10} \text{ W} \\
&\times \left(\frac{4360}{\mathcal{F}}\right)^2 \left(\frac{10^{-16} \text{ m}/\sqrt{\text{Hz}}}{\delta L_{\rm fc}(f)}\right)^2, \qquad (8.45)
\end{aligned}
$$

where $\delta\alpha(0)$ is the phase response of the carrier to the filter cavity length noise (8.14) and $P_{\rm leak}$ is the power of the leaked carrier from the interferometer to the filter cavity. It is assumed that $\delta L_{\rm fc}(f) = 10^{-16}$ m/$\sqrt{\text{Hz}}$ above 10 Hz, which can be realized in Advanced LIGO [65]. As the carrier output from the interferometer is $P_{\rm carrier} = 35$ mW in Advanced LIGO [65], the isolation factor of 81 dB is required from the output of the interferometer to the filter cavity. Recently, a Faraday isolator with an isolation factor higher than 40 dB and less than 1 % of loss [67] has been developed. Using two Faraday isolators, an isolation factor higher than 80 dB can be achieved with a loss less than 2 %, and the backscattering noise can satisfy the requirement.

8.2.3 PLL noise

The PLL that controls the relative frequency between the squeezer laser and the CC laser can cause the detuning noise. The PLL frequency noise reflected by the filter cavity can be written as

$$
S_{\rm PLL,fc}(f) = \frac{S_{\rm PLL}(\phi) f}{\sqrt{1 + (f/f_{\rm fc})^2}}, \qquad (8.46)
$$

where $f_{\rm fc} = 57.3$ Hz is the filter cavity half bandwidth and $S_{\rm PLL}(\phi) = 5\ \mu{\rm rad}/\sqrt{\rm Hz}$ is the PLL phase noise within the PLL control bandwidth ~ 40 kHz. The PLL phase noise has been chosen such that the rms value of the PLL phase noise, $\delta\phi_{\rm PLL} = 1$ mrad. The rms value of the PLL frequency noise within the filter cavity control bandwidth is

$$\begin{aligned}
\delta f_{\rm PLL,fc} &= \sqrt{\int_0^{\Delta f} df\, S^2_{\rm PLL,fc}(f)} \\
&= S_{\rm PLL}(\phi)\sqrt{\int_0^{\Delta f} df \frac{f^2}{1+(f/f_{\rm fc})^2}} \\
&= S_{\rm PLL}(\phi) f_{\rm fc}\sqrt{\left(\Delta f - f_{\rm fc}\arctan\frac{\Delta f}{f_{\rm fc}}\right)}.
\end{aligned} \tag{8.47}$$

The rms value of the PLL frequency noise is $\delta f_{\rm PLL,fc} = 0.25$ mHz, which corresponds to the rms value of the filter cavity length noise $\delta L_{\rm PLL,fc} = 2.7 \times 10^{-16}$ m. Therefore, the PLL noise satisfies the requirement.

8.3 Comparison to the other locking scheme

Other than the CCFC scheme, a filter cavity locking scheme using the resonant locking field (RLF) has been demonstrated at MIT for the length control [68]. The configuration of the CCFC and RLF schemes in GW detectors is shown in Figure 8.10. RLF is phase locked to the CC field and detuned with respect to it to resonate inside the filter cavity. RLF is injected into the OPO together with the CC field and shares the same optical path with it, except that the RLF is resonant inside the filter cavity, while the CC field is not. The filter cavity length signal is obtained from the beat note of the RLF and LO from the interferometer at the OMC transmission.

Compared with the RLF scheme, the CCFC scheme has the advantage in that it uses the already present CC field and does not require any modification of the optical setup. However, the CCFC scheme is worse in terms of the shot noise level. Here, we compare the SNR in the CCFC and RLF schemes in terms of shot noise.

SNR in the CCFC scheme in terms of the shot noise is

$$\mathrm{SNR}_{\rm CCFC} \sim \frac{P_{\rm CC}}{\sqrt{2\hbar\omega_0 P_{\rm junk}}}\delta\alpha_m, \tag{8.48}$$

where $P_{\rm CC}$ is the CC power at the OMC reflection and $\delta\alpha_m$ is the relative phase change of the CCSB by the filter cavity length noise.

SNR in the RLF scheme in terms of shot noise is

$$\mathrm{SNR}_{\rm RLF} \sim \frac{\sqrt{P_{\rm LO}AP_{\rm RLF}}}{\sqrt{2\hbar\omega_0 P_{\rm LO}}}\delta\alpha_p = \frac{\sqrt{AP_{\rm RLF}}}{\sqrt{2\hbar\omega_0}}\delta\alpha_p, \tag{8.49}$$

where $P_{\rm LO}$ is the LO power from the interferometer at the OMC transmission, $P_{\rm RLF}$ is the RLF power before OMC, $A \sim 1/100$ is the attenuation factor of the RLF by the OMC,

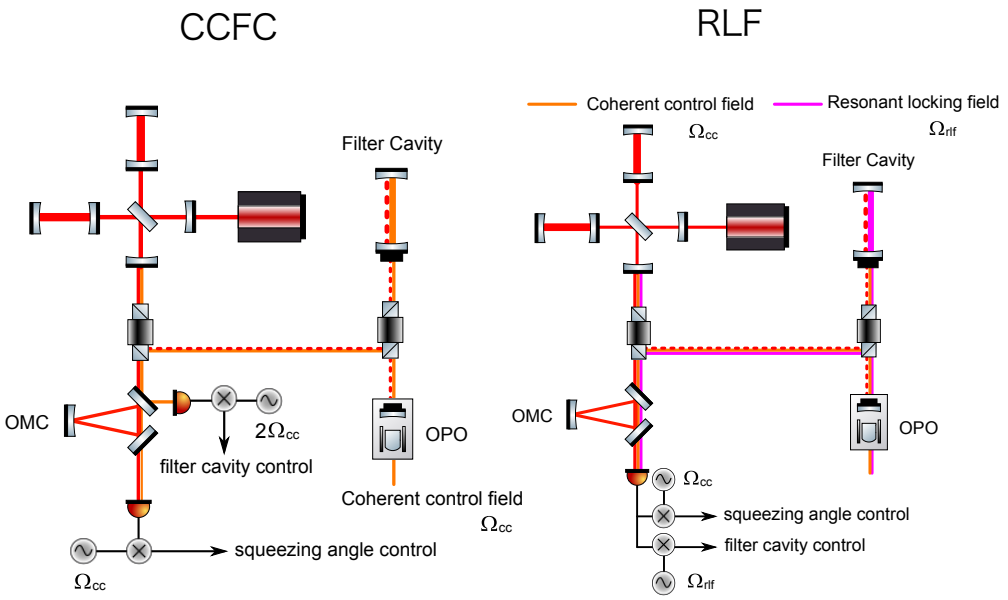

Figure 8.10: Configuration of CCFC (left) and RLF (right) schemes in GW detectors. The solid red, orange, purple, and dashed red lines represent the carrier field, CC field, RLF, and squeezed fields, respectively. The CC and RLF are detuned by $\Omega_{\rm cc}$ and $\Omega_{\rm rlf}$ with respect to the carrier, respectively.

and $\delta\alpha_p$ is the common phase change of the CCSB by the filter cavity length noise.

The ratio of the SNRs in the CCFC and RLF schemes is

$$\frac{\mathrm{SNR_{CCFC}}}{\mathrm{SNR_{RLF}}} \sim \frac{P_{\rm CC}}{\sqrt{P_{\rm junk}AP_{\rm RLF}}} \sim \frac{1}{\sqrt{A}}\sqrt{\frac{P_{\rm CC}}{P_{\rm junk}}} \sim 0.03, \tag{8.50}$$

where we assumed that $\delta\alpha_p \sim \delta\alpha_m$ and $P_{\rm CC} = P_{\rm RLF} = 1\ \mu$W, $P_{\rm junk} = 100$ mW which are typical values in GW detectors. This ratio indicates that the SNR in the CCFC scheme is worse than that in the RLF scheme by a factor of ~ 30. Nevertheless, the shot noise level in the CCFC scheme can satisfy the requirement, as it was calculated in Section 8.2.1.

8.4 Demonstration of CCFC lock with 300 m filter cavity

本章については、５年以内に雑誌等で刊行予定のため、非公開。

8.5 Conclusion

In this chapter, I suggested a new length and alignment control scheme of a filter cavity with coherent control sidebands, which are already used to control the squeezing angle. This scheme ensures accurate length and alignment of the filter cavity with respect to the squeezed vacuum field because the CCSB are copropagating fields at almost the same

frequency as the squeezed field. I implemented the new control scheme in 300 m filter cavity for the length control and demonstrated that the new control scheme improved the locking accuracy of the filter cavity from 3.4 pm to 0.75 pm, which satisfies the target value of 1 pm. Frequency-dependent squeezing with the filter cavity length control by the CCFC lock was also realized. The detuning fluctuation was about 10 Hz, which might be better than that without the CCFC lock.

The current squeezing level in the CCFC scheme is limited by losses. A loss of 50 % is introduced from the BS to pick off the CCFC error signal, and this loss can be avoided in the real GW detectors becase the CCFC error signal can be obtained at the OMC reflection without introducing the pick-off BS. In the future, alignment control of the filter cavity using the CCFC scheme will be implemented to improve the mode matching between the squeezer and the filter cavity. This implementation is also expected to stabilize the detuning fluctuation, which enables the stable operation of the filter cavity. The CCFC scheme developed in this chapter will be tested in the real GW detectors in the near future.

Chapter 9

Conclusion

The sensitivity of GW detectors is designed to be limited by quantum noise. The quantum noise originates from the quantum vacuum field entering from an output port of the interferometer. The quantum noise is composed of shot noise and radiation pressure noise. The shot noise originates from the phase fluctuation of the vacuum field and dominates at high frequencies of the detector sensitivity, while the radiation pressure noise originates from the amplitude fluctuation of the vacuum field and dominates at low frequencies. The sensitivity of current GW detectors is dominated by shot noise at high frequencies. To reduce the shot noise, the frequency-independent squeezing, whose phase quadrature is squeezed, has been injected into the interferometer and the shot noise reduction by $\sim$3 dB has been achieved in Advanced LIGO and Advanced Virgo. However, the increase of the radiation pressure noise due to the frequency-independent squeezing has been observed in Advanced LIGO and Advanced Virgo.

To reduce the shot noise and radiation pressure noise simultaneously, the frequency-dependent squeezing which is phase squeezed at high frequencies and amplitude squeezed at low frequencies is required. The most promising way to realize the frequency-dependent squeezing is reflecting the frequency-independent squeezed vacuum field off an optical cavity called the filter cavity. In the past, the squeezing angle rotation using rigid, meter-scale filter cavities has been realized in the MHz and kHz regions. However, frequency-dependent squeezing with a rotation frequency below 100 Hz, which is required in GW detectors, has not yet been demonstrated.

In this thesis, we developed the first frequency-dependent squeezed vacuum source with a rotation frequency below 100 Hz by using a 300 m filter cavity which can fit for Advanced LIGO and Advanced Virgo. It is shown that our frequency-dependent squeezed vacuum source can realize the broadband quantum noise reduction in GW detectors. For further quantum noise reduction, it is necessary to stabilize the filter cavity length fluctuation, the alignment fluctuation, and the detuning fluctuation. In this measurement, the filter cavity was controlled with an auxiliary green field whose frequency is as twice as the squeezing frequency. As the optical path and the frequency for the green field and the squeezed field are different, the filter cavity control with the auxiliary green field does not ensure the filter cavity length and alignment for the squeezed field.

To solve this problem, I suggested a new control scheme of the filter cavity using coherent control sidebands which are already used to control the squeezing angle. As the coherent control sidebands have the same optical path and almost the same frequency as the squeezed field, the control of the filter cavity with the coherent control sidebands ensures the filter cavity length and alignment for the squeezed field. I succeeded in controlling the length of the 300 m filter cavity with the new control scheme and demonstrated that the new control scheme reduced the filter cavity length fluctuation from 3.4 pm to 0.75 pm which satisfies the target value of 1 pm. Using this new control scheme, the frequency-dependent squeezing with a rotation frequency around 100 Hz also has been realized.

Frequency-dependent squeezed vacuum source with the several hundred-meter-long filter cavities is planned to be installed in current GW detectors such as Advanced LIGO, Advanced Virgo, and KAGRA in the near future. The new control scheme for the filter cavity developed in this thesis could be integrated in these detectors. Using these technologies, the sensitivity of the current GW detectors will be improved at all frequencies and the detection range will be improved by $\sim$50 %, which increases the detection rate by more than three times. The result in this thesis is also a big step toward for the sensitivity improvement of the future third-generation GW detectors such as the Einstein Telescope and Cosmic Explorer, which require even longer filter cavities and the higher squeezing levels. Therefore, the result in this thesis will be significant for the development of GW astronomy.

Appendix A

Auto alignment

For the stable operation of the filter cavity, it is essential to control the angles of the filter cavity mirrors. The auto alignment of the filter cavity can be achieved using a wave front sensing (WFS) technique [70]. In this appendix, the theory of WFS and the experiment of WFS with the green field in TAMA are presented.

A.1 Wave front sensing

A filter cavity input beam, which includes the Hermite-Gaussian (HG) 10 mode can be written as

$$E_{\rm in} = \begin{pmatrix} U_{00} & U_{10} \end{pmatrix} \begin{pmatrix} a_0 \\ a_1 \end{pmatrix} E_0 e^{i\omega t}, \tag{A.1}$$

where a_0 and a_1 are the amplitudes of the HG 00 and 10 modes, respectively.

We recall the HG mode expression [76]:

$$U_{mn}(x,y,z) = U_m(x,z)U_n(y,z)\exp[-ikz + i(m+n+1)\eta(z)], \tag{A.2}$$

where

$$U_m(x,z) = \left(\frac{2}{\pi w^2(z)}\right)^{1/4} \sqrt{\frac{1}{2^m m!}} H_m\left(\frac{\sqrt{2}x}{w(z)}\right) \exp\left[-\left(\frac{x}{w(z)}\right)^2 - i\frac{kx^2}{2R(z)}\right], \tag{A.3}$$

where H_m is the m-th order Hermite polynomial, $w(z)$ is the beam radius, $\eta(z)$ is the Gouy phase, and $R(z)$ is the beam radius of curvature:

$$w(z) = w_0\sqrt{1 + z^2/z_0^2}, \tag{A.4}$$
$$\eta(z) = \arctan(z/z_0), \tag{A.5}$$
$$R(z) = z(1 + z_0^2/z^2), \tag{A.6}$$
$$z_0 = kw_0^2/2, \tag{A.7}$$

where z_0 is the Rayleigh range and w_0 is the beam radius at the waist position.

A filter cavity mode that has a shift δx and a tilt $\delta\theta$ with respect to the input beam can be written as

$$E_{\rm fc} = \begin{pmatrix} U_{00} & U_{10} \end{pmatrix} M(\gamma) \begin{pmatrix} a_0 \\ a_1 \end{pmatrix} E_0 e^{i\omega t}, \tag{A.8}$$

$$M(\gamma) = \begin{pmatrix} 1 & \gamma \\ -\gamma^* & 1 \end{pmatrix}, \tag{A.9}$$

where

$$\gamma = \delta x/w_0 + i\delta\theta/\theta_0. \tag{A.10}$$

Here $\theta_0 = \lambda/(\pi w_0)$ is the beam divergence, and the first order of γ is considered.

The reflection matrix for an optimally aligned filter cavity can be written as

$$R_{\rm fc}^{\rm align} = \begin{pmatrix} r_{c0} & 0 \\ 0 & r_{c1} \end{pmatrix}, \tag{A.11}$$

where $r_{\rm c0}$ and $r_{\rm c1}$ are the cavity reflectivities for the HG 00 and HG 10 mode, respectively:

$$r_{\rm c0} = r_I - \frac{t_I^2 r_E e^{-i\phi}}{1 - r_I r_E e^{-i\phi}}, \tag{A.12}$$

$$r_{\rm c1} = r_I - \frac{t_I^2 r_E e^{-i(\phi+\eta_{\rm rt})}}{1 - r_I r_E e^{-i(\phi+\eta_{\rm rt})}}. \tag{A.13}$$

Here ϕ is the round-trip phase for the HG 00 mode and $\eta_{\rm rt}$ is the round-trip Gouy phase:

$$\phi = \frac{2L\omega}{c},\ \eta_{\rm rt} = \arctan(2L/z_0). \tag{A.14}$$

The reflection matrix of a misaligned filter cavity in the first order of γ, γ_r can be written as

$$\begin{aligned} R_{\rm fc}^{\rm mis}(\gamma, \gamma_r) &= M^*(\gamma_r) R_{\rm fc}^{\rm align} M(\gamma) \\ &= \begin{pmatrix} r_{c0} & r_{c0}\gamma + r_{c1}\gamma_r^* \\ -(r_{c0}\gamma_r + r_{c1}\gamma^*) & r_{c1} \end{pmatrix}, \end{aligned} \tag{A.15}$$

where we define:

$$\gamma_r = \delta x'/w_0 + i\delta\theta'/\theta_0, \tag{A.16}$$

where $\delta x'$ and $\delta\theta'$ are the shift and tilt of the promptly reflected beam axis with respect to the cavity axis.

Assuming that $a_0 = 1, a_1 = 0$ for the input beam, the beam reflected from a misaligned filter cavity can be written as

$$E_{\rm ref} = [U_{00} r_{c0} - U_{10}(r_{c0}\gamma_r + r_{c1}\gamma^*)] E_0 e^{i\omega t} = [U_{00} r_{c0} - U_{10} C] E_0 e^{i\omega t}, \tag{A.17}$$

where, for compactness, we defined

$$C = r_{c0}\gamma_r + r_{c1}\gamma^*. \tag{A.18}$$

This can be generalized to the case of a sideband:

$$E_{\text{ref}} = [U_{00}r_{s0} - U_{10}(r_{s0}\gamma_r + r_{s1}\gamma^*)]E_0 e^{i(\omega+\Omega)t} = [U_{00}r_{s0} - U_{10}S]E_0 e^{i(\omega+\Omega)t}, \tag{A.19}$$

where r_{s0} and r_{s1} are the cavity reflectivities for the HG 00 and HG 10 modes of the sideband and

$$S = r_{s0}\gamma_r + r_{s1}\gamma^*. \tag{A.20}$$

It is useful to introduce a compact form that "hides" the spatial modes:

$$E^c_{\text{ref}} = [U_{00}r_{c0} - U_{10}C]E_0 e^{i\omega t} = r_c E_0 e^{i\omega t}, \tag{A.21}$$

$$E^s_{\text{ref}} = [U_{00}r_{c0} - U_{10}S]E_0 e^{i(\omega+\Omega)t} = r_s E_0 e^{i(\omega+\Omega)t}, \tag{A.22}$$

to recall the usual expression for the in-phase PDH signal (3.38):

$$P^I_{\text{demod}} = P_0 J_0(\beta)J_1(\beta)\text{Im}(r_c r_s^* - r_c^* r_s), \tag{A.23}$$

and

$$\begin{aligned} r_c r_s^* - r_c^* r_s &= [U_{00}r_{c0} - U_{10}C][U_{00}r_{s0} - U_{10}S]^* - [U_{00}r_{c0} - U_{10}C]^*[U_{00}r_{s0} - U_{10}S] \\ &= U_{00}U_{00}^*(r_{c0}r_{s0}^* - r_{c0}^* r_{s0}) + U_{00}U_{10}^*(r_{s0}C^* - r_{c0}S^*) + U_{00}^*U_{10}(r_{c0}^*S - r_{s0}^*C) \\ &\quad + U_{10}U_{10}^*(CS^* - C^*S). \end{aligned} \tag{A.24}$$

The first term is the usual PDH signal, which is spatially symmetric and cancelled out in the WFS. For the same reason, the fourth term, which contains only the HG10 modes, will cancel out. Therefore, we retain only the terms that mix the HG00 and HG10 modes. By defining $U = U_{00}U_{10}^*$, the WFS signal is

$$\begin{aligned} W &= U[r_{s0}(r_{c0}^*\gamma_r^* + r_{c1}^*\gamma) - r_{c0}(r_{s0}^*\gamma_r^* + r_{s1}^*\gamma)] \\ &+ U^*[r_{c0}^*(r_{s0}\gamma_r + r_{s1}\gamma^*) - r_{s0}^*(r_{c0}\gamma_r + r_{c1}\gamma^*)] \\ &= -(r_{c0}r_{s1} - r_{c1}r_{s0})(U\gamma - U^*\gamma^*) \\ &= -(r_{c0}r_{s1} - r_{c1}r_{s0})\left[(U - U^*)\frac{\delta x}{w_0} + (U + U^*)i\frac{\delta\theta}{\theta_0}\right]. \end{aligned} \tag{A.25}$$

Here, we assumed that all the reflectivities are real numbers. Using Equation (A.3), it can be proven that

$$U - U^* = -2iU_1^*U_0^*U_0U_0\sin\eta, \tag{A.26}$$

$$U + U^* = 2U_1^*U_0^*U_0U_0\cos\eta. \tag{A.27}$$

Equation (A.23) will become

$$\begin{aligned} P^I_{\rm demod} &= P_0 J_0(\beta) J_1(\beta) {\rm Im} W \\ &= 2P_0 J_0(\beta) J_1(\beta) U_1^* U_0^* U_0 U_0 (r_{c0} r_{s1} - r_{c1} r_{s0}) \left[\frac{\delta x}{w_0} \sin\eta - \frac{\delta\theta}{\theta_0} \cos\eta \right]. \end{aligned} \tag{A.28}$$

The WFS signal is obtained by considering the difference between the two halves of the QPD. It can be proven that:

$$\int\int dxdy \{U_1^* U_0^* U_0 U_0 (x>0) - U_1^* U_0^* U_0 U_0 (x<0)\} = \sqrt{\frac{2}{\pi}}. \tag{A.29}$$

Finally, we can write the WFS signal as follows:

$$P^I_{\rm WFS,demod} = \sqrt{\frac{8}{\pi}} P_0 J_0(\beta) J_1(\beta) (r_{c0} r_{s1} - r_{c1} r_{s0}) \left[\frac{\delta x}{w_0} \sin\eta - \frac{\delta\theta}{\theta_0} \cos\eta \right]. \tag{A.30}$$

The relation between the cavity axis shift, tilt and input, end mirror misalignment, $\delta\theta_I$ and $\delta\theta_E$ can be expressed as follows:

$$\begin{pmatrix} \delta x \\ \delta\theta \end{pmatrix} = \frac{1}{R_I + R_E - L} \begin{pmatrix} R_I(R_E - L_E) & R_E(R_I - L_I) \\ R_I & -R_E \end{pmatrix} \begin{pmatrix} \delta\theta_I \\ \delta\theta_E \end{pmatrix}, \tag{A.31}$$

where R_I and R_E are the input and end mirror radius of curvature, respectively, and L_I and L_E are the distances between the waist and the input and end mirrors:

$$L_I = \frac{L(L-R_E)}{2L - R_I - R_E}, \tag{A.32}$$

$$L_E = \frac{L(L-R_I)}{2L - R_I - R_E}. \tag{A.33}$$

Using the values listed in Table A.1 for the TAMA filter cavity, we find that:

$$\begin{pmatrix} \delta x \\ \delta\theta \end{pmatrix} = \begin{pmatrix} 224 & 217 \\ 0.75 & -0.76 \end{pmatrix} \begin{pmatrix} \delta\theta_I \\ \delta\theta_E \end{pmatrix}. \tag{A.34}$$

This yields

$$\begin{aligned} \delta x &= 224\,\delta\theta_I + 217\,\delta\theta_E, \\ \delta\theta &= 0.75\,\delta\theta_I - 0.76\,\delta\theta_E. \end{aligned}$$

When the carrier is on resonance and the sidebands are located far from the resonance, we have

$$r_{c0} = 0.61,\ r_{c1} = r_{s0} = r_{s1} \simeq 1. \tag{A.35}$$

Table A.1: Filter cavity parameters for wavefront sensing with green field.

Parameter	Symbol	Real value
Length	L	300 m
Input mirror radius of curvature	R_I	438 m
End mirror radius of curvature	R_E	445 m
Input mirror transmissivity (532 nm)	T_I	0.7%
End mirror transmissivity (532 nm)	T_E	2.9%
Finesse (532 nm)	$\mathcal{F}$	172
Modulation depth	β	0.185 rad
Modulation Frequency	Ω	78 MHz
Beam radius at waist (532 nm)	w_0	0.0059 m
Beam divergence (532 nm)	θ_0	$2.85 \cdot 10^{-5}$ m
Rayleigh range (532 nm)	z_0	209 m
Round-trip Gouy phase (532 nm)	η_{rt}	1.236 rad
Power on WFS	P_0	2.7 mW

This means that the WFS for the misalignment of the input mirror is

$$\begin{aligned} P_I \text{ [W]} &= \sqrt{\frac{8}{\pi}} P_0 J_0(\beta) J_1(\beta)(r_{c0} r_{s1} - r_{c1} r_{s0}) \left(\frac{224}{w_0} \sin\eta - \frac{0.75}{\theta_0} \cos\eta \right) \delta\theta_I \\ &= (3.4 \sin\eta - 2.4 \cos\eta)\delta\theta_I, \end{aligned} \tag{A.36}$$

and that for the end mirror is

$$\begin{aligned} P_E \text{ [W]} &= \sqrt{\frac{8}{\pi}} P_0 J_0(\beta) J_1(\beta)(r_{c0} r_{s1} - r_{c1} r_{s0}) \left(\frac{217}{w_0} \sin\eta + \frac{0.76}{\theta_0} \cos\eta \right) \delta\theta_E \\ &= (3.3 \sin\eta + 2.4 \cos\eta)\delta\theta_E. \end{aligned} \tag{A.37}$$

The WFS signal as a function of the Gouy phase is shown in Figure A.1.

A.2 Experimental setup

Becase there was not enough space to accommodate the optics for auto alignment, a second layer optical table was constructed on the optical bench as shown in Figure A.2.

Two QPDs are placed with 90 degree of Gouy phase separation. The input and end mirrors of the filter cavity are controlled with WFS signals from the two QPDs. There is also a QPD for the green field at the filter cavity transmission, which is used to control the pointing of the injection green field. The pointing signal is fed back to a steering mirror at the BS chamber.

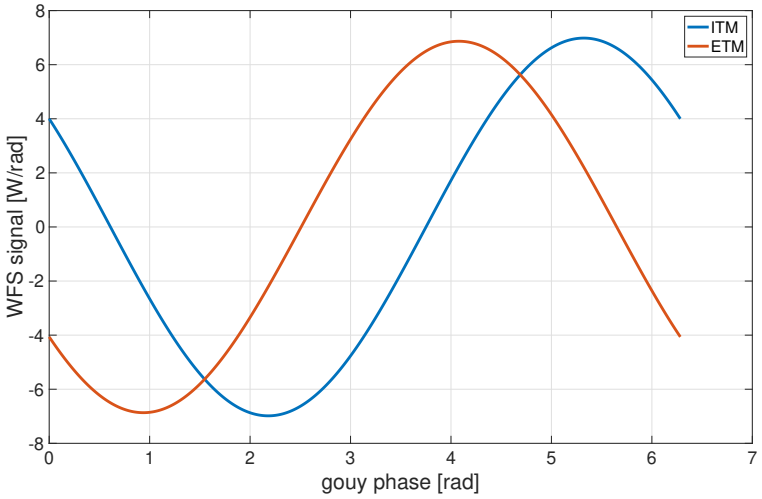

Figure A.1: WFS signal as a function of the Gouy phase for the green field. The blue and red curves are the WFS signals for the input and end mirrors of the filter cavity, respectively.

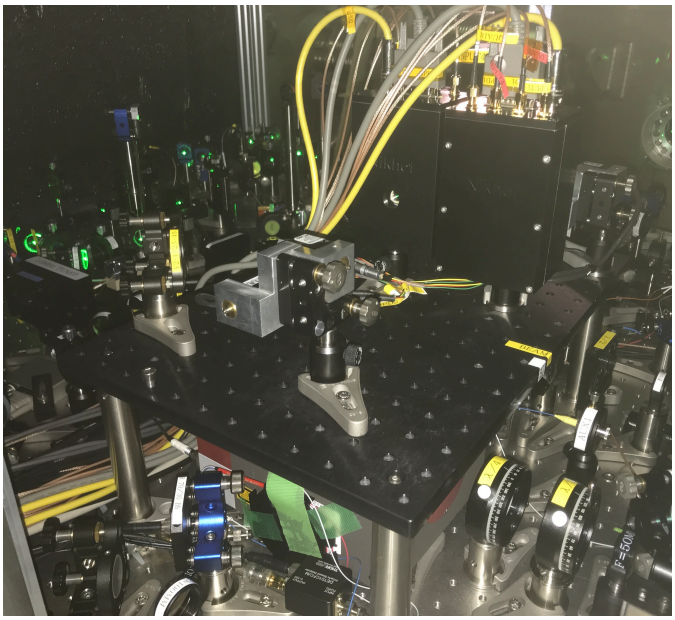

Figure A.2: Second layer optical table for auto alignment.

A.3 QPD centering loop

For WFS, it is necessary to center the beam in the QPD. To achieve this, a beam centering system was developed in TAMA [77]. The QPD DC signals are used to extract the pitch and yaw motion of the beam and fed back to actuators called galvo. The galvo has two galvanometer scanners mounted orthogonally, each of which is used to rotate a small mirror as shown in Figure A.3.

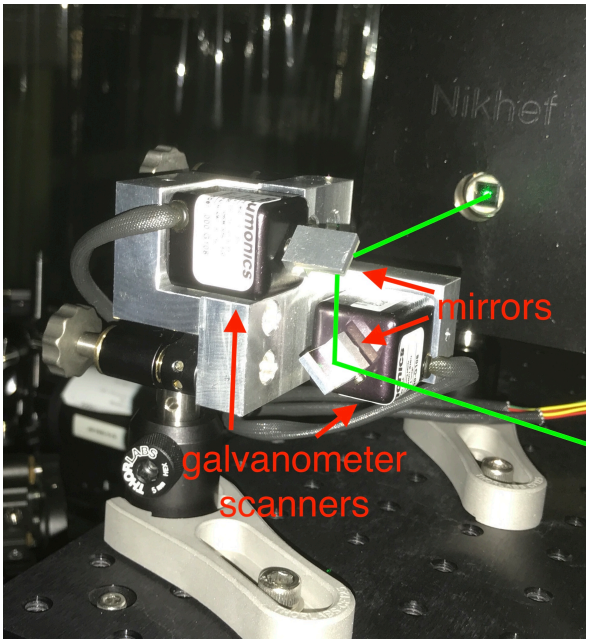

Figure A.3: Galvo actuator for auto alignment.

Using the beam centering system, we successfully locked the QPD centering loops for pitch and yaw in the both QPDs. The servo for the beam centering system can measure the closed-loop transfer function by measuring ADD OUT/ADD IN in the servo [77]. The open-loop transfer function can be obtained from the closed-loop transfer function by using the following formula:

$$G_{\mathrm{OL}} = -1 + \frac{1}{G_{\mathrm{CL}}}, \tag{A.38}$$

where G_{OL} andG_{CL} are the open- and closed-loop transfer functions.

The measured open-loop transfer function of the QPD centering loop is shown in Figure A.4. It should be noted that the UGF can be increased up to around 2 kHz.

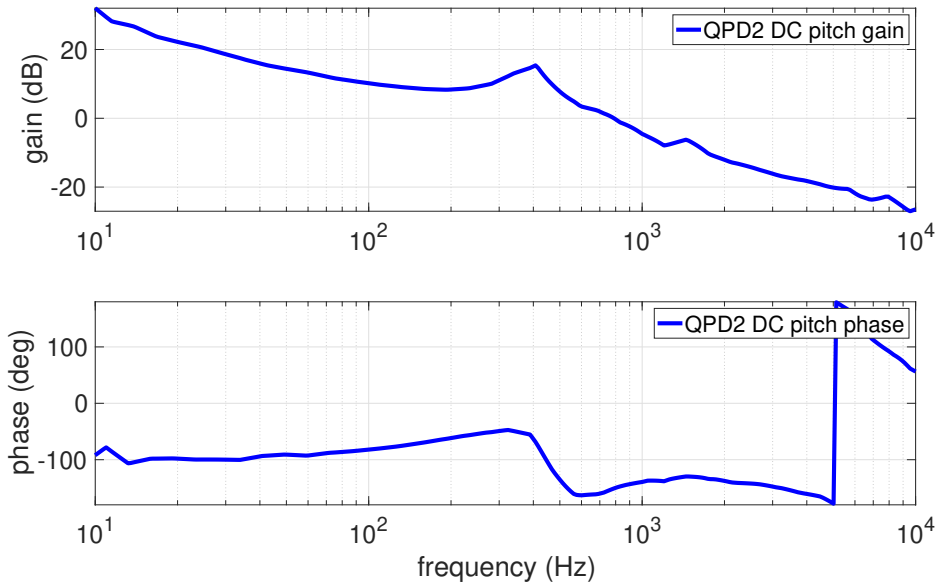

Figure A.4: Open-loop transfer function of the beam centering system. The UGF is 800 Hz and the phase margin is 30 deg.

A.4 WFS loop

Currently, the WFS loop is working and the filter cavity alignment for the green field is stabilized by WFS. A characterization of the WFS loop is ongoing.

Appendix B

List of devices

In this appendix, the list of devices used in this experiment is summarized. Table B.1 and B.2 are lists of EOM and PD.

Table B.1: List of EOM.

type	function	name	manufacturer
resonant (15.2 MHz)	SHG/IRMC (15.2 MHz)	Model 4003	New focus
resonant (78 MHz)	FC/GRMC (78 MHz)	EO-78K3-VIS	Qubig
resonant (87.6 MHz)	OPO (87.6 MHz)	EO-88K3-NIR	Qubig

Table B.2: List of photo detector.

type	function	name	manufacturer
resonant (15.2 MHz)	SHG/IRMC (15.2 MHz), CC1/CCFC (14 MHz)	8880 (TAMA PD)	Clear-pulse
broadband	FC/GRMC (78 MHz),	PD100-NIR	Qubig
broadband	OPO (87.6 MHz)	PDA05CF2	Thorlabs
broadband	MZ	PDA100A-EC	Thorlabs
broadband	PLL	DET01CFC(/M)	Thorlabs

Acknowledgements

This experiment was supported by many people. I could not achieve this experiment without them.

First, I thank my supervisor, Masaki Ando, who is an associate professor of the University of Tokyo. He supported me to focus on the experiment in NAOJ. I thank his advice in the weekly meeting and the rehearsal of the JPS meeting and the thesis defense and so on.

I thank Raffaele Flaminio, a professor of LAPP. He was my former supervisor in NAOJ and he is the principal investigator of our filter cavity experiment. I am grateful that he started this interesting experiment and warmly accepted me at NAOJ. His advice, particularly, at the filter cavity meeting, was really helpful.

I thank Yoichi Aso, an associate professor of NAOJ. He is my supervisor in NAOJ. He helped the development of the digital system and suspensions in TAMA.

I thank Kentaro Somiya, an associate professor of Tokyo Tech. I thank him a lot for his financial support by JST CREST.

I thank Matthew Evans, an associate professor of MIT. I visited MIT for 2 weeks to work on a 16 m filter cavity experiment. He kindly accepted me at MIT although I adjusted my visit schedule several times.

I thank Yuta Michimura, an assistant professor of the University of Tokyo. I thank him for his financial support of my travel. I learned a lot from him since I was an undergraduate student. I am always surprised by his various works on KAGRA, DECIGO, Lorentz invariance test, optical levitation, axion dark matter search, and so on.

I thank all the collaborators. Ryutaro Takahashi, an assistant professor of NAOJ, took care of the suspensions and vacuum system in TAMA. Chien-Ming Wu, a researcher in National Tsing Hua University in Taiwan, is an expert on squeezing ; he visited us twice and made incredible progress. I am impressed that he found our problem about alignment of the homodyne detector and solved it soon, improving the squeezing level and bandwidth within a few days. Pierre Prat, an engineer in APC, developed an automatic analog servo for the squeezer and filter cavity used in our experiment. We would have wasted a lot of time without the servo. Henning Vahlbruch, a researcher in MPG-AEI, developed our homodyne detector and provided us some essential advice about our squeezer. Eleonora Polini, a PhD student in LAPP, designed the injection and reflection telescope of our filter cavity. Ayaka Shoda, who was an appointed assistant professor in NAOJ, helped our digital system and suspensions in TAMA. For the digital system, we got substantial help

from KAGRA staff; Osamu Miyakawa, Takahiro Yamamoto, and Shoichi Oshino. Yuefan Guo, a PhD student in Nikhef, designed the optical configuration for auto alignment. Martin van Beuzekom, an engineer in Nikhef, developed QPDs for the auto alignment. There were also many visitors from all over the world to help our experiment. I thank all of them.

I also thank the Ando lab members for their useful comments in the weekly meeting and so on.

I thank the LIGO lab members in MIT, particularly, Matthew Evans, Lee McCuller, Kentaro Komori, Christopher Whittle, and Dhruva Ganapathy. I sometimes talked with Kentaro Komori about our own experiments and I was able to understand the filter cavity in MIT and LIGO much better thanks to him.

I thank the following officers for their support: Mayuko Niwata in the University of Tokyo, Mizuho Yoshizumi, Mie Ueda, Megumi Ohyama, Mikiko Harada in NAOJ, Fumiko Miyama in Tokyo Tech, Marie Woods in MIT, and Felicia Armijo and Nately Sych in Caltech.

Lastly, I thank Yuhang Zhao, Eleonora Capocasa, and Matteo Leonardi with whom I worked most of the time during my PhD. I would not have been able to complete this experiment without their great work. Yuhang Zhao, a researcher in NAOJ, proceeded the experiment step by step and made steady progress. Eleonora Capocasa, an assistant professor in APC, designed and characterized our filter cavity. She also developed the digital system for our filter cavity. Matteo Leonardi, an assistant professor of NAOJ, is my vice supervisor in NAOJ and I learned a lot of things from him. Every time we had troubles, he always led us in the right direction. I cannot count the number of questions I have asked him thus far, and discussions with him always deepens my understanding much better. I am honored to have a great supervisor like him.

This work was supported by JSPS Grant-in-Aid for Scientific Research (Grants No. 18H01224, No. 18H01235 and No. 18K18763) and JST CREST (Grant No. JPMJCR1873).

Bibliography

[1] B. P. Abbott *et al.* (LIGO Scientific Collaboration and Virgo Collaboration), Observation of Gravitational Waves from a Binary Black Hole Merger, Phys. Rev. Lett. **116**, 061102 (2016).

[2] B. P. Abbott *et al.* (LIGO Scientific Collaboration and Virgo Collaboration), GW170817: Observation of Gravitational Waves from a Binary Neutron Star Inspiral, Phys. Rev. Lett. **119**, 161101 (2017).

[3] B. P. Abbott *et al.* (LIGO Scientific Collaboration and Virgo Collaboration), GWTC-1: A Gravitational-Wave Transient Catalog of Compact Binary Mergers Observed by LIGO and Virgo during the First and Second Observing Runs, Phys. Rev. X **9**, 031040 (2019).

[4] J. Aasi *et al.* (LIGO Scientific Collaboration), Advanced LIGO, Class. Quantum Grav. **32**, 074001 (2015).

[5] F. Acernese *et al.* (The Virgo Collaboration), Advanced Virgo: A second-generation interferometric gravitational wave detector, Class. Quantum Grav. **32**, 024001 (2015).

[6] B. P. Abbott *et al.* (LIGO Scientific Collaboration and Virgo Collaboration), GWTC-2: Compact Binary Coalescences Observed by LIGO and Virgo During the First Half of the Third Observing Run, arXiv:2010.14527.

[7] Y. Aso, Y. Michimura, K. Somiya, M. Ando, O. Miyakawa, T. Sekiguchi, D. Tatsumi, and H. Yamamoto (The KAGRA Collaboration), Interferometer design of the KAGRA gravitational wave detector, Phys. Rev. D **88**, 043007 (2013).

[8] B. P. Abbott *et al.* (LIGO Scientific, Virgo, and KAGRA Collaborations), Prospects for observing and localizing gravitational-wave transients with Advanced LIGO, Advanced Virgo and KAGRA, Living Rev. Relativity **23**, 3 (2020).

[9] C. M. Caves, Quantum-mechanical noise in an interferometer, Phys. Rev. D **23**, 1693 (1981).

[10] M. Tse *et al.*, Quantum-Enhanced Advanced LIGO Detectors in the Era of Gravitational-Wave Astronomy, Phys. Rev. Lett. **123**, 231107 (2019).

[11] F. Acernese *et al.* (Virgo Collaboration), Increasing the Astrophysical Reach of the Advanced Virgo Detector via the Application of Squeezed Vacuum States of Light, Phys. Rev. Lett. **123**, 231108 (2019).

[12] H. Yu *et al.*, Quantum correlations between light and the kilogram-mass mirrors of LIGO, Nature **583**, 43-47 (2020).

[13] F. Acernese *et al.* (Virgo Collaboration), Quantum Backaction on Kg-Scale Mirrors: Observation of Radiation Pressure Noise in the Advanced Virgo Detector, Phys. Rev. Lett. **125**, 131101 (2020).

[14] H. J. Kimble, Y. Levin, A. B. Matsko, K. S. Thorne, and S. P. Vyatchanin, Conversion of conventional gravitational-wave interferometers into quantum nondemolition interferometers by modifying their input and/or output optics, Phys. Rev. D **65**, 022002 (2001).

[15] S. Chelkowski, H. Vahlbruch, B. Hage, A. Franzen, N. Lastzka, K. Danzmann, and R. Schnabel, Experimental characterization of frequency-dependent squeezed light, Phys. Rev. A **71**, 013806 (2005).

[16] E. Oelker, T. Isogai, J. Miller, M. Tse, L. Barsotti, N. Mavalvala, and M. Evans, Audio-Band Frequency-Dependent Squeezing for Gravitational-Wave Detectors, Phys. Rev. Lett. **116**, 041102 (2016).

[17] Y. Zhao, N. Aritomi, E. Capocasa, M. Leonardi, M. Eisenmann, Y. Guo, E. Polini, A. Tomura, K. Arai, Y. Aso, Y.-C. Huang, R.-K. Lee, H. Lück, O. Miyakawa, P. Prat, A. Shoda, M. Tacca, R. Takahashi, H. Vahlbruch, M. Vardaro, C.-M. Wu, M. Barsuglia, and R. Flaminio, Frequency-Dependent Squeezed Vacuum Source for Broadband Quantum Noise Reduction in Advanced Gravitational-Wave Detectors, Phys. Rev. Lett. **124**, 171101 (2020).

[18] N. Aritomi, M. Leonardi, E. Capocasa, Y. Zhao, and R. Flaminio, Control of a filter cavity with coherent control sidebands, Phys. Rev. D **102**, 042003 (2020).

[19] M. Maggiore, Gravitational Waves, Oxford University Press, Oxford, 2008.

[20] C. D. Ott, Probing the core-collapse supernova mechanism with gravitational waves, Classical and Quantum Gravity, 26(20) 204015, (2009).

[21] T. L. Smith, M. Kamionkowski, and A. Cooray, Direct detection of the inflationary gravitational-wave background, Phys. Rev. D **73**, 023504 (2006).

[22] S. Kawamura *et al.*, The Japanese space gravitational wave antenna: DECIGO, Class. Quantum Grav. **23**, S125 (2006).

[23] B. O'Reilly, LIGO-Virgo Cumulative Event Rate Plot O1-O3a (added a separate plot to include O3b public alerts), LIGO-G2001862 (2020).

[24] B. P. Abbott *et al.* (LIGO Scientific Collaboration and Virgo Collaboration), Population Properties of Compact Objects from the Second LIGO-Virgo Gravitational-Wave Transient Catalog, arXiv:2010.14533.

[25] R. Abbott *et al.* (LIGO Scientific Collaboration and Virgo Collaboration), GW190814: Gravitational Waves from the Coalescence of a 23 Solar Mass Black Hole with a 2.6 Solar Mass Compact Object, Astrophys. J. Lett. **896** L44 (2020).

[26] B. P. Abbott *et al.* (LIGO Scientific Collaboration and Virgo Collaboration), GW190521: A Binary Black Hole Merger with a Total Mass of 150 $M_{\odot}$, Phys. Rev. Lett. **125**, 101102 (2020).

[27] S. E. Woosley, Pulsational Pair-instability Supernova, Astrophys. J. **836**, 244 (2017).

[28] B. P. Abbott *et al.* (LIGO Scientific Collaboration and Virgo Collaboration), Tests of General Relativity with Binary Black Holes from the second LIGO-Virgo Gravitational-Wave Transient Catalog, arXiv:2010.14529.

[29] B. P. Abbott *et al.* (LIGO Scientific Collaboration and Virgo Collaboration), GW190425: Observation of a Compact Binary Coalescence with Total Mass $\sim 3.4 M_{\odot}$, Astrophys. J. Lett. 892, L3 (2020).

[30] B. P. Abbott *et al.*, Multi-messenger Observations of a Binary Neutron Star Merger, Astrophys. J. Lett. 848, L12 (2017).

[31] LIGO Scientific Collaboration, Virgo Collaboration, Fermi Gamma-Ray Burst Monitor, and INTEGRAL, Gravitational Waves and Gamma-rays from a Binary Neutron Star Merger: GW170817 and GRB 170817A, The Astrophysical Journal Letters, 848(2) L13, (2017).

[32] The LIGO Scientific Collaboration and The Virgo Collaboration, The 1M2H Collaboration, The Dark Energy Camera GW-EM Collaboration and the DES Collaboration, The DLT40 Collaboration, The Las Cumbres Observatory Collaboration, The VINROUGE Collaboration and The MASTER Collaboration, A gravitational-wave standard siren measurement of the Hubble constant, Nature **551**, 85-88 (2017).

[33] M. Punturo *et al.*, The Einstein Telescope: a third-generation gravitational wave observatory, Class. Quantum Grav. **27**, 194002 (2010).

[34] B. P. Abbott *et al.*, Exploring the sensitivity of next generation gravitational wave detectors, Class. Quantum Grav. **34**, 4, 044001 (2017).

[35] ET Science Team, ET conceptual design study document, http://www.et-gw.eu/index.php/etdsdocument.

[36] LIGO Scientific Collaboration, Instrument Science White Paper 2020, LIGO-T2000407.

[37] T. Fricke, N. Smith-Lefebvre, R. Abbott, R. Adhikari, K. Dooley, M. Evans, P. Fritschel, V. Frolov, K. Kawabe, J. Kissel, B. Slagmolen, and S. Waldman, DC readout experiment in Enhanced LIGO, Class. Quantum Grav. **29**, 6, 065005 (2012).

[38] T. Isogai, J. Miller, P. Kwee, L. Barsotti, and M. Evans, Loss in long-storage-time optical cavities, Opt. Express **21**, 30114-30125 (2013).

[39] R. W. P. Drever, J. L. Hall, F. V. Kowalski, J. Hough, G. M. Ford, A. J. Munley and H. Ward, Laser phase and frequency stabilization using an optical resonator, Appl. Phys. B **31**, 97-105 (1983).

[40] Y. Enomoto, K. Komori, Y. Michimura, K. Somiya, K. Yamamoto, and T. Yamamoto, Latest estimated sensitivity of KAGRA, JGW-T1707038.

[41] C. M. Caves and B. L. Schumaker, New formalism for two-photon quantum optics. I. Quadrature phases and squeezed states, Phys. Rev. A **31**, 3068 (1985).

[42] B. L. Schumaker and C. M. Caves, New formalism for two-photon quantum optics. II. Mathematical foundation and compact notation, Phys. Rev. A **31**, 3093 (1985).

[43] R. W. Boyd, Nonlinear Optics, Third edition, Academic Press, Elsevier, 2007.

[44] D. E. Zelmon, D. L. Small, and D. Jundt, Infrared corrected Sellmeier coefficients for congruently grown lithium niobate and 5 mol.% magnesium oxide-doped lithium niobate, J. Opt. Soc. Am. B 14, 3319-3322 (1997).

[45] S. Dywer, Quantum noise reduction using squeezed states in LIGO, PhD thesis, Massachusetts Institute of Technology, 2013.

[46] E. Oelker, Squeezed States for Advanced Gravitational Wave Detectors, PhD thesis, Massachusetts Institute of Technology, 2016.

[47] G. Mansell, Squeezed light sources for current and future interferometric gravitational-wave detectors, PhD thesis, Australian National University, 2018.

[48] C. W. Gardiner and M. J. Collett, Input and output in damped quantum systems: Quantum stochastic differential equations and the master equation, Phys. Rev. A **31**, 3761 (1985).

[49] S. Chelkowski, H. Vahlbruch, K. Danzmann, and R. Schnabel, Coherent control of broadband vacuum squeezing, Phys. Rev. A **75**, 043814 (2007).

[50] J. Appel, D. Hoffman, E. Figueroa, and A. I. Lvovsky, Electronic noise in optical homodyne tomography , Phys. Rev. A **75**, 035802 (2007).

[51] E. Schreiber, Gravitational-wave detection beyond the quantum shot-noise limit: The integration of squeezed light in GEO 600, PhD thesis, Max Planck Institute for Gravitational Physics (Albert Einstein Institute) and Institute for Gravitational Physics, Leibniz Universität Hannover, 2018.

[52] P. Kwee, J. Miller, T. Isogai, L. Barsotti, and M. Evans, Decoherence and degradation of squeezed states in quantum filter cavities, Phys. Rev. D **90**, 062006 (2014).

[53] J. Abadie *et al.* (LIGO Scientific Collaboration), A gravitational wave observatory operating beyond the quantum shot-noise limit, Nat. Phys. **7**, 962 (2011).

[54] V. Akulov, S. Babin, S. Kablukov, and K. Raspopin, Intracavity frequency doubling of Yb-doped fiber laser with 540-550 nm tuning, Laser Phys. **21**, 935-939 (2011).

[55] V. Akulov, S. Kablukov, and S. Babin, Frequency doubling of a tunable ytterbium-doped fibre laser in KTP crystals phase-matched in the XY and YZ planes, Quantum Electron. **42**, 120 (2012).

[56] M. Leonardi, Development of a squeezed light source prototype for Advanced Virgo, PhD thesis, University of Trento, 2016.

[57] K. Nagano, A. Perreca, K. Arai, and R. X Adhikari, External quantum efficiency enhancement by photon recycling with backscatter evasion, Appl. Opt. **57**, 3372-3376 (2018).

[58] H. Vahlbruch, M. Mehmet, K. Danzmann, and R. Schnabel, Detection of 15 dB Squeezed States of Light and Their Application for the Absolute Calibration of Photoelectric Quantum Efficiency, Phys. Rev. Lett. **117**, 110801 (2016).

[59] R. Takahashi and the TAMA Collaboration, Status of TAMA300, Class. Quantum Grav. **21**, S403 (2004).

[60] R. Takahashi and K. Arai, and the TAMA Collaboration, Improvement of the vibration isolation system for TAMA300, Classical Quantum Gravity **19**, 1599 (2002).

[61] R. Takahashi, F. Kuwahara, E. Majorana, M. A. Barton, T. Uchiyama, K. Kuroda, A. Araya, K. Arai, A. Takamori, M. Ando, K. Tsubono, M. Fukushima, and Y. Saito, Vacuum-compatible vibration isolation stack for an interferometric gravitational wave detector TAMA300, Rev. Sci. Instrum. **73**, 2428 (2002).

[62] E. Capocasa, M. Barsuglia, J. Degallaix, L. Pinard, N. Straniero, R. Schnabel, K. Somiya, Y. Aso, D. Tatsumi, and R. Flaminio, Estimation of losses in a 300 m filter cavity and quantum noise reduction in the KAGRA gravitational-wave detector, Phys. Rev. D **93**, 082004 (2016).

[63] E. Capocasa, Y. Guo, M. Eisenmann, Y. Zhao, A. Tomura, K. Arai, Y. Aso, M Marchiò, L. Pinard, P. Prat, K. Somiya, R. Schnabel, M. Tacca, R. Takahashi, D. Tatsumi, M. Leonardi, M. Barsuglia, and R. Flaminio, Measurement of optical losses in a high-finesse 300 m filter cavity for broadband quantum noise reduction in gravitational-wave detectors, Phys. Rev. D **98**, 022010 (2018).

[64] E. Capocasa, Optical and noise studies for Advanced Virgo and filter cavities for quantum noise reduction in gravitational-wave interferometric detectors, Ph.D. thesis, Université Paris Diderot, 2017.

[65] L. McCuller and L. Barsotti, Design Requirement Document of the A+ filter cavity and relay optics for frequency dependent squeezing, LIGO-T1800447 (2020).

[66] The Virgo Collaboration, Advanced Virgo Plus Phase I - Design Report, https://tds.virgo-gw.eu/?content=3&r=15777.

[67] E. Genin, M. Mantovani, G. Pillant, C. De Rossi, L. Pinard, C. Michel, M. Gosselin, and J. Casanueva, Vacuum-compatible low-loss Faraday isolator for efficient squeezed-light injection in laser-interferometer-based gravitational-wave detectors, Appl. Opt. **57**, 9705-9713 (2018).

[68] L. McCuller, C. Whittle, D. Ganapathy, K. Komori, M. Tse, A. Fernandez-Galiana, L. Barsotti, P. Fritschel, M. MacInnis, F. Matichard, K. Mason, N. Mavalvala, R. Mittleman, Haocun Yu, M. E. Zucker, and M. Evans, Frequency-Dependent Squeezing for Advanced LIGO, Phys. Rev. Lett. **124**, 171102 (2020).

[69] H. A. Macleod, Thin-Film Optical Filters, 5th ed. (CRC Press, Boca Raton, Florida, 2018).

[70] E. Morrison, B. J. Meers, D. I. Robertson, and H. Ward, Automatic alignment of optical interferometers, Appl. Opt. **33**, 5041-5049 (1994).

[71] K. Kokeyama, J. G. Park, K. Cho, S. Kirii, T. Akutsu, M. Nakano, S. Kambara, K. Hasegawa, N. Ohishi, K. Doi, and S. Kawamura, Demonstration for a two-axis interferometric tilt sensor in KAGRA, Phys. Lett. A **382**, 1950 (2018).

[72] K. L. Dooley, E. Schreiber, H. Vahlbruch, C. Affeldt, J. R. Leong, H. Wittel, and H. Grote, Phase control of squeezed vacuum states of light in gravitational wave detectors, Opt. Express **23**, 8235 (2015).

[73] E. Oelker, L. Barsotti, S. Dwyer, D. Sigg, and N. Mavalvala, Squeezed light for advanced gravitational wave detectors and beyond, Opt. Express **22**, 21106 (2014).

[74] K. Somiya, E. Hirose, and Y. Michimura, Influence of nonuniformity in sapphire substrates for a gravitational wave telescope, Phys. Rev. D **100**, 082005 (2019).

[75] D. V. Martynov *et al.*, Sensitivity of the Advanced LIGO detectors at the beginning of gravitational wave astronomy, Phys. Rev. D **93**, 112004 (2016).

[76] H. Kogelnik and T. Li, Laser Beams and Resonators, Appl. Opt. **5**, 1550-1567 (1966).

[77] G. Heinzel, TAMA beam centering system, TAMA300 Library, QPD Steering (1999).